EVOLUTION OF SINGLE PARTICLE STRENGTHS IN TIN ISOTOPES AND IMPACTS ON NEUTRON CAPTURE

BY BRETT MONTGOMERY MANNING

A dissertation submitted to the

Graduate School—New Brunswick

Rutgers, The State University of New Jersey

in partial fulfillment of the requirements

for the degree of

Doctor of Philosophy

Graduate Program in Physics and Astronomy

Written under the direction of

Dr. Jolie A. Cizewski

and approved by

_____

_____

_____

_____

_____

New Brunswick, New Jersey

October, 2014

ABSTRACT OF THE DISSERTATION

Evolution of Single Particle Strengths in Tin Isotopes and Impacts on Neutron Capture

by Brett Montgomery Manning

Dissertation Director: Dr. Jolie A. Cizewski

Atomic nuclei with a few nucleons beyond shell closures are important in understanding the evolution of single-particle structure, which is critical to the benchmarking of nuclear models. With radioactive ion beams, studies near the double closed shell nucleus ^{132}Sn have been made possible. While the single-neutron states in ^{133}Sn with $N = 83$ and ^{131}Sn with $N = 81$ have recently been verified to be highly pure, it is important to study further from the $N = 82$ neutron shell closure.

Level energies and spectroscopic information for neutron-rich nuclei also provide important input for the rapid neutron capture r-process nucleosynthesis calculations. Specifically, it is important to know the location and strength of single-neutron states with orbital angular momentum $\ell = 1$ when calculating neutron-capture rates. Surman and collaborators have performed sensitivity studies to show that varying neutron-capture rates can significantly alter final r-process abundances. However, there are many nuclei important to the r-process that cannot be studied. Extending studies to more neutron-rich nuclei will help constrain the nuclear shell model in extrapolating to nuclei even further from stability.

The (d, p) neutron transfer reaction has been measured in inverse kinematics with radioactive ion beams of ^{126}Sn and ^{128}Sn and a stable beam of ^{124}Sn, all in inverse-kinematics at the Holifield Radioactive Ion Beam Facility at Oak Ridge National Laboratory, utilizing the SuperORRUBA (Oak Ridge Rutgers University Barrel Array) of silicon detectors. The present work is combined with previous studies to complete the set of (d, p) studies on even mass tin isotopes from doubly-magic ^{132}Sn to stable ^{124}Sn and the systematics of $\ell = 1$ and $\ell = 3$ strengths. The results of the (d, p) study are used to map the fragmentation of single-neutron strengths in $N \leq 82$ tin isotopes and to calculate the direct-semidirect neutron capture on these even mass tin isotopes that are important for the astrophysical r-process.

Acknowledgements

Looking back on my five years in graduate school it is amazing to recall the number of people who helped me get to where I am today. From my time in New Jersey and then Tennessee, to the countless other labs I was fortunate to work in, I have always received tremendous support from those around me.

I would first like to thank the individuals responsible for bringing me into nuclear physics; Jolie Cizewski, my graduate advisor, and Fredric Sarazin, my undergraduate advisor. I was new to nuclear physics when I first started working for Jolie, but she was always patient. Her tireless work ethic, generosity, and knowledge of the best restaurants in every city have all served to inspire me during the challenging moments. Jolie was a fantastic boss, and I will truly miss being a part of her team. Similarly, Fred has been instrumental in my graduate career. He showed me that research can be fun during a time when I was skeptical, despite taking me to sing karaoke in Oak Ridge.

To my friends in New Brunswick, thanks for all of the great times. Eliav, for everything, the least of which was the constant supply of food, drinks, and tickets. Matt and Alex for being amazing friends that did not forget me when I moved away! Seba, Mike Berry, Brandon, Michael Manhart, Enrique, and all the others for the great memories of Rutgers. I would also like to thank Noemie and

Gerfried for always being supportive of me and including me in their work.

During my time in Tennessee I have benefited from many great friendships and the lessons learned along the way. Remi, for all he taught me and his wonderful laugh (sorry I fell asleep during church). Diego taught me the value in working smart. Brian showed me that nuclear physicists can have fun, keeping me in the field. Dan for being a great friend and mentor, and being the master of cornhole. Andy, for telling me not to come in at 8am my first day. Pittman for the trips to Bojangles when nobody else would go. Bill, for showing me the true value of a PhD in physics. Callum and Sarah for all the great trips around the US, and not judging us too harshly. Eric and Sara for always introducing me to the newest spots downtown. Andrew for so many great nights and always keeping the refrigerator stocked at conferences. Travis for showing me how out of shape I was on the Appalachian Trail. Paul for always alerting me of the latest Groupon at Mother Earth Meats. Shuya for the constant jokes and be willing to sing Rocky Top anywhere we go. Steve Taylor for all of the time spent talking about fishing. David and Sean for the great summers. Michael for always taking an interest in my work and looking out for me. Shisheng and Caroline for their encouragement. Goran, for all of the great discussions and allowing me to aid in your work. Filomena for teaching me FRESCO, and Luke for clarifying reaction theory for me. Felix, Dan Shapira, Alfredo, and David Radford for taking time to help a student you had just met. Kate, Robert, Kay, Gio, Stan, and Miguel for welcoming me into the nuclear group at UT. Tim for all the great games, even

though the ISU game was the worst night of my life. Margi and Scott for the true Tennessee gameday experience on the river.

Ray for not only handing over your approved experiments, but also supporting me the entire way (and actually reading my dissertation). Meredith and Leslie for helping prepare me the night before my oral qualifier and remaining great friends, even when they drop big announcements while getting in the car. Steve and Kelly for more great times than I can recall, but most of all for making sure I was not killed in the exploding fire. Mitch and Aimee, for all you taught me and all of the great food we shared. Tony and his family, for more than I could ever express in words, thank you for making me part of your family.

Lastly to all of my family and family friends. My grandparents for being tremendous role models of how to work hard no matter the situation. My amazing aunts and uncles (and adopted aunts and uncles) who have always treated like I was their own. My parents for their unconditional support; transcribing my math homework when I was in a cast two years in a row, wanting to buy me the biggest Cadillac at NE, and always making sure I had access to BBQ even when times were hard. My sisters, for both blazing the trail before me and pushing me from behind, there is no doubt I would not be here if not for all of the pressure your success placed on me. And finally to Sarah, for her unconditional love and friendship. Letting me walk home in the dark after a tough loss, encouraging me when I was going crazy, and always being willing to road trip anywhere.

Thank you all so much.

Table of Contents

List of Tables

List of Figures

Chapter 1

Introduction

The study of nuclear structure is a rich field combining the efforts of theory and experiment to understand the shapes, sizes, and internal states of the atomic nucleus. Of further interest is the study of transitions between nuclear states as well as the decay of the nucleus. Experimental data have established well-known trends in nuclear structure that theory aims to predict. A whole host of theoretical models exist, from macroscopic models such as the liquid drop model [Won04] to microscopic *ab initio* approaches such as the no core shell model [Nav00, Bar13a]. Naturally, each model has limitations and one must decide which model to employ based on the isotope itself as well as the structure of interest.

Traditionally, only stable nuclei or those with long half-lives could be studied, but the advent of radioactive ion beams (RIBs) has pushed studies towards the limits of existence on the neutron-rich side of the nuclear chart. RIBs have presented new challenges for experimentalists studying these exotic nuclei. Additionally, the experimental results are challenging the validity of nuclear structure theory for nuclei away from stability.

At the intersection of nuclear structure and astrophysics is the field of nuclear astrophysics, which helps to explain how the elements are produced in stars. Studying the structure of proton-rich and neutron-rich nuclei is providing a dramatic impact on nuclear astrophysics as many of these isotopes are on the rapid proton capture process (rp-process) path and the rapid neutron capture process (r-process) path, respectively. These processes are largely responsible for the production of elements heavier than iron [Cla68].

1.1 The Nuclear Shell Model

Early studies of nuclear structure indicated that there are "magic numbers" of both protons and neutrons for which certain features exhibit abrupt deviations from otherwise smooth patterns. These numbers are 2,8,20,28,50,82 for protons and neutrons with 126 also being magic for neutrons [May49, Hax49]. A well-known indicator of these magic numbers comes from the two-proton and two-neutron separation energies [Nil95]. Just beyond the "magic numbers", the two-proton and two-neutron separation energies fall off dramatically. A similar effect is seen in the ionization energy for atomic electrons and their corresponding "magic numbers" in the noble gases. Another example exists for isotopes with an even number of protons and neutrons. For these nuclei, the first excited 2^+ state will be dramatically higher in excitation energy as compared to the local trend

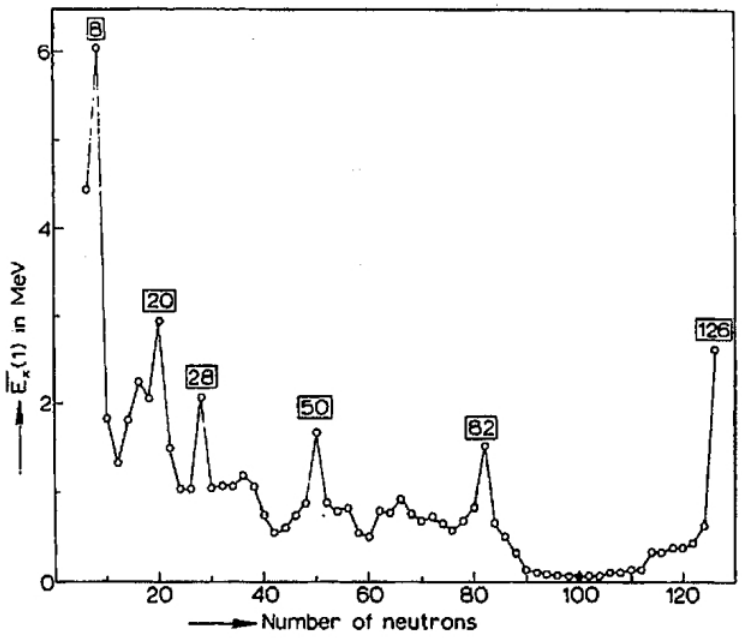

Figure 1.1: Magic numbers manifest in plot of average excitation energy of the first excited 2^+ state in doubly-even nuclei as a function of neutron number. Figure taken from Reference [Bru77].

when the nucleus has a magic number of neutrons or protons as shown in Figure 1.1. In the tin isotopes with 50 protons and away from $N = 50$ and $N = 82$, the first excited state has a spin and parity of 2^+ and at an excitation energy of approximately 1200 keV as compared to about 500 keV for the neighboring nuclei [Cas00]. However, at $N = 82$ the first 2^+ state in ^{132}Sn is above 4000 keV.

Unlike the atomic shell model described by the electromagnetic force, the strong nuclear force is not well understood. Still, several important characteristics of the strong force have been deduced from fundamental principles and experimental studies. In particular, the strong force is attractive over short distances ($\sim$2.5 fm), but there is a strongly repulsive "hard core" [Nil95]. The short

range of the strong force is understood as a consequence of the uncertainty principle [Rin80]. Consequently, only a few nucleons can interact with each other at a time, and thus the nuclear force will saturate. Another key point is that nucleons must obey the Pauli principle. If two nucleons collide one must be scattered to an available quantum state above the Fermi energy [Nil95]. Such a collision would require a large energy transfer and rarely happens, and thus the nucleons can be considered non-interacting particles.

Nucleons moving in an average central potential created by the constituent nucleons is a many-body system that can be modeled by shells. A three-dimensional harmonic oscillator is a good starting point for the interaction potential as analytic solutions exist for the Schrödinger equation in this case. The energy orbitals are degenerate for $2n + \ell$ and do not reproduce all of the observed "magic numbers" as shown in Figure 1.2.

Employing a more realistic Woods-Saxon shape potential is a first step to improving the nuclear shell model. Figure 1.2 shows that the new potential lifts some of the degeneracy. However, the predicted "magic numbers" still do not correspond with observation. The genius of the nuclear shell model was adding a spin-orbit term to the average potential. Mayer [May49] and Haxel, Jensen, and Suess [Hax49] independently proposed a spin-orbit term that is attractive when the orbital angular momentum and spin are aligned and repulsive when they are

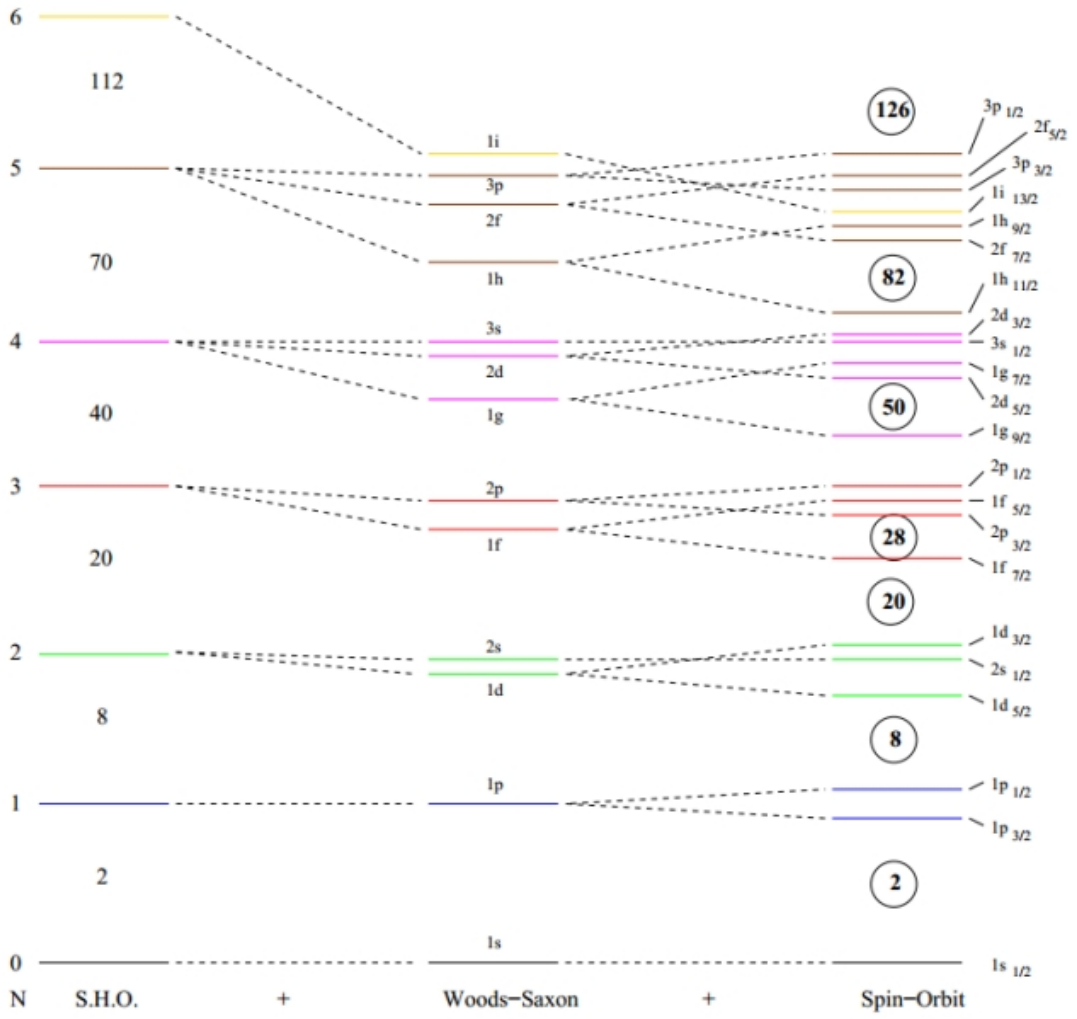

Figure 1.2: Energy levels and shell structure of nuclei shown for different potentials. The left most plot shows the energy levels for a simple harmonic oscillator. All energy levels are evenly spaced and are degenerate for $2n + \ell$. The middle plot shows the energy levels for a Woods-Saxon type potential. Some degeneracy is lifted, but not all shell closures correspond to the "magic numbers". The right most plot shows the energy levels using a Woods-Saxon type potential with the addition of a spin-orbit component. Adding the spin-orbit term reproduces the observed "magic numbers". Figure taken from Brown et al. [Bro10].

anti-aligned. The addition of this term allowed the nuclear shell model to accurately reproduce the magic numbers as shown in Figure 1.2.

The nuclear shell model is adept at describing stable nuclei at or near shell closures. Specifically, it is possible to predict the ground state angular momentum, or spin and parity for odd mass isotopes. The orbital angular momentum for such nuclei is given by the orbital angular momentum of the last unpaired nucleon. For nuclei with an even number of both protons and neutrons, the ground state spin will be zero with even parity because all nucleons are paired resulting in zero net orbital angular momentum.

1.2 The *r*-process

Several processes driven by nuclear fusion are known to produce nuclei up to iron [Cla68]. Beyond iron it is no longer energetically favorable to produce heavier nuclei through charged-particle fusion. The slow neutron capture process (*s*-process) can occur in environments with intermediate temperatures and relatively low neutron densities ($\sim 10^6$ n/cm^3) such as asymptotic giant branch stars [Cla68]. The *s*-process proceeds much slower than beta decay, and thus this process produces nuclei at or near stability that are heavier than iron. Burbidge, Burbidge, Fowler, and Hoyle noted that a rapid neutron capture process

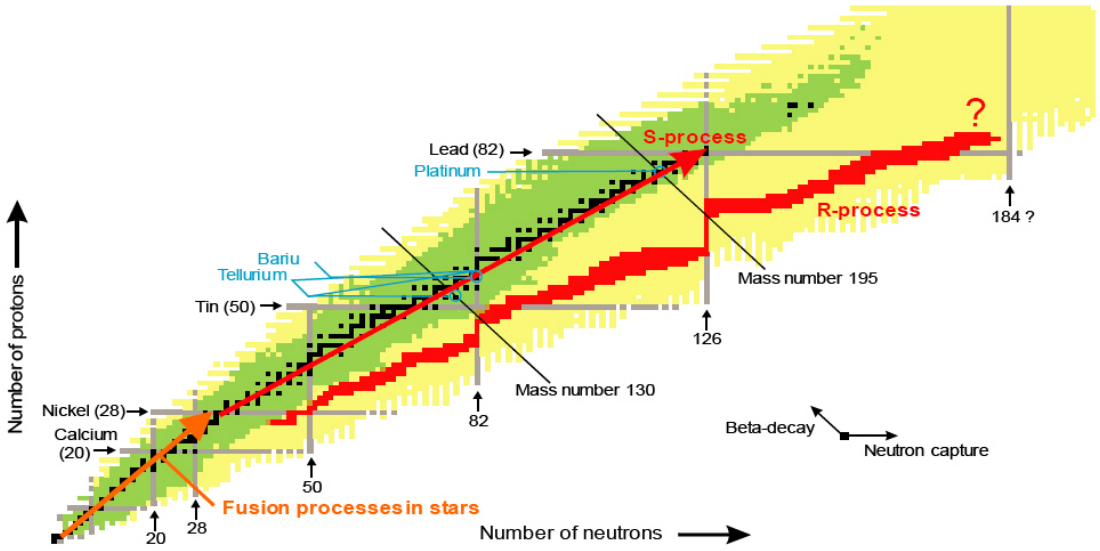

Figure 1.3: Chart of the nuclides. Black squares represent stable nuclei. Green squares represent nuclei that had been observed at the time the figure was made. Yellow squares represent the believed limits of existence. "Magic numbers" are indicated on the plot by gray lines. A possible r-process path is indicated by the red squares. Figure taken from Reference [Hab11].

(r-process) must also exist to explain observed isotopic abundance peaks at germanium, xenon, and platinum [Bur57]. It is believed that the r-process accounts for more than half of the nuclei heavier than iron. Still, the exact site of the r-process is not known. Possible candidates include core-collapse supernovae with both high neutron density ($> 10^{20}$ n/cm^3) and temperature or neutron star mergers with exceedingly high neutron densities [Hil78, Mat90].

While the r-process path is not precisely known, simulations indicate that it should proceed through neutron-rich nuclei as shown in Figure 1.3. Successive neutron captures occur rapidly on heavy seed nuclei until a balance is established between further neutron capture and photodisintegration. Under r-process conditions, neutron capture and photodisintegration rates are much faster than beta

decay rates, therefore, abundances along an isotopic chain are determined by this equilibrium [Qia03]. For an isotope with atomic number Z and mass number A, based on the conditions for statistical equilibrium and a nuclear Saha-type equation for the photodisintegration rate the abundance ratio for neighboring nuclei is given by

$$\begin{aligned}\frac{Y(Z,A+1)}{Y(Z,A)} &= \frac{n_n \langle v\sigma_{n,\gamma}(Z,A)\rangle}{\lambda_{\gamma,n}(Z,A+1)} \\ &= n_n \left(\frac{2\pi\hbar^2}{mkT}\right)^{3/2} \left(\frac{A+1}{A}\right)^{3/2} \frac{G(Z,A+1)}{2G(Z,A)} \exp\left[\frac{S_n(Z,A+1)}{kT}\right], \quad (1.1)\end{aligned}$$

where $Y(Z,A)$ is the abundance of the isotope, $\langle v\sigma_{n,\gamma}(Z,A)\rangle$ is the thermally-averaged neutron capture rate, $\lambda_{\gamma,n}(Z,A+1)$ is the photodisintegration rate, n_n is the neutron density, k is Boltzmann′s constant, T is the temperature, $G(Z,A)$ is the nuclear partition function, m is the neutron mass, and $S_n(Z,A)$ is the neutron separation energy [Cla68].

Adding neutrons to a nucleus in general decreases the neutron separation energy, thus increasing the photodisintegration rate which prevents the r-process path from extending to more neutron-rich isotopes. The abundance of a couple of isotopes will build up for a given isotopic chain until the nuclei can beta decay to a new isotopic chain. For the new isotopic chain, an equilibrium will again be established as several isotopic abundances grow. These isotopes are known

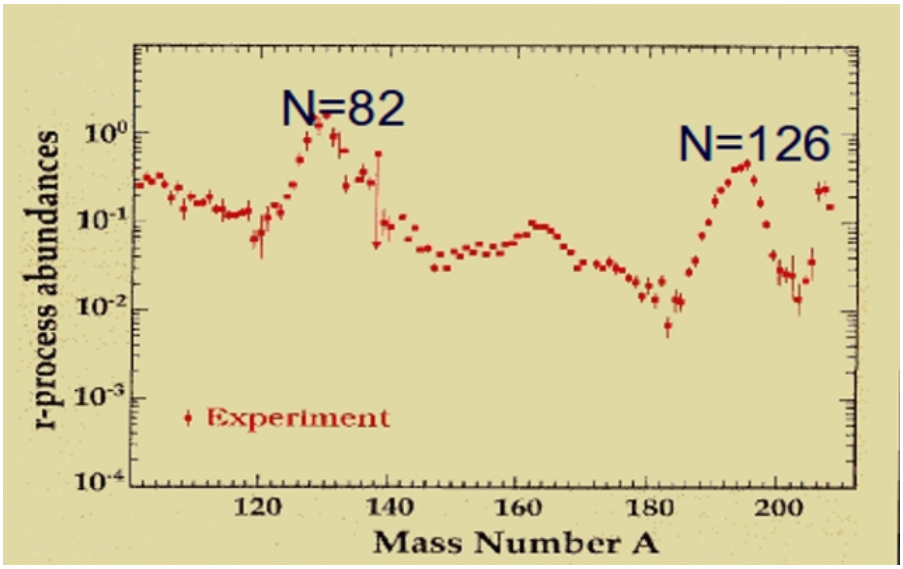

Figure 1.4: Observed r-process abundances show peaks near neutron shell closures at $N = 82$ and $N = 126$. Figure adopted from Reference [Ria00].

as waiting points, where a heavy nucleus must wait for a beta decay to a new isotopic chain before further neutron captures are possible. Immediately beyond closed neutron shells, the neutron separation energy is drastically diminished. Consequently, there will be waiting point nuclei near neutron shell closures. Interestingly, observed r-process abundances indicate peaks corresponding to neutron shell closures as shown in Figure 1.4.

The path of the r-process depends predominantly on the nuclear masses which determine the neutron separation energies. Additionally, beta decay half-lives play an important role in this process. For many nuclei near stability and in the mid-shell region, the neutron capture is dominated by compound nuclear neutron capture that proceeds through closely spaced states above the neutron threshold energy. A statistical model such as the Hauser-Feshbach model can be used to calculate neutron capture cross sections averaged over closely-spaced

resonances [Hau52]. A sufficient level density of about 10 states per MeV is required for this approximation to hold [Rau97]. For light nuclei and isotopes near closed neutron shells, the level density becomes low and it is expected that direct neutron capture will dominate over resonant capture [Moh12]. In direct capture, the neutron populates a discrete bound state with a photon emitted to conserve energy. In semidirect capture the photon strength is enhanced by the tail of the giant dipole resonance (GDR) and the system decays by electromagnetic transitions through the discrete bound states. The direct-semidirect capture process is sensitive to the excitation energies, spins, parities, electromagnetic transition probabilities, and spectroscopic factors of the low-lying states in the final nucleus [Arb05]. Recent work by Surman and collaborators have shown that neutron capture at late times in the r-process can significantly impact final isotopic abundances [Sur01].

1.3 Previous Studies

Studies near ^{132}Sn have been of considerable interest as this nucleus represents a doubly-magic nucleus away from stability. With $Z = 50$ protons and $N = 82$ neutrons, one would naively expect nuclei in this region to exhibit classic features predicted by the shell model. However, the nuclear shell model was developed for stable nuclei and thus is not guaranteed to well describe nuclei near ^{132}Sn, eight units from stability.

Indeed, there has been great interest in studying nuclei near the double-shell closure of $Z = 50$ and $N = 82$ in the era of radioactive ion beams (RIBs) [Jon04, Jon10, Jon11, Koz12, All14]. In particular, Jones et al. studied the (d, p) reaction in inverse kinematics with a RIB of ^{132}Sn [Jon10, Jon11]. The reaction populated f and p-states in ^{133}Sn above the $N = 82$ shell gap. The excitation energies, spins, and parities were determined for the $2f_{7/2}$, $3p_{3/2}$, $3p_{1/2}$, and $2f_{5/2}$ expected above the $N = 82$ shell closure. Using modern reaction theory, spectroscopic factors were extracted for each state. The extracted values indicated that these states were pure single particle states in ^{133}Sn despite being eight units away from stability. More recently, Allmond et al. populated these same states in ^{133}Sn through the ^{132}Sn(^{9}Be,^{8}Be γ) reaction in inverse kinematics [All14]. This study confirmed the work of Jones et al., further supporting the pure single-neutron nature of the observed states.

Kozub et al. studied the (d, p) reaction in inverse kinematics with a RIB of ^{130}Sn ($N = 80$) to study states in ^{131}Sn [Koz12]. Excitation energies, spins, and parities were assigned to the same four states above the $N = 82$ shell gap observed in the ^{132}Sn(d, p) study. The spectroscopic factors extracted for the states in ^{131}Sn indicated that these states were largely single-particle in nature despite the main ground state configuration of ^{130}Sn having two neutron holes below the $N = 82$ shell closure.

Since ^{124}Sn is the heaviest stable tin isotope, there have been several experiments that studied states in ^{125}Sn [Str77, Jon04, Tom11]. Tomandl et al. studied states in ^{125}Sn through the (n,γ) and (d,p) reactions in normal kinematics. The normal kinematics (d,p) study yielded energy resolution of less than 10 keV as compared to 200 keV for inverse kinematic studies on neutron-rich tin isotopes [Jon04, Tom11]. The high energy resolution in the normal kinematics study allowed the researchers to observe the high degree of fragmentation of the single-neutron strength present in ^{125}Sn.

1.4 Goals of the Study

The goal of the present work is to provide a systematic study of both the nuclear structure and the resulting neutron capture cross sections relevant to nuclear astrophysics for the neutron-rich tin isotopes from stable ^{124}Sn out to doubly magic ^{132}Sn. The (d,p) reaction was studied in inverse kinematics with a stable beam of ^{124}Sn and RIBs of ^{126}Sn and ^{128}Sn to study the single-neutron states in ^{125}Sn, ^{127}Sn, and ^{129}Sn where the latter two are being studied for the first time. Measuring reaction protons as a function of angle will provide a $Q-$value spectrum for each reaction. Using previously known masses, the $Q-$value of each state can be converted into an excitation energy in the final nucleus. The population of each state can be divided into angular bins to produce a differential cross section.

Comparing the shape of the experimental differential cross section to that of nuclear reaction theory calculations will allow for a determination of, or constraint on, the transferred orbital angular momentum of the given state. Normalizing the theoretical differential cross section to the experimental differential cross section provides an experimental spectroscopic factor. The previous differential cross sections for ^{130}Sn(d,p), and ^{132}Sn(d,p) will be re-analyzed using the same reaction theory as used for the present study. The excitation energies, spins, parities, and spectroscopic factors for each state will be used to calculate the direct-semidirect neutron capture on ^{124}Sn, ^{126}Sn, ^{128}Sn, ^{130}Sn, and ^{132}Sn.

1.5 Structure of the Dissertation

The structure of the dissertation is presented below.

Chapter 2 provides an introduction to the reaction theory used for calculating differential cross sections for the (d,p) reaction and cross sections for direct-semidirect neutron capture. This chapter also describes how experimental spectroscopic factors are extracted using reaction theory.

Chapter 3 summarizes all of the relevant technical aspects of the experiment ranging from beam production and target fabrication to detectors and electronics. This chapter will be of interest to an experimentalist studying transfer reactions.

Chapter 4 details the data analysis used to extract quantities such as differential cross sections from the experiments. This chapter includes an explanation

of the calibrations for energy and solid angle and angle determinations.

Chapter 5 details how the data are used to extract spectroscopic factors and asymptotic normalization coefficients and calculate neutron capture cross sections.

Chapter 6 summarizes the work presented in this dissertation and presents a look at the future of transfer reactions on RIBs using charged particle-gamma coincidences.

Chapter 2

Reaction Theory

Transfer reactions provide rich spectroscopic data, but reaction theory is needed to reliably interpret these results. This chapter will detail the critical theories necessary to extract excitation energies, spin and parity of states, spectroscopic factors, and neutron capture cross sections. Special attention will be given to explaining how computer codes use these theories to calculate meaningful quantities and how these calculations rely on observables from experiments.

2.1 Scattering Theory

2.1.1 Basics

When two nuclei interact a myriad of possible outcomes exist. In this section we will limit the discussion to include only those interactions for which there are two particles in the final state. In general, the reaction can be written as

$$A + a \rightarrow B + b + Q \text{ or } A(a,b)B, \tag{2.1}$$

where A is the target, a is the projectile, B is the recoil, b is the ejectile, and Q is the energy released during the reaction. Q is often described as the mass difference between the initial particles and the final particles. Each combination of particles is called a partition [Sat70]. A partition may be further distinguished by the quantum state of each particle. A channel is defined as a partition with the particles in given quantum states [Sat70]. It is useful to refer to the partition $A + a$ as the entrance channel when both particles are in their ground state. The partition $B + b$ may have many different configurations which are known as the exit channels [Sat70]. This chapter will illuminate two of the possible exit channels: elastic scattering and direct reactions. In the case of elastic scattering the internal states are unchanged, so $B = A$ and $b = a$, and hence $Q = 0$. The specific direct reaction of interest is the (d, p) reaction, hence, $A + d \rightarrow B^{\star} + p$. $B^{\star}$ indicates that the recoiling nucleus may be in an excited state.

The entrance and exit channels can be described as the scattering of waves off of a potential so that a transition amplitude and cross section can be calculated. First consider a plane wave scattering off a short range potential, $V(\mathbf{r})$. This simple case will lay the foundation for more complicated discussion to follow. Since the incoming plane wave, ψ_i, must satisfy the Schrödinger equation, it can be shown that

$$\psi_i \sim \mathrm{e}^{ikr}, \tag{2.2}$$

where k is the wave number [Sat70]. The outgoing wave, ψ_f, should be a spherical wave originating from the scatterer and should demonstrate the asymptotic behavior

$$\psi_f \rightarrow \mathrm{e}^{ikr} + f(\Omega)\frac{\mathrm{e}^{ikr}}{r}, \tag{2.3}$$

for $r \rightarrow \infty$ where $f(\Omega) \equiv f(\theta, \phi)$ is the scattering amplitude [Sat70]. Once the wavefunctions are known, it can be shown that the number of scattered particles in a channel α, N_α, is proportional to the square of the scattering amplitude [Ber04]. Ultimately, the differential cross section can be calculated for a given channel, α, by

$$\frac{d\sigma_\alpha(\Omega)}{d\Omega} = \frac{N_\alpha}{\Delta\Omega \cdot n \cdot J} \tag{2.4}$$

where $\Delta\Omega$ is the solid angle the particles are scattered into, n is the number of target particles per unit area in the region of the beam interaction, and J is the incident flux of beam particles [Sat70]. The elastic differential cross section [Ber04] is

$$\frac{d\sigma_{\mathrm{el}}(\Omega)}{d\Omega} = |f(\Omega)|^2. \tag{2.5}$$

The total cross section is found by integrating over all angles, thus the total elastic cross section is

$$\sigma_{\mathrm{el}} = \int d\Omega \left[\frac{d\sigma_{\mathrm{el}}(\Omega)}{d\Omega}\right] = 2\pi \int_{-1}^{+1} |f(\Omega)|^2 \, d(\cos\theta). \tag{2.6}$$

Even for the simple case of a spinless particle scattering on a spherical, structureless target the importance of the scattering amplitude is evident.

However, it is well-known that for nuclear scattering the potential exhibits both a short-range attractive nuclear component and a long-range repulsive Coulomb component. Now the potential can be written as $V(r) = V_{\mathrm{C}}(r) + V_{\mathrm{N}}(r)$, where $V_{\mathrm{C}}(r)$ is the Coulomb potential and $V_{\mathrm{N}}(r)$ is a short-range nuclear potential that vanishes at large distances. The new scattering amplitude is given by the sum of the scattering amplitudes for each component of the potential, $f(\theta) = f_{\mathrm{C}}(\theta) + f_{\mathrm{N}}(\theta)$. Thus, the Coulomb cross section [Sat70] is given by

$$\frac{d\sigma_{\mathrm{C}}(\Omega)}{d\Omega} = |f_{\mathrm{C}}(\theta) + f_{\mathrm{N}}(\theta)|^2 . \tag{2.7}$$

Customarily, the short-range potential is the area of interest, so the cross sections are typically normalized with respect to the Rutherford cross section to extract the nuclear cross section.

2.1.2 Formal Scattering Theory

The previous method for calculating cross sections provides a simple approach, but solving for the scattering amplitude can still be a very complicated task. Again let us consider the case of $A(a,b)B$, but this time the wavefunctions describing the internal states will remain general. The wavefunction for each channel, $\psi_x(\mathbf{r_x})$, is given by the product of the wavefunctions for each particle in the partition, ψ_x, where the internal coordinates are given by $\mathbf{r_x}$ [Sat83].

$$\psi_i(\mathbf{r_i}) \equiv \psi_{\mathbf{A}}(\mathbf{r_A})\psi_{\mathbf{a}}(\mathbf{r_a}) \tag{2.8}$$

$$\psi_i(\mathbf{r_f}) \equiv \psi_{\mathbf{B}}(\mathbf{r_B})\psi_{\mathbf{b}}(\mathbf{r_b}) \tag{2.9}$$

The wavefunctions for each channel are the eigenfunction solutions to the Schrödinger equation for the internal Hamiltonians, H_x, with internal eigenenergies ϵ_x [Sat83].

$$H_i\psi_i \equiv (H_a + H_A)\,\psi_i = \epsilon_i\psi_i \tag{2.10}$$

$$H_a\psi_a = \epsilon_a\psi_a, \quad H_A\psi_A = \epsilon_A\psi_A \tag{2.11}$$

$$H_f\psi_f \equiv (H_b + H_B)\,\psi_f = \epsilon_f\psi_f \tag{2.12}$$

$$H_b\psi_b = \epsilon_b\psi_b, \quad H_B\psi_B = \epsilon_B\psi_B \tag{2.13}$$

The total Hamiltonian is given by the sum of the internal Hamiltonians, the

kinetic energy of the relative motion, and the interaction potential. For example, $H = H_a + H_A - \hbar^2/2\mu_i \ \nabla_i^2 + V_i$. The total wavefunction, Ψ, can be written as the expansion

$$\Psi = \sum_f \chi_f(\mathbf{r_f})\psi_\mathbf{i}(\mathbf{r'_f}) \tag{2.14}$$

where the χ_f are projections of Ψ onto the exit channel, f, and $\mathbf{r_f}$ are the internal coordinates of the exit channel [Sat83]. Using properties of the Green functions [Ber04] the scattering amplitude can now be written as

$$f(\theta) = -2\pi^2 \left(\frac{2\mu}{\hbar^2}\right) \left\langle \phi_{k'} \left| V \right| \psi_k^{(+)} \right\rangle \tag{2.15}$$

where $\phi_{k'}$ is the incoming wave with wave number k' and $\psi_k^{(+)}$ is the outgoing spherical wave with wave number k [Sat83]. In this notation, the $(+)$ indicates the outgoing nature of the wave. This expression for the scattering amplitude indicates that it is proportional to the matrix element of the potential between a final free state and the full scattering state. Since these states do not belong to the same orthogonal set, it is useful to express the scattering amplitude in terms of matrix elements between the initial and final free states. The set of matrix elements between free states is represented as

$$T_{k',k} \equiv \langle \phi_{k'} \left| T \right| \phi_k \rangle = \left\langle \phi_{k'} \left| V \right| \psi_k^{(+)} \right\rangle \tag{2.16}$$

also known as the T-matrix [Sat83]. The matrix elements give the probability

of the transition from a state with initial momentum $\hbar k$ to a state with final momentum $\hbar k'$, through interaction with the potential V. It is now possible to write the scattering amplitude in terms of a T-matrix element

$$f(\theta) = -2\pi^2 \left(\frac{2\mu}{\hbar^2}\right) T_{k'k}. \tag{2.17}$$

2.2 Distorted Wave Born Approximation

Previously in this chapter the Hamiltonian was written as the sum of the kinetic energy and interaction potential. In some cases it is advantageous to write the potential as the sum of two terms, $V(r) = V_1(r) + V_2(r)$, when the scattering solution for $V_1(r)$ can easily be solved for or is already known and is the dominant term in the potential. It is then possible to treat the weaker potential of interest, $V_2(r)$, as a perturbation to the solution for $V_1(r)$ alone. The T-matrix can now be written as $T_{k',k} \equiv \left\langle \phi_{k'} \left| V_1(r) + V_2(r) \right| \psi_k^{(+)} \right\rangle$, which yields the more useful form,

$$T_{k',k} = \left\langle \chi_{k'}^{(-)} \left| V_1(r) \right| \phi_k^{(+)} \right\rangle + \left\langle \chi_{k'}^{(-)} \left| V_2(r) \right| \psi_k^{(+)} \right\rangle, \tag{2.18}$$

where $\psi_k^{(+)}$ are the exact solutions, $\phi_k^{(+)}$ are the plane waves, and $\chi_k^{(-)}$ are the distorted waves [Sat83].

The Distorted Wave Born Approximation (DWBA) scattering amplitude can be derived by combining Equation 2.17 and Equation 2.18 and replacing the exact solutions, $\psi_k^{(+)}$, with the distorted waves, $\chi_k^{(+)}$. The total amplitude is given by

$$f_{\mathrm{DWBA}}(\theta) = f_1(\theta) - 2\pi^2 \left(\frac{2\mu}{\hbar^2}\right) \int \mathrm{d}^3 r \; \chi_{k'}^{(-)\star}(r) V_2(r) \chi_k^{(+)}(r) \tag{2.19}$$

where $f_1(\theta)$ is the scattering amplitude due to $V_1(r)$ [Sat83].

For this approximation to be valid, $V_2(r)$ must be weak compared to $V_1(r)$. The approximation uses distorted waves instead of plane waves, and invokes the Born approximation because the potential is truncated at the first term which is linear in $V_2(r)$. The scattering amplitude can be written specifically for inelastic channels. $V_1(r)$ is an optical potential chosen to describe the elastic channel and $V_2(r)$ is the potential that induces the inelastic transition. The approximation remains valid provided that elastic scattering is the dominant interaction and the inelastic channel can be treated as a perturbation. For the inelastic channel, the scattering amplitude can be written as

$$f_{\mathrm{DWBA}}^{\mathrm{inel}}(\theta) = -2\pi^2 \left(\frac{2\mu}{\hbar^2}\right) \int \chi_f^{(-)\star}(k_f, r_f) \, \langle b, B \, | V_{\mathrm{int}} | \, a, A \rangle \, \chi_i^{(+)}(k_i, r_i) \mathrm{d}^3 r_i \mathrm{d}^3 r_f \tag{2.20}$$

where the entrance channel $i = a + A$ and exit channel $f = b + B$ both describe elastic scattering off of optical potentials V_i and V_f respectively [Sat83]. The potential V_{int} induces the inelastic transitions and depends on the type of reaction and the model chosen to describe it.

2.2.1 Optical Model Parameters

The potential $V_1(r)$ accounts for the many-body problem of elastically scattering composite particles. In order to simplify the problem, the potential is customarily described by an optical model potential. The optical model potentials are in general complex and use the Woods-Saxon form [Per76],

$$V_2(r) = V_c + V_{vol}(x_{Vvol}) + \left(\frac{\hbar}{m_\pi c}\right)^2 V_{so}(l\cdot s)\frac{1}{r}\frac{d}{dr}f(x_{so}) - i\left[W_{vol}f(x_{Wvol}) - 4W_D\frac{d}{dx_D}f(x_D)\right] \quad (2.21)$$

where,

$$V_c = \begin{cases} ZZ'e^2/r, & \text{if } r \geqslant R_c \\ (ZZ'e^2/2R_c)(3 - r^2/R_c^2), & \text{if } r < R_c \end{cases} \quad (2.22)$$

$$R_c = r_c A^{1/3}, \quad (2.23)$$

$$f(x_i) = (1 + e^{x_i})^{-1}, \quad (2.24)$$

$$x_i = (r - r_i A^{1/3})/a_i. \quad (2.25)$$

In Equation 2.21, the terms represent the Coulomb, V_c; real volume, V_{vol}; spin-orbit, V_{so}; and imaginary volume, W_{vol}, and surface, W_D, potentials in the

optical model parameterization. For each term, the potential radius and diffuseness parameters are given by r_i and a_i respectively. The radius is defined as the distance from at which the potential drops to half of its central value [Kra87]. The diffuseness is defined as the distance over which the central value of the potential drops from 90% to 10% [Kra87]. The real terms are sufficient to describe the elastic scattering channel, and the imaginary terms are used to incorporate inelastic channels. Typically, the imaginary volume term is set to zero, and the imaginary surface term alone accounts for absorption.

Ideally, the optical model parameters for both the entrance and exit channels would be determined by studying the elastic channel on an isotope by isotope basis. Simultaneously fitting the parameters to elastic scattering data for a given isotope over a range of different beam energies would provide a sound parameterization. However, this is not always practical, especially for radioactive isotopes that would require inverse kinematics studies. Instead, a global parameterization is performed by studying elastic scattering data on stable isotopes over a large range of both proton and mass number in addition to a range of beam energies [Sat83]. It is important to note that the optical model parameters cannot be reliably extracted from data at a single beam energy. Otherwise, the parameters could be extracted from elastic scattering data during a transfer reaction experiment.

The present study employed the optical model parameterizations from Lohr-Haeberli [Loh74], Koning-Delaroche [Kon03], and Chapel-Hill 89 [Var91]. These values are summarized in Tables 4.2, 4.3, and 4.4. The Lohr-Haeberli parameterization included elastic scattering of polarized deuterons at energies of 9, 11, and 13 MeV off of eight heavy targets ranging from ^{27}Al to ^{120}Sn. The analysis also included previous elastic scattering data on 18 isotopes for deuteron energies between 5 and 12.3 MeV.

Two different optical model parameterizations were used for proton and neutron elastic scattering. The Koning-Delaroche parameterization utilized proton and neutron elastic scattering data off of heavy targets ranging from ^{24}Mg and ^{209}Bi at proton and neutron energies ranging from 1 keV up to 200 MeV. Among the targets used in the parameterization were both natural tin and ^{124}Sn. The other optical model parameterization for proton and neutron elastic scattering was Chapel-Hill 89. The study included data from over 300 isotopes with mass numbers ranging from 40 to 209, protons energies of 16 to 65 MeV, and neutron energies of 10 to 26 MeV.

2.3 Adiabatic Wave Approximation

The DWBA formalism described in the previous section is a powerful tool for calculating certain reaction cross sections. However, it has well-known limitations

such as neglecting deuteron breakup. For nuclear reactions it is often preferable to choose beam energies above the Coulomb barrier, so as to probe the surface and interior of the nucleus. Given that the deuteron binding energy is 2.22 MeV, for heavy nuclei where the Coulomb barrier is relatively high it is expected that deuteron breakup will be present.

The ADiabatic Wave Approximation (ADWA) has been introduced as an alternative to DWBA. ADWA explicitly treats the case of deuteron breakup and has been shown to be very accurate when compared to the exact solution for (d,p) and (p,d) reactions [Nun11]. Johnson and Soper first proposed the zero-range ADWA formalism which introduces a three body wavefunction for the channel with a deuteron [Joh70, Joh72]. The transition matrix, T_{ADWA} for the (d,p) reaction is given by

$$T_{ADWA} = \left\langle \chi_p^{(-)}(\mathbf{r_p})\phi_{\mathbf{n}}(\mathbf{r_n}) \left| \mathbf{V_{np}} \right| \psi^{(+)} \right\rangle \tag{2.26}$$

where $\chi_p^{(-)}$ is the proton distorted wave in the exit channel, $\phi_n(\mathbf{r_n})$ is the bound state of the neutron, V_{np} is the neutron-proton interaction, and $\psi^{(+)}$ is the three body wavefunction in the incident channel that satisfies the equation

$$\left[E - T_R - T_r - V_{np} - V_n\left(\mathbf{R} + \frac{1}{2}\mathbf{r}\right) - V_p\left(\mathbf{R} + \frac{1}{2}\mathbf{r}\right) - V_c(R) \right] \psi^{(+)}(\mathbf{r}, \mathbf{R}) = 0. \tag{2.27}$$

The coordinates are given by the vectors $\mathbf{R} = (\mathbf{r_p} + \mathbf{r_n})/2$, the position of the center of mass of the neutron and proton relative to the target, and $\mathbf{r} = (\mathbf{r_p} - \mathbf{r_n})$, the position of the neutron relative to the proton. The total energy is given by $E = E_d - \epsilon_0$ where E_d is the incident deuteron kinetic energy and ϵ_0 is the binding energy of the deuteron. V_n and V_p are the nucleon optical model potentials taken at half the kinetic energy of the incident deuteron, and V_c is the Coulomb potential.

In the Adiabatic Approximation the three body wavefunction is written as

$$\psi^{(+)} = P_0\psi^{(+)} + Q_0\psi^{(+)} \tag{2.28}$$

where $P_0 = |\phi_0\rangle \langle\phi_0|$ and $Q_0 = 1 - P_0$ are the projection operators and $|\phi_0\rangle$ is the deuteron ground state. In DWBA the second term in Equation 2.28 is not included. The projection operators are determined by the deuteron elastic scattering wavefunction, χ_0, which is determined by an optical model potential. Thus, the operators can be defined by

$$P_0\psi^{(+)}(\mathbf{r}, \mathbf{R}) = \phi_0(\mathbf{r})\chi_0(\mathbf{R}). \tag{2.29}$$

The Adiabatic Approximation assumes that $\epsilon_k - \epsilon_0 \approx 0$, allowing the substitution $\epsilon_0 \rightarrow \epsilon_k$ in Equation 2.27, where ϵ_k represents the internal eigenenergies.

Because V_{np} is zero-range, the approximation requires that the neutron and proton do not drift apart beyond this range in the time it takes the deuteron to transit the nucleus. Thus, the term adiabatic indicates that the neutron-proton internal velocities are slow compared to the relative motion of their center of mass.

Yet another improvement to nuclear reaction theory was made by the Finite-Range ADWA (FR-ADWA) formalism developed by Johnson and Tandy [Joh74]. Again the proton and neutron optical model parameters are chosen at half the kinetic energy of the incident deuteron, but now the sum of the potentials is averaged over the neutron-proton interaction, V_{np}. In the finite range case, Equation 2.27 is now written as

$$\left[E + i\epsilon - T_R - T_r - V_n\left(\mathbf{R} + \frac{1}{2}\mathbf{r}\right) - V_p\left(\mathbf{R} + \frac{1}{2}\mathbf{r}\right) - V_{np}(\mathbf{r})\right]\psi^{(+)}(\mathbf{r}, \mathbf{R}) = i\epsilon\phi_d(\mathbf{r})e^{i\mathbf{K}_d\cdot\mathbf{R})}. \quad (2.30)$$

In the finite-range treatment, the goal is to discretize the neutron-proton spectrum by an expansion of $\psi^{(+)}$ in terms of the Weinberg eigenstates defined by

$$\left[-\epsilon_d - T_r - \alpha_i V_{np}(\mathbf{r})\right]\phi_i = 0 \qquad i = 1, 2, 3, ... \quad (2.31)$$

where $\langle\phi_i\left|V_{np}\right|\phi_j\rangle = -\delta_{ij}$. The first member of the set is the bound state

of the deuteron, which implies that $\phi_1 \approx \phi_d$ and $\alpha_1 = 1$. The expansion of the wavefunction in terms of Weinberg states is given by

$$\psi^{(+)}(\mathbf{r}, \mathbf{R}) = \sum_{i=1}^{\infty} \phi_i(\mathbf{r}) \chi_i^{(+)}(\mathbf{R}). \tag{2.32}$$

Introducing the expansion into Equation 2.30 leads to N coupled-channel two-body Schrödinger equations. It is assumed that truncating to the first term in the expansion is accurate, and thus a single equation remains:

$$[E_d + i\epsilon - T_R - V_{11}(\mathbf{R})] \left| \chi_1^{(+)} \right\rangle = i\epsilon N_d \left| \mathbf{K}_d \right\rangle \tag{2.33}$$

where $N_d = -\left\langle \phi_1 \right| V_{np} \left| \phi_d \right\rangle$ and $\mathbf{K}_d$ is the momentum operator for the deuteron. In the FR-ADWA the adiabatic potential used for V_{11} is given by

$$V_{FR-ADWA} = \frac{\left\langle \phi_d \right| V_{np}(V_n + V_p) \left| \phi_d \right\rangle}{\left\langle \phi_d \right| V_{np} \left| \phi_d \right\rangle}. \tag{2.34}$$

The neutron and proton optical model potentials are folded with the neutron-proton interaction and averaged over the deuteron wavefunction.

2.4 Spectroscopic Factors and Asymptotic Normalization Coefficients

In Chapter 1 the nuclear shell model was presented with simple single-particle states. However, in reality, nuclear states will mix producing states with similar spins and parities. The creation of mixed states with the same spin and parity as a single-particle state serves to fragment the single-particle strength of a given state. The fragmentation can be quantified by a spectroscopic factor, defined as the square of the norm of the overlap function for a transfer reaction $A(d,p)B$:

$$S^B_{A\ell j} = |A_{\ell j}|^2 \tag{2.35}$$

where $A_{\ell j}$ is the spectroscopic amplitude used to describe the overlap function given by

$$\phi^B_{A\ell j} = \sum_{\ell j} A_{\ell j} \varphi^B_{A\ell j} \tag{2.36}$$

and $\varphi^B_{A\ell j}$ is the single-particle wave function [Sat83].

In practice, spectroscopic factors are determined experimentally from reaction theory. It is common for reaction theory calculations to assume a spectroscopic factor of 1. Thus, by normalizing the theoretical differential cross section to the experimental differential cross section it is possible to extract the spectroscopic

factor ($S_{\ell j}$) of a state with orbital angular momentum ℓ and total angular momentum j [Tho05, Tho07]:

$$\left(\frac{d\sigma}{d\Omega}\right)_{exp} = S_{\ell j}\left(\frac{d\sigma}{d\Omega}\right)_{rxn\ theory} \tag{2.37}$$

Of course, the spectroscopic factor is not an observable and is heavily dependent on reaction theory. Specifically, the choice of optical model parameters, reaction formalism, and bound state geometry of the neutron will greatly influence the amplitude of the theoretical differential cross section and, hence, the spectroscopic factor.

In addition to being model dependent, theoretical spectroscopic factors are largely determined by the interior of the nucleus, despite low energy transfer reactions being mostly peripheral [Tho07]. Therefore, it might be dubious to extract spectroscopic factors from such reactions. Regardless, it is possible to extract a quantity that is model independent and sensitive to the tails of the nuclear wave function [Muk01]. The asymptotic normalization coefficient (ANC) is such a quantity that depends on the radial part of the overlap function,

$$R^B_{A\ell j}(r) \overset{r>R_n}{\longrightarrow} C^B_{A\ell j}\ ik\ h^{(1)}_\ell(ikr) \tag{2.38}$$

where $h^{(1)}_\ell(ikr)$ is a spherical Hankel function of the first kind, k is the wavenumber, and $C^B_{A\ell j}$ is the ANC associated with the reaction $A(d,p)B$ [Muk01].

The ANC is the amplitude of the tail of the bound-state overlap function. For (d,p) reactions the ANC can be interpreted as the probability of finding the transferred neutron in the nuclear exterior region of the final nucleus B [Muk01]. The single-particle bound-state wavefunction can also be expressed in the limit of the nuclear exterior,

$$\phi^B_{A\ell j}(r) \overset{r>R_n}{\longrightarrow} b^B_{A\ell j}\; ik\; h^{(1)}_\ell(ikr) \tag{2.39}$$

where $b^B_{A\ell j}$ is defined as the single-particle ANC [Muk01]. The single-particle ANC can be calculated from the bound-state potential, usually a Woods-Saxon shape with standard radius ($r = 1.25$ fm) and diffuseness ($a = 0.65$ fm) [Tho09, Jon11]. Since the radial part of the overlap function is assumed to be described by the single-particle bound-state wavefunction and the spectroscopic factor [Muk01],

$$R^B_{A\ell j}(r) \approx \sqrt{S_{\ell j}}\; \phi^B_{A\ell j}(r), \tag{2.40}$$

the square of the ANC can be written as the product of the spectroscopic factor and the square of the single-particle ANC,

$$\left(C^B_{A\ell j}\right)^2 = S_{\ell j}\left(b^B_{A\ell j}\right)^2. \tag{2.41}$$

Even though spectroscopic factors are model dependent, they can be used to

calculate an ANC which is independent of model parameters for peripheral reactions.

2.5 Neutron Capture

Compound nuclear capture is the dominant mode of neutron capture. Cross sections for this reaction are often calculated using a statistical model such as Hauser-Feshbach [Hau52]. This approach works well for most heavy nuclei where the level density is sufficiently high and it is possible to average over many closely spaced resonances and states. However, near neutron shell closures the level density near the neutron separation energy decreases and it is expected that direct-semidirect neutron capture will become the dominant mode [Moh12].

It is possible to describe direct capture (DC) using a formalism similar to that used in the previous section. The direct capture cross section of a neutron, n, by a target nucleus, A, to yield nucleus B in state i is given by [Kra96]

$$\sigma_i^{th} = \int d\Omega \; d\sigma_i^{th}/d\Omega_\gamma. \tag{2.42}$$

More formally, the cross section is

$$\sigma_i^{th} = \int d\Omega \, 2 \left(\frac{e^2}{\hbar c}\right) \left(\frac{\mu c^2}{\hbar c}\right) \left(\frac{k_\gamma}{k_n}\right)^3 \frac{1}{2I_A+1} \frac{1}{2S_n+1} \times \sum_{M_A M_n M_B, \sigma} |T_{M_A M_n M_B, \sigma}|^2 \tag{2.43}$$

where i is the state of the nucleus B, S_n and I_A (M_n , M_A , and M_B) are the spins (projections) of the corresponding nuclei, μ is the reduced mass in the entrance channel, σ is the polarization of the electromagnetic radiation (± 1), k_γ is the momentum of the emitted radiation, k_n is the entrance channel relative momentum, and T is the multipole expansion of the electromagnetic transition amplitude. The total direct neutron capture cross section, σ^{DC} can then be calculated by summing over the product of the individual theoretical capture cross sections for each state, σ^{th}, and the corresponding spectroscopic factors S_{lj}^i [Kra96].

$$\sigma^{DC} = \sum S_{lj}^i \sigma_i^{th} \tag{2.44}$$

A more sophisticated formalism is required to describe the direct-semidirect neutron capture used in modern calculations [Par95, Arb05]. Since E1 transitions are significantly faster than other electromagnetic transitions [Won04], we will limit further derivations to electric dipole transitions described by the density form of the electromagnetic operator. We will restrict the calculations to capture of spin 1/2 nucleons on a spin-0 target. Furthermore, it is assumed that the capture states are entirely single-particle in nature and characterized by quantum

numbers n_f, l_f, and j_f .

The density form of the radial electric operator is given by

$$O_L = e_{\text{eff}}\, r^L \tag{2.45}$$

where e_{eff} is the kinematic effective charge defined as

$$e_{\text{eff}} = (-1)^L Z \left(\frac{1}{A+1}\right)^L + z\left(\frac{1}{A+1}\right)^L \tag{2.46}$$

where Z is the charge of the target, A is the mass of the target, and z is the charge of the projectile. The direct component just described is akin to a transfer reaction. However, the semidirect component proceeds by the projectile exciting the giant dipole resonance. The semidirect component of neutron capture is included via the operator

$$O_L^{DSD} = \sum_T h'_{LT}(r)\left(\frac{1}{E_\gamma - E_{LT} + i\Gamma_{LT}/2} - \frac{1}{E_\gamma + E_{LT}}\right) \tag{2.47}$$

where E_{LT}, Γ_{LT}, L, and T are the position, width, multipolarity, and isospin of the giant dipole resonance, respectively, and h_{LT} is the form factor for describing isovector excitations due to vibrations of the proton and neutron fluids. Once the operators are defined, it is possible to calculate the capture amplitudes for electric dipole transitions, $G_c^{n_f l_f j_f}$, for each channel. Then the cross section for capture to each state is defined as

$$\sigma_\gamma^{n_f l_f j_f} = 4\pi\alpha \frac{\mu c^2}{\hbar c} \frac{k_\gamma}{k_i^3} \sum_c (2j+1) \left| G_c^{n_f l_f j_f} \right|^2 \tag{2.48}$$

where α is the fine structure constant, μ is the reduced mass of the system, k_γ is the gamma-ray wave vector, and k_i is the wave vector for the captured neutron. Finally, the total neutron capture cross section can be written as the sum of capture cross sections into all available states with quantum numbers nlj,

$$\sigma_\gamma = \sum_{nlj} \frac{2J_f + 1}{2J_i + 1} \frac{S_{nlj}}{2j+1} \sigma_\gamma^{nlj} \tag{2.49}$$

where S_{nlj} is the spectroscopic factor associated with the given state.

Chapter 3

Experimental Details

3.1 Beam Production

All of the beams in this experiment were produced at the Holifield Radioactive Ion Beam Facility (HRIBF) at Oak Ridge National Laboratory (ORNL). The HRIBF produced radioactive ion beams with the isotope separation-online (ISOL) technique [Str04]. A schematic of the HRIBF is shown in Figure 3.1. A beam of protons from the Oak Ridge Isochronous Cyclotron (ORIC) impinge upon a thick uranium carbide (UC_x) target inducing fission of the uranium. The target-ion source where the UC_x target is located is on a platform held at -200 kV. The fission fragments diffuse through the target material and follow a transport line to an electron-beam-plasma ion source (EBPIS) where they are ionized [Car97]. An extractor held at -40 kV relative to the platform accelerates positive ions exiting the plasma [HRI14]. A mass analyzing magnet ($\Delta M/M \approx 1/2500$) purifies the beam for the desired mass. The beam passes through a cesium-vapor charge-exchange cell producing negative ions as required for injection into the 25 MV tandem electrostatic accelerator. Contaminants are magnetically separated ($\Delta M/M \approx 1/10000$ to $1/20000$) from the beam after the charge-exchange

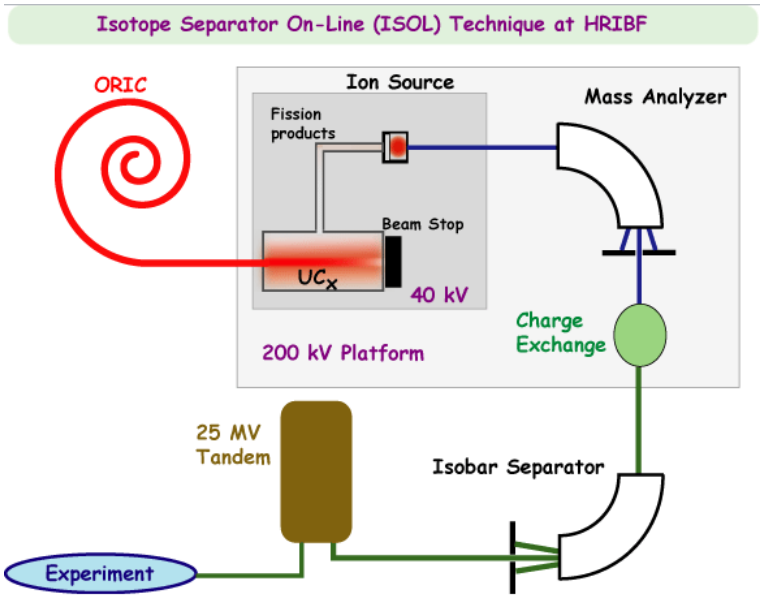

Figure 3.1: Schematic of the HRIBF beam production. Figure taken from [HRI14].

cell. The negative ions enter the low energy side of the tandem where they are accelerated to the positively-charged terminal. At the positive terminal the ions pass through a carbon stripper foil which strips electrons from the ions leaving them positively-charged. The beam is sent around a 180° bending magnet and accelerated down the high energy side of the tandem. There is an additional carbon stripper foil one third of the way down the high energy side of the tandem. If used, this foil can remove additional electrons to accelerate the beam particles to higher energies. The beam passes through slits before being delivered to the experimental room. For this experiment, the positive terminal voltage of the tandem was held at ∼24 MV, and the beam was double stripped to achieve a total energy of 630 MeV for all beams. For the beams of ^{124}Sn, ^{126}Sn, and ^{128}Sn, the energies were 5.1 MeV/A, 5.0 MeV/A, and 4.9 MeV/A respectively.

A technique has been pioneered at the HRIBF to purify beams of group 4A elements of the periodic table such as Sn and Ge [Str03]. During beam production for this experiment, hydrogen sulfide (H_2S) gas was injected into the ion source transfer line prior to the EBPIS. The gas binds to Sn ions in the transport line forming tin-sulfide (SnS) molecules more often than other fission fragments of similar mass. The SnS molecules are then treated as any other particle. The mass analyzing magnet was configured to transport $A = 156, 158, 160$ for the beams of ^{124}Sn, ^{126}Sn, and ^{128}Sn, respectively. Contaminants with similar mass are unlikely to form sulfide molecules and, therefore, are removed from the beam. The SnS molecules are broken up in the charge-exchange cell leaving negative Sn ions. Beam intensities of about 35,000 pps of ^{128}Sn, 100,000 pps of ^{126}Sn, and 250,000 pps of ^{124}Sn were observed in the present study.

3.2 Targets

Thin foils of deuterated polyethylene $(CD_2)_n$ were prepared as targets for this experiment by the author. Powdered deuterated polyethylene is dissolved into p-xylene. The mass of polyethylene is determined in relation to the surface area and the desired thickness of the foil. The concentration of the solution should be approximately 0.5 mg/mL. For instance, to produce a 100 μg/cm^2 foil on a substrate with a surface area of 10 cm^2, one would dissolve 1 mg of polyethylene into 2 mL of p-xylene. The solution is heated in a covered beaker to the boiling

point ($\sim$ 145°C) and continues to boil for one hour. Once the boil is complete, the solution is removed from the heat and allowed to cool to about 125° C. Next the solution is poured into a shallow petri dish. The dish should be mostly covered in order to slow the evaporation of p-xylene. Once all of the solvent has evaporated away, a polymerized layer of CD_2 will be left on the bottom of the petri dish. To remove the targets one should first score the edges of the desired target. Warm water is carefully poured into the petri dish to help separate the foil from the glass substrate. The foil will float to the surface of the water in about 5 minutes. The thin foil is then poured into a deep dish with warm water. The target frame should be submerged below the floating foil and slowly raised out of the water at a 45° angle. The thin foil will adhere to the frame where it should be allowed to dry. A small amount of liquid adhesive may be applied to the corners of the foil for thicker targets to ensure a solid bond between frame and foil.

We have found that boiling the solution for a full hour reduces surface fluctuations on the foil. It may also be worthwhile to anneal the target by baking it for about 5 minutes in an oven at 110° C. The annealing process may improve the polymerization of the CD_2 thus making the target less brittle. These points represent new results that may prove very useful for future experiments. We have used this technique to develop targets for studying the $^{86}\mathrm{Kr}(d,p)$ reaction in inverse kinematics. The author played a central role in these advances.

Figure 3.2: Deuterated polyethylene targets mounted on target drive for ^{124,126,128}Sn(d,p) reaction measurements at the HRIBF. Below the targets a phosphor is mounted for tuning the beam to the target chamber.

Although the foil thickness is estimated by the mass of powdered polyethylene and the surface area of the petri dish, some of the powder is lost during the process. The thickness of each foil was verified by examining the energy loss of α particles passing through the target. A ^{244}Cm source emitted α particles with an energy of 5.805 MeV. These particles were detected in a silicon detector to measure the full energy. A single foil was placed in between the source and the detector, and the energy of the α particles passing through the foil were measured. The energy loss, ΔE, of charged particles through a material is the product of the stopping power dE/dx and the thickness x [Kra87]:

$$\Delta E = -\frac{dE}{dx} \cdot x. \tag{3.1}$$

The stopping powers for α particles through polyethylene are well-known

within the resolution of the silicon detectors [Ber00]. The foils used in this experiment were measured to be 139±17 μg/cm^2 and 242±29 μg/cm^2. A photograph of these targets mounted for the experiment is shown in Figure 3.2.

3.3 Detectors

To study the (d, p) reaction on radioactive nuclei it is necessary to perform the experiment in inverse-kinematics. For heavy ion beams like those used in this experiment, beam-like particles will be forward focused and elastically scattered target particles will be forward of 90°. Reaction protons will be emitted at all angles, but the reaction cross section is typically highest near 90°. Given the kinematics of this experiment, it is critical to have a large solid angle charged particle detector array immediately backward of 90° where the reaction cross section is high and there are no elastically scattered target particles. Near 0° in the center of mass frame the elastic cross section can be described by Rutherford scattering; thus it is also important to have charged particle detectors just forward of 90° in the lab frame so as to detect elastically scattered target particles for beam normalization. A gas-filled ionization chamber at 0° can measure the heavy beam-like particles in coincidence with light particles in the charged particle detectors. Figure 3.3 depicts the detector setup used in this experiment.

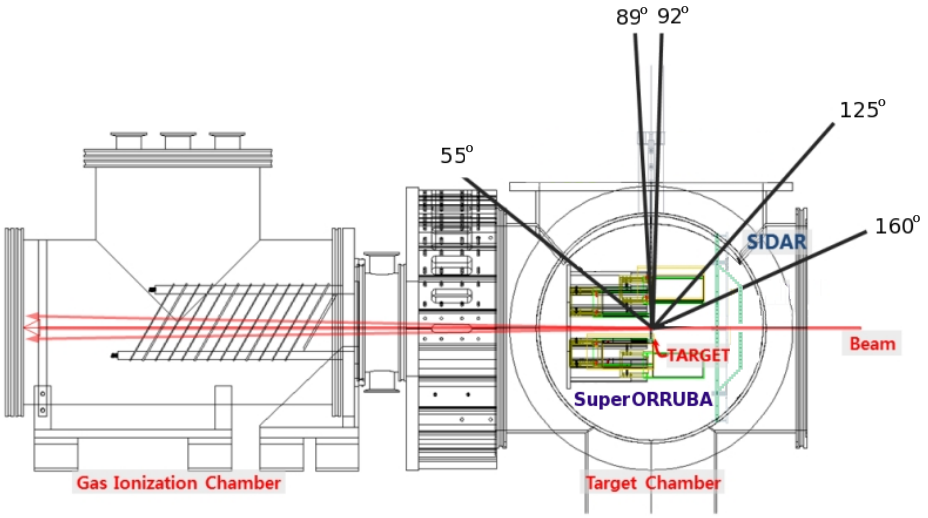

Figure 3.3: Schematic of detectors used in ^{124,126,128}Sn(d,p) reactions measured in inverse kinematics. A gas-filled ionization counter was placed at 0° to detect beam-like particles. Two silicon detectors from the SuperORRUBA array covered angles from 55°-89°, and eight more of these detectors covered angles from 92°-125°. Six silicon detectors from the SIDAR array covered the extreme backward angles from 125°-160°. Figure modified from [Ahn13].

3.3.1 Silicon Detectors

As a charged particle passes through a semiconductor, it ionizes the material producing many electron-hole pairs along its path. The advantage of using semiconductors to detect charged particles is that the energy required to produce a single electron-hole pair, termed the ionization energy, is about 3 eV as compared to about 30 eV in gas-filled detectors [Kno10]. Thus, the signal produced by semiconductors is about one order of magnitude greater than the signal produced by a gas-filled detector for similar incident radiation. The increased number of charge carriers for semiconductors provides better signal to noise ratio which is imperative for detecting low energy radiation.

It is common to make a charged particle detector by forming a reversed biased diode from two pieces of doped semiconductor. Charge carriers migrate across the junction of the n-type semiconductor, with an excess of electrons, and the p-type semiconductor, with an excess of holes. As electrons move to the p-type material, a net negative space charge builds up on the p side. Conversely, as holes move to the n-type material a net positive space charge forms on the n side of the junction. An electric field is formed between the two net spaces charges slowing the migration of charge across the junction. The volume of material spanned by the electric field is known as the depletion region [Kno10]. Applying a reverse bias to the junction can extend the electric field over the entirety of the material. Doing so ensures that any electron-hole pairs created by incident radiation will interact with the electric field. The free electron-hole pairs are swept to anodes present at the boundaries of the n-type and p-type materials. Measuring the charge collected on either anode provides a method for determining the energy deposited by the incident radiation.

SuperORRUBA

The SuperORRUBA (Super Oak Ridge Rutgers University Barrel Array) [Bar13b] is designed to have 2 rings of the BB15 style non-resistive double-sided silicon strip detectors as shown in Figure 3.4. Typically one ring each would be positioned immediately forward and backward of 90°. Each BB15 style detector has

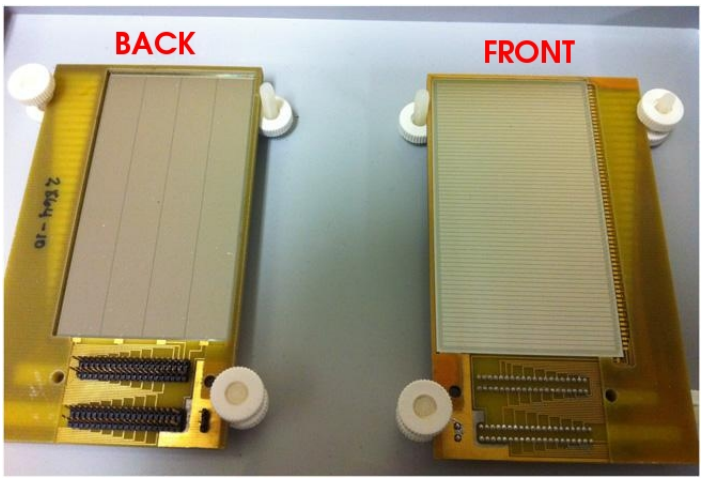

Figure 3.4: BB15 style detector used in the SuperORRUBA array. Each detector has 64 non-resistive silicon strips on the front side and 4 non-resistive silicon strips on the back side.

an active area 7.5 cm $\times$ 4 cm. The front side of the detector is divided into 64 1.2 mm $\times$ 4 cm strips, and the back side is divided into 4 7.5 cm $\times$ 1 cm strips. The front side strips were oriented perpendicular to the beam direction while the back side strips were parallel. For this experiment there were 2 BB15 detectors in the forward ring covering 55°-89° and 8 BB15 detectors in the backward ring covering 92°-125°. All of the BB15 detectors were about 1000 μm thick.

SIDAR

The SIDAR (SIlicon Detector ARray) [Bar01] is composed of 6 MSL-type YY1 detectors with 16 annular silicon strips per detector. Figure 3.5 shows the MSL-type YY1 detectors used in the SIDAR. The SIDAR was configured into its "lampshade" configuration where the 6 detectors were tilted 43° from perpendicular to the beam axis and evenly spaced azimuthally. The SIDAR covered the most

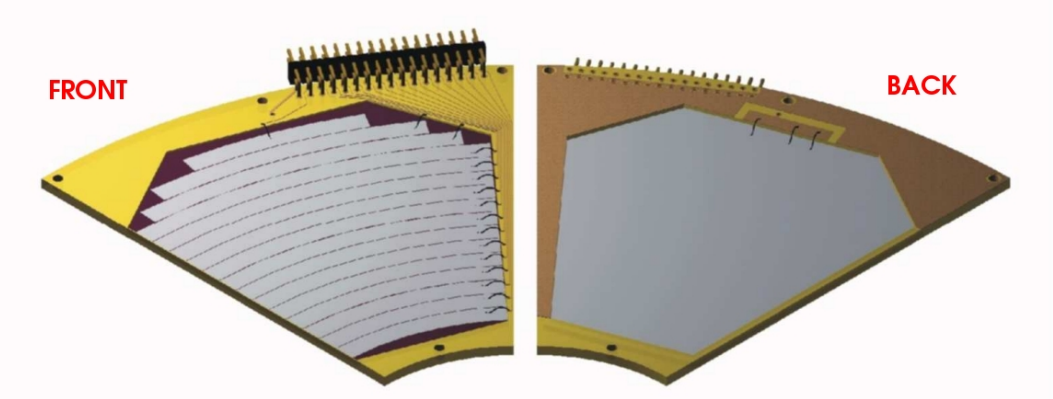

Figure 3.5: MSL-YY1 style detector used in the SIDAR array. Each detector has 16 annular non-resistive silicon strips on the front side and the back side is a single silicon pad.

backward angles from 125°-160°. All of the MSL-type YY1 detectors were about 100 μm thick.

3.3.2 Ionization Counter

An ionization counter (IC) was placed at 0° immediately downstream of the target chamber. The IC served several purposes during this experiment. First, it was used as a beam monitor to count the number of particles on target in real time. ^{126}Sn and ^{128}Sn are both radioactive, and it can be difficult to produce high beam currents for these nuclei. It was critical to maintain the highest beam current possible to maximize the yield of reaction protons during the allotted beam time. Additionally, the IC provides a means for determining the total number of beam particles on target during the entirety of the experiment. The total number of beam particles on target is used to calculate absolute normalization for the (d, p) differential cross sections.

Secondly, the first anode of the IC provided a timing signal used for establishing coincidences with protons detected in the silicon detectors. There will be many random events detected in the silicon detectors, but protons from the (d, p) reaction detected in the silicon detectors will be time correlated with the heavy recoil from the reaction detected in the IC.

The third purpose of the IC is to identify tin ions in the beam. Although the beams for this experiment were nearly 98% pure, any beam contaminants could produce reactions in the target with kinematics similar to the reaction of interest [Sha11]. Furthermore, fusion evaporation reactions could occur with the desired beam, however with different kinematics than transfer reactions. The IC provides a means for both confirming the purity of the beam and identifying the reaction of interest. However, for heavy beams with $A \sim 130$ the IC is not able to resolve species that differ in mass by one unit, as is the case for (d, p) reactions.

An IC is a gas-filled chamber that detects ionizing radiation. When a particle enters the chamber, it loses energy as it interacts with the gas. During this process the gas becomes ionized producing electrons and positive ions. An external electric field is applied between an anode and a cathode. The field sweeps the electrons to the anode and the positive ions to the cathode where the particles are collected. Drift times for electrons are typically 1000 times faster than for

positive ions [Kno10]. For high counting rates it is customary to integrate only the electron-induced signal collected on the anode, which is proportional to the energy deposited by the particle.

It is common to configure the IC as a $\Delta E/E$ telescope. Several anode signals can be combined near the front of the detector to measure the energy loss (ΔE) of the particle. The remaining anode signals are then combined to measure the residual energy (E) of the particle. Bethe's formula describes the energy loss of a charged particle passing through a material. The energy loss, dE/dx is given by [Kno10]

$$-\frac{dE}{dx} = \frac{4\pi e^4 z^2}{m_0 v^2} NZ \left[\ln\left(\frac{2m_0 v^2}{I}\right) - \ln\left(1 - \frac{v^2}{c^2}\right) - \frac{v^2}{c^2} \right] \tag{3.2}$$

where v and ze are the velocity and charge of the primary particle, N and Z are the number density and atomic number of the absorber atoms, m_0 is the electron rest mass, I is the average excitation and ionization potential of the absorber, and e is the electronic charge. For nonrelativistic particles ($v << c$) Equation 3.2 simplifies [Kno10] to

$$-\frac{dE}{dx} \propto \frac{mz^2}{E} \tag{3.3}$$

where m is the mass of the incident particle. The relation in Equation 3.3 can be used to identify beam particle and contaminants in an IC.

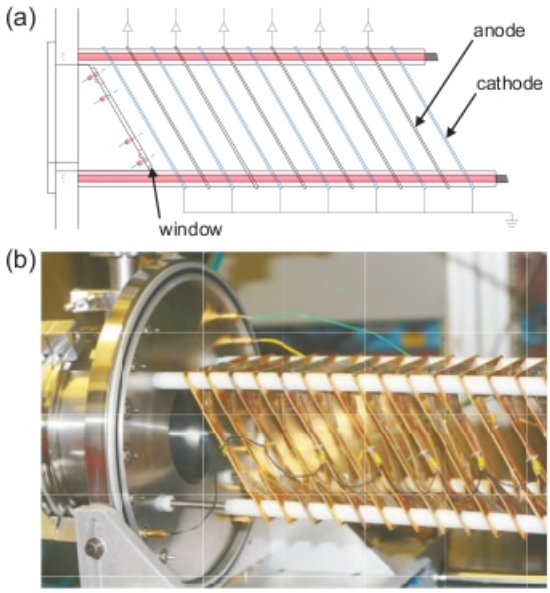

Figure 3.6: (a) Schematic of ionization chamber and (b) photograph of tilted anodes mounted in the chamber. Figure taken from [Cha14].

A new IC for high count rates was constructed and commissioned at the HRIBF prior to this experiment [Cha14]. A diagram of this design and a photograph are shown in Figure 3.6. To improve the response time of the detector, and hence the maximum counting rate, a tilted entrance window and tilted grid design were implemented. The grids are tilted 30° from perpendicular to the beam axis, which ensures the external field is not parallel to the beam path. The electrons and ions drift away from the beam axis which helps to reduce recombination. This design followed previous work [Kim05] from a group at RIKEN.

Additionally, to increase the counting rate, the electrodes are separated by 0.72 in. polyoxymethylene spacers. Due to the close proximity of the anode and

the cathode, the drift distance and time are very short for both electrons and ions. A short drift time increases the response time of the detector and allows for higher counting rates. This IC has demonstrated accurate counting up to ∼700,000 pps [Cha14].

For this experiment, the chamber was instrumented with 7 anodes and 8 cathodes. The first anode was used as a timing signal. Signals for the next two anodes were combined to measure the energy loss, ΔE, while the last four anode signals were combined to measure the residual energy, E of the stopped beam. The chamber was filled with tetrafluromethane (CF_4) because the gas has been shown to have fast relaxation times which allows for higher counting rates [Hun88, Chr79]. The gas pressure in the chamber was ∼75 torr. The timing anode was held at a voltage of 200 V while the other six anodes were held at 300 V.

3.4 Electronics

The high number of electronics channels in this experiment presented several challenges. A new analog electronics system using Application Specific Integrated Circuits (ASICs) [Ahn13] was implemented at the HRIBF before this experiment, but the present study was the first campaign to rely solely on the new system. Figure 3.7 shows a typical conventional electronics setup.

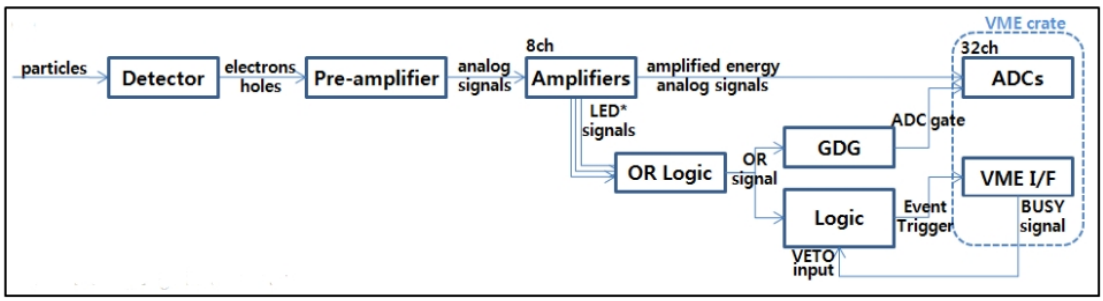

Figure 3.7: Typical conventional electronics setup for transfer reactions. Detectors output current pulses proportional to the energy deposited. Preamplifiers integrate the charge in the signal and produce a voltage pulse. The voltage pulse is amplified and shaped before being sent off to logic modules and ADCs. Figure taken from [Ahn13].

In the conventional electronics setup, an electrical current pulse is produced by the silicon detectors or ionization counter. A preamplifier integrates the current to produce a voltage pulse with amplitude proportional to the charge out of the detector. The signal out of the pre-amplifiers is only a few hundred mV and may have a long decay time which could lead to overlap of different signals. A shaping amplifier increases the amplitude of the voltage signal and ensures the signal has a quick decay time so that signals are less likely to overlap. The shaped signal is sent to a discriminator that can be configured to reject low amplitude signals that are likely to be electronic noise. Signals from the discriminator are sent to a logical OR module to create a trigger signal. The trigger signal is sent to a peak-sensing analog-to-digital converter (ADC) to create a gate for the peak-sensing ADC to read input signals. A copy of the signal from the discriminator is sent directly to the peak-sensing ADC and is digitized and recorded when a gate is received from the logical OR module. The peak-sensing ADC outputs a busy signal while it is reading data so that no other signals are recorded.

3.4.1 Application Specific Integrated Circuits

The physical space and cost of implementing the conventional electronics setup just described poses a problem for experiments with a large number of electronics channels. For such an experiment, it is worthwhile to use ASICs that combine the functionality of several modules described above into a single electronics chip. Each ASICs chip serves as shaping amplifier, discriminator, and peak detector [Ahn13]. Figure 3.8 shows a schematic diagram of the electronics setup configured with ASICs.

In Figure 3.8, an XLM (Xilinx Logic Module) is shown in the data stream. An XLM is a programmable logic module used to load DAQ (data acquisition) commands and initial setup parameters onto the ASICs motherboard and the ASICs chipboards. The XLM commands the ADC to save data when desired triggering conditions are satisfied. The module contains a field-programmable gate array (FPGA) allowing for easy modifications. A VME (Versa Module Europa) crate connects the XLM to the VME I/F module that reads data from the peak-sensing ADCs and transfers the data to a network connected computer.

Implementing an ASICs system presents many challenges and was part of the thesis work of Sunghoon Ahn [Ahn13]. A large number of files are required to

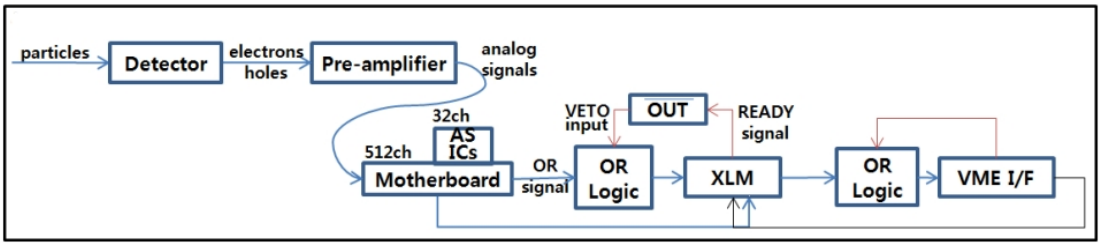

Figure 3.8: Schematic of electronics setup with ASICs implementation. The ASICs chips take the place of the shaping amplifiers and discriminators used in the conventional electronics setup. Figure taken from [Ahn13].

allow the data acquisition system to communicate with the ASICs system, the XLM, and the VME I/F. These files handle the communication between the systems necessary for triggering and storing data. Additional files are needed to load parameters into the XLM and ASICs system. Once the system is running the ASICs chipboards will put off a large amount of heat. It is imperative that some form of cooling is used. For these experiments fan cooling was used to maintain safe operating temperatures for the ASICs system. A common failure mode from overheating was a damaged voltage regulator on the motherboard, resulting in the loss of power to the board. It was also found that the chip boards could become damaged resulting in the loss of some channels on that chip. Cooling plates can be attached to the chip boards to reduce the probability of damage.

Chapter 4

Results

In this chapter we present a complete description of the analysis techniques required to convert raw particle energies measured in individual silicon strips into Q-value spectra for each reaction and ultimately differential cross sections for the observed states. As explained in similar studies [Jon11], the SIDAR was exposed to a small number of reaction protons due to covering extreme backward angles in the laboratory frame. Only for $\ell = 0$ transfers would we expect to detect many reaction protons at these angles. Consequently, the focus of this chapter is on the measurements with the BB15 SuperORRUBA detectors.

4.1 Silicon Detector Calibrations

Silicon detectors are commonly used for detecting charged particles such as protons from nuclear reaction experiments [Kno10]. These detectors have good intrinsic energy resolution and can be highly segmented to provide excellent angular resolution. Furthermore, the detectors can be made into arrays that cover large

solid angles and have high detection efficiencies. The last two points are critical for experiments with radioactive ion beams where beam intensities are often quite low. Still, it is critical to have sound calibration techniques to utilize the effectiveness of these detectors.

4.1.1 Energy Calibrations

Each electronics channel has its own gain and offset due to the preamplifier and the ADC. To properly measure the gain and offset, each channel must be calibrated with inputs of known energy. The ADCs used with the ASICs system have non-negligible energy offsets, so it is important to have several calibration points spanning a large range of energies.

Table 4.1: Decay energies and branching ratios for ^{244}Cm, ^{241}Am, and ^{239}Pu. These nuclei were used for the silicon detector energy calibrations [ENS11].

Isotope	Branching Ratio	Energy (MeV)
^{244}Cm	76.90%	5.805
	23.10%	5.763
^{241}Am	84.80%	5.486
	13.10%	5.443
^{239}Pu	70.77%	5.157
	17.11%	5.144

A common technique for calibrating silicon detectors is to measure alpha particles with a known energy in the detector of interest [Kno10]. A metallic disc electroplated with ^{244}Cm, ^{241}Am, and ^{239}Pu was inserted at the target position for the energy calibration. The energies and branching ratios of these nuclei are

shown in Table 4.1. Figure 4.1 shows the raw calibration data for a single front side strip in a BB15 style detector using the triple-alpha source described above.

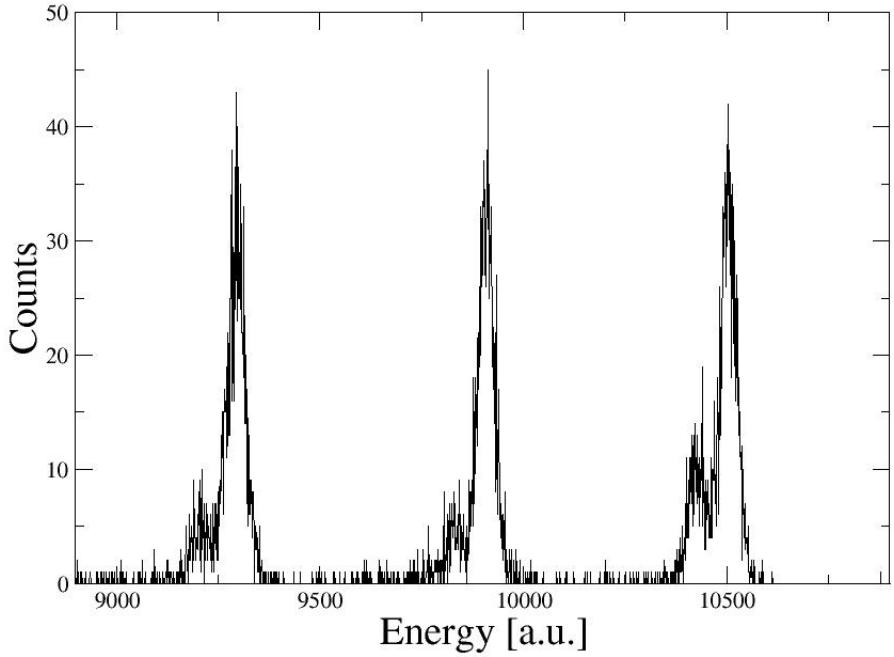

Figure 4.1: The alpha energy calibration data for a single front side strip of a BB15 style SuperORRUBA detector prior to the ^{124}Sn(d,p) experiment. The alpha source contained three different isotopes; ^{244}Cm, ^{241}Am, and ^{239}Pu. Table 4.1 summarizes the characteristics of these nuclei. In this figure the strip has not been calibrated, therefore, energy of each alpha peak is given by a channel number in the ADC.

The alpha data provide a nice set of calibration points at energies near the upper end of the dynamic range of the ADCs, but an electronic pulser is necessary to provide low energy inputs. Figure 4.2 shows data from a pulser. A signal of known energy is sent directly into the preamplifier and then treated just as a signal from the detector.

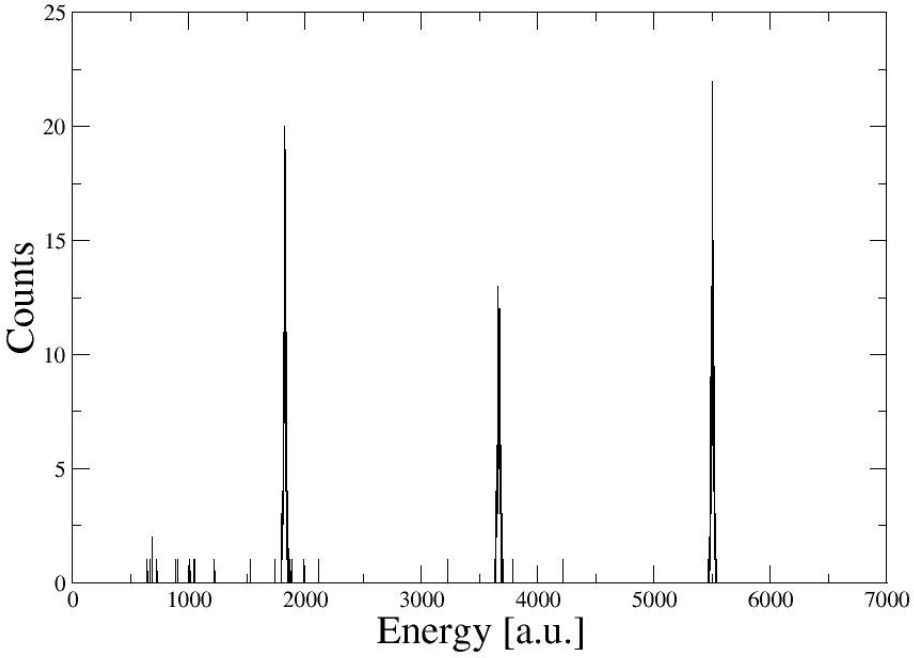

Figure 4.2: The pulser energy calibration data for a single front side strip of a BB15 style SuperORRUBA detector prior to the ^{124}Sn(d,p) experiment. The pulse heights of the three peaks are 115 mV, 225 mV, and 335 mV. The pulser provides energy calibration at much lower values than alpha sources and is thus quite valuable. In this figure the strip has not been calibrated so the energy of each pulser peak is given by a channel number in the ADC.

Combining the pulser and alpha data provide a complete set of calibration data. A linear regression of the calibration data provides a reliable measure of the gain and offset of each electronics channel. During our study we found that the addition of pulser data made little impact on the final gains and offsets when compared to the values calculated solely from the alpha data. Still, it is recommended to incorporate pulser data to confirm the linearity of the ADCs, and to ensure the calibration spans the full dynamic range of the ADCs.

Once the detector has undergone a basic energy calibration, each electronics channel should have the same input voltage to the ADC for a given signal. Figure 4.3 shows the results of applying gain calibrations to a BB15 style detector in the SuperORRUBA at the conclusion of the ^{124}Sn(d,p) experiment. The plots depict the energy of the incident signal as a function of strip number on the detector. Prior to the gain calibrations, the dominant alpha peaks for each source shown in Table 4.1 appear at different voltage inputs to the ADC as displayed in the top panel. However, once the gain calibrations are applied, each alpha peak manifests at the same voltage input in each electronics channel as seen in the bottom panel.

4.1.2 Angle Determination

The laboratory polar angle of each silicon strip in the SuperORRUBA can be determined from the geometry of the array relative to the target position. For the backward ring of BB15 detectors in the SuperORRUBA, the strip angle is given by

$$\theta_{\text{backward}} = 90^{\circ} + \tan^{-1}\left[\frac{w * j + d_1}{r_1}\right], \tag{4.1}$$

where w is the width of the strip, d_1 is the projection along the $z-$axis of the distance from the target to the nearest front side strip on the detector, j is the strip number, and r_1 is the radius of the array of detectors. Similarly, for the

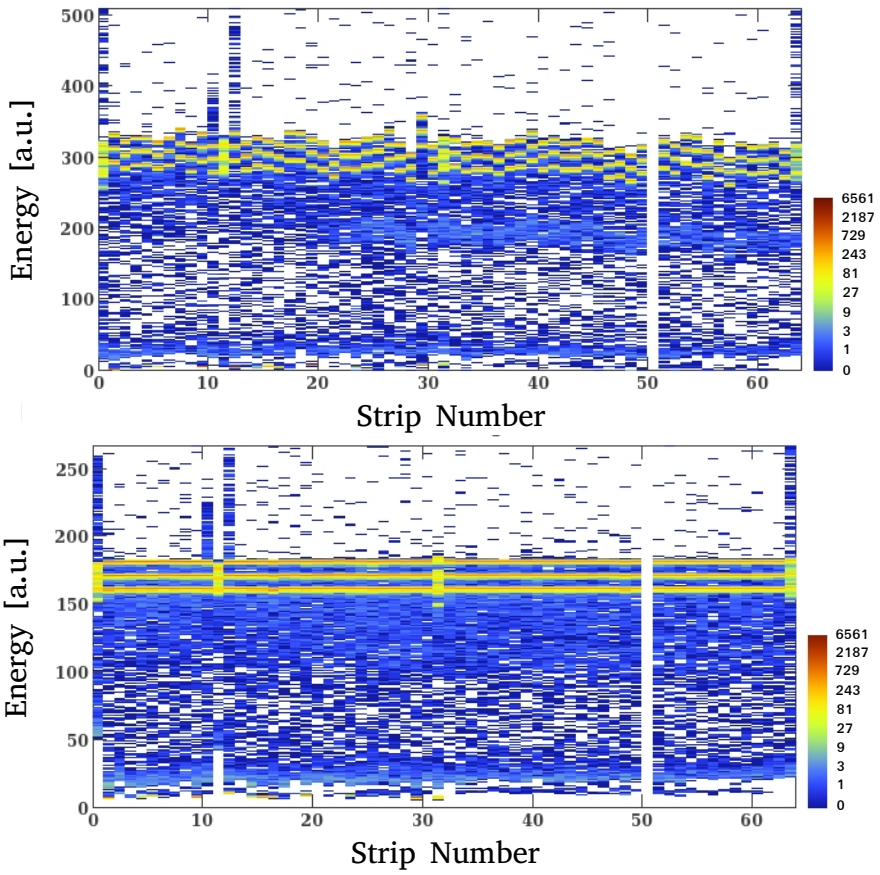

Figure 4.3: 2D energy vs detector strip number for a BB15 style detector prior to the ^{124}Sn(d,p) experiment. The top panel shows a single detector prior to any energy calibrations. The centroid of each alpha peak varies from strip to strip. The bottom panel shows the same detector after applying the energy calibration. All of the alpha peaks line up at the same input voltage to the ADC. Strips 1, 12, and 33 had bad resolution as evidenced by the poor resolution of each individual alpha peak, and strip 51 has no data. These issues are due to the ASICs electronics and detector damage, respectively.

forward ring of BB15 detectors in the SuperORRUBA, the strip angle is given by

$$\theta_{\text{forward}} = 90^\circ - \tan^{-1}\left[\frac{w * (65 - j) + d_2}{r_2}\right], \tag{4.2}$$

where d_2 is the projection along the $z-$axis of the distance from the target to the nearest front side strip on the detector, r_2 is the radius of the array of detectors, and all other parameters are the same as for the backward ring of detectors. The detector strip number, j, is defined so that $j = 1$ near the detector mounting screw holes and continues to $j = 64$. For the BB15 detectors $w = 1.2 \pm 0.1$ mm, and during this experiment $d_1 = 3.7 \pm 1.0$ mm, $d_2 = -2.0 \pm 1.0$ mm, $r_1 = 127.0 \pm 2.0$ mm, and $r_2 = 113.5 \pm 2.0$ mm. The polar angular range of the SuperORRUBA was $\theta_{\text{backward}} = 92 \pm 1^\circ$ to $122 \pm 1^\circ$ and $\theta_{\text{forward}} = 56 \pm 1^\circ$ to $90 \pm 1^\circ$.

4.1.3 Energy Straggling

Once each silicon strip has been calibrated, the detectors will provide the angle and energy of a particle with the assumption it originated at the target position. However, the target has some non-negligible thickness. When a heavy ion from the beam passes through the target it will deposit some energy into the material. It is well-known that for a charged particle moving through matter, the energy deposition is proportional to the square of the charge of the particle [Jac99]. Thus, a tin ion with $Z = 50$ will lose much more energy traversing the target than a

proton with $Z = 1$. A tin ion that undergoes a transfer reaction at the front of the target will have more energy than a tin ion that traverses the extent of the target before inducing a transfer reaction. Using the energy loss code STOPIT [Mil02] we calculate the energy loss of a 630 MeV ion of ^{128}Sn passing through a foil of 240 μg/cm^2 deuterated polyethylene to be 16.5 MeV. Assuming the interaction occurs at the center of the target results in a 3% uncertainty in the energy of the beam.

Correcting for the energy straggling of the protons leaving the target requires knowing the angle of the emitted particle, as the path length through the material depends on this angle. Using the code STOPIT, the energy loss of protons passing through a foil of deuterated polyethylene was calculated for the expected range of proton energies over the angular range of the SuperORRUBA. The energy correction must also be valid for the elastically scattered deuterons. Since the reaction was assumed to be at the center of the target and deuterons and protons experience roughly the same amount of energy straggling, we need only calculate energy loss for the backward ring of the SuperORRUBA. The difference in energy loss for a proton and deuteron passing through a 121μg/cm^2 CD_2 foil is on the order of 1% in the energy range of interest. The energy loss for protons and deuterons will be approximately symmetric about 90° in the laboratory frame for the reasons just listed. The energy loss $E_{loss}(\theta, E_p)$ can be modeled by

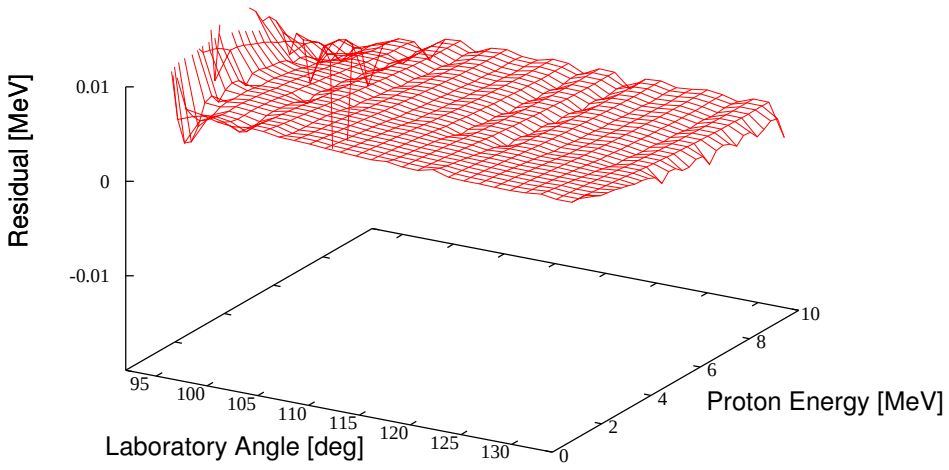

Figure 4.4: Proton energy straggling correction function. Using the code STOPIT, the energy loss of a proton with given initial energy and path length traversing through deuterated polyethylene was calculated. This plot was produced for a proton exiting the center of a 140 μg/cm^2 deuterated polyethylene foil. The z-axis is the difference in energy between the given initial proton energy and the calculated initial energy. The plot shows that the energy loss equation reproduces the actual proton energy to within several keV for most of the range of interest. At θ_{LAB} near 90° the calculation begins to diverge from the actual value by over 10 keV, especially for low energy protons. However, most of this region is shadowed by the target ladder and is not a concern.

$$E_{loss}(\theta, E_p) = \frac{a \cdot \mathrm{e}^{b \cdot E_p} + c}{\theta - 90^\circ} \tag{4.3}$$

where θ is the laboratory angle of the emitted proton, E_p is the residual energy of the proton as detected in a silicon detector, and a, b, and c are constants to be fit. Using the energy loss results from STOPIT, a chi-square fit returned values

of $a = 1.5$ MeV, $b = -0.6$/MeV, and $c = 0.2$ MeV. Figure 4.4 shows the difference in MeV between the initial particle energy and the reconstructed energy as a function of initial energy and laboratory angle.

4.1.4 Solid Angle Calibration

In order to calculate differential cross sections it is necessary to know the solid angle of each detector. The solid angle of each silicon strip can be calculated from geometry; however, it is often preferable to measure the solid angle using an alpha source of known activity. One advantage of this technique is that it does not compound uncertainties from measuring the geometry of the detector arrays. Additionally, any intrinsic flaws that might impact the efficiency of a given silicon strip are folded into the measurement.

For this experiment a ^{244}Cm source was placed at the target position where it could illuminate half of the SuperORRUBA. Data were collected for a precise amount of time and then the source was rotated to illuminate the other half of the array so that data collection could begin again. The source was known to have an activity of 3006 counts per second into 4π steradians as measured on October 28, 2009. The half-life of ^{244}Cm is known to be 181 years, and the date of the solid angle calibration was on March 19, 2012. The present activity, A_2, can be determined by

$$A_2 = A_1 \mathrm{e}^{-t \cdot \ln(2)/T_{1/2}}, \tag{4.4}$$

where A_1 is the activity at an earlier time, $T_{1/2}$ is the half-life of the nucleus, and t is the time duration between the two measurements.

The activity was calculated to be 2740 counts per second at the time of the calibration. Since the source was mounted on a slide it only illuminated 2π steradians, and thus the activity was 1370 counts per second into the direction the source was pointing.

Once the activity of the source is known, the solid angle of a given strip Ω_i is calculated by

$$\Omega_i = \frac{N_i}{A_2 \cdot T} \tag{4.5}$$

where N_i is the number of alpha particles detected in a given silicon strip in a known amount of time T. As a check, the solid angle of each silicon strip was also calculated from geometry. The solid angle of a given strip in the SuperORRUBA can be calculated from the geometrical relation

$$\Omega_i = \frac{A}{r^2} \tag{4.6}$$

where A is the surface area of the silicon strip and r is the distance from the

target to the center of the strip. The active area of a silicon strip on a BB15 style detector is 1.17 mm x 40.3 mm, resulting in an active area of 47.15 mm^2. Thus, only the distance from the target to the strip is needed. A comparison of the two methods showed agreement to within better than 4%. For the final analysis the solid angles determined from the alpha source were used as these measurements also included the efficiency of each strip.

4.2 Particle Identification

Charged particles were detected in the SIDAR and SuperORRUBA in coincidence with heavy ions in the ionization counter. A time-to-amplitude converter (TAC) takes two time signals and outputs a voltage pulse with amplitude proportional to the time difference between the two input signals. Using the silicon trigger as the start signal for the TAC, and the first anode in the ionization counter (delayed by $\sim 4\mu s$) as the stop signal for the TAC, it was possible to identify a peak corresponding to target induced events. The TAC spectrum shown in Figure 4.5 is from the ^{128}Sn(d,p) reaction. Gating on the events within this peak reduces the number of random events in the particle spectra, greatly enhancing the (d,p) reaction protons of interest.

In order to further clarify the silicon spectra, it is useful to gate on heavy particles detected in the IC. The detector was setup with an energy loss (dE) and residual energy (E) region, where the incident radiation passed through the dE

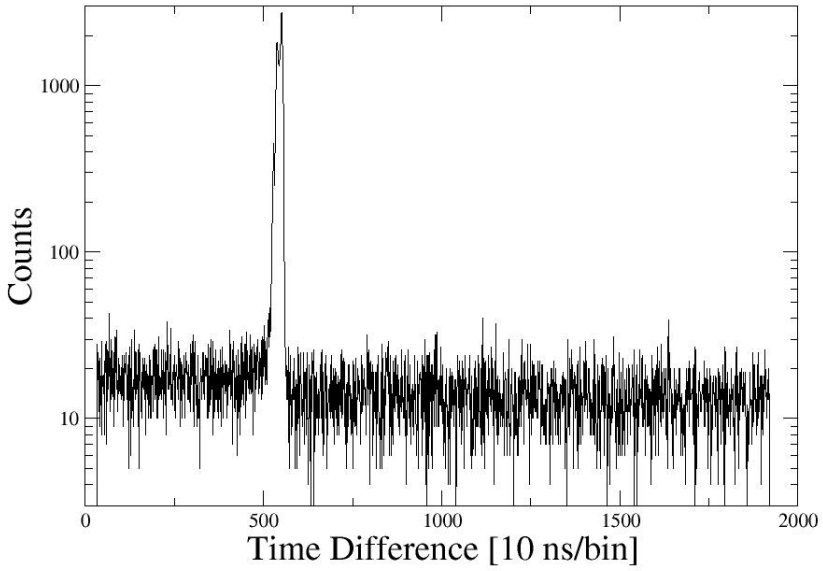

Figure 4.5: TAC spectrum for the ^{124}Sn(d,p) reaction generated by a start signal from the silicon detectors and a stop signal from the ionization chamber. Both the transfer and elastic channel are contained in the peak.

depositing some energy before stopping in the E and depositing all of its residual energy. By plotting the energy deposited in the dE against the sum of the energy deposited in the dE and E, it is possible to identify different species as based on their masses and charges as described in Section 3.2.2 of this dissertation. It is also worth noting that requiring a coincidence between both the dE and the E helps to reject random noise present in either signal.

It is possible for incident radiation to strike the grid wires of the IC itself. These events are perfectly fine and should be included in the data analysis. Such events show up in Figure 4.6 as a series of centroids on both the left and top of the plot. The strong centroid in the upper right hand corner of the plot is from

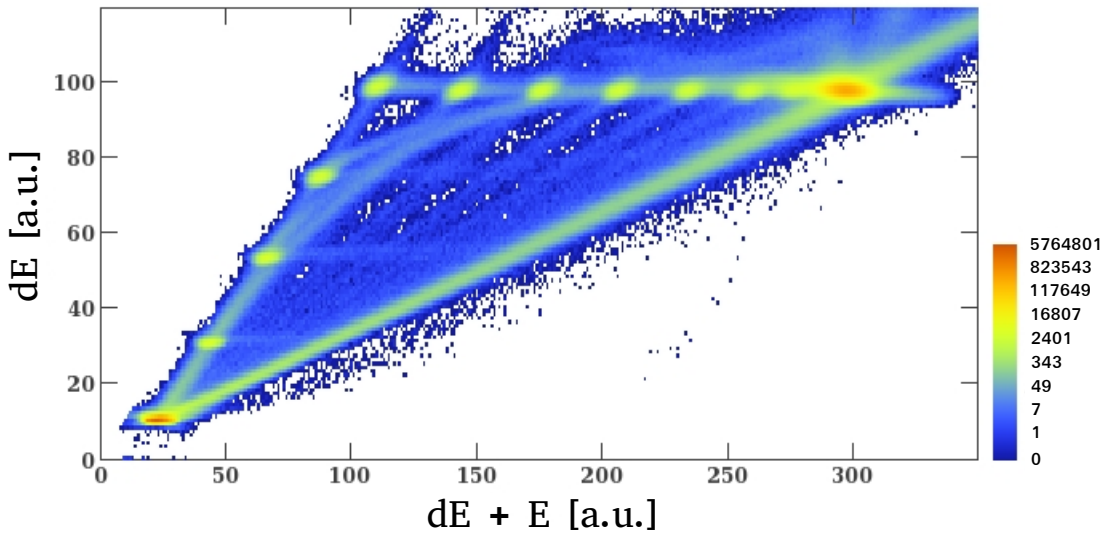

Figure 4.6: A dE vs. $dE + E$ spectrum from the ionization counter during the ^{124}Sn(d, p) experiment. There are centroids along the left and top side of the data corresponding to the beam particles striking grid wires in one of the anodes. The intense centroid in the upper right corner is the a combination of the unreacted ^{124}Sn ions and the ^{125}Sn ions from a transfer reaction.

both unreacted beam and heavy residues from the reaction. This figure is taken from the ^{124}Sn(d, p) experiment, so the focus in the upper right hand corner of Figure 4.6 are both ^{124}Sn and ^{125}Sn. The mass difference between the two nuclei is only 0.8%, so the IC is not able to resolve the two species. The focus in the bottom left corner of the plot is noise from the electronics and should not be included in the analysis of the silicon detectors. By gating on the counts in the middle of the triangle it was determined that there were good (d, p) events correlated with many of these counts. The streaks originating from the grid wire foci are believed to be due to real ions striking grid wires in coincidence with random signals. Thus, in order to improve the quality of the silicon spectra, a gate was placed around all events in the IC except for the foci near the origin.

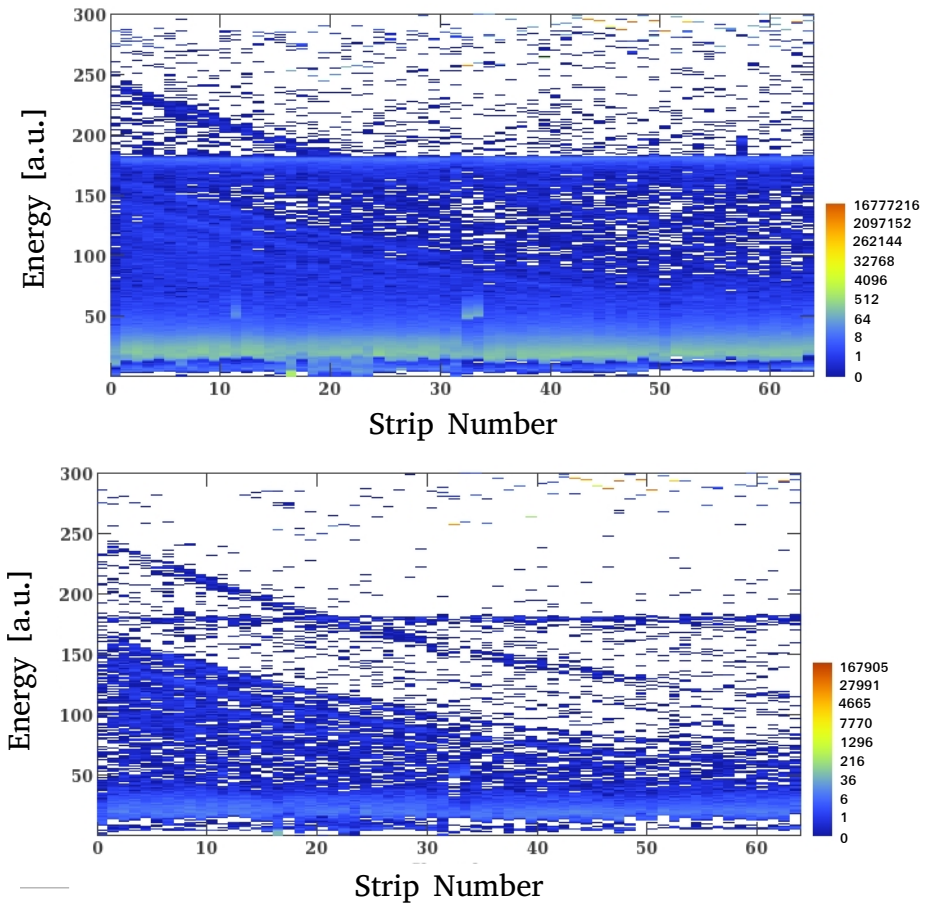

Figure 4.7: A 2D plot of energy vs strip number for all BB15 style detectors backwards of $\theta_{LAB} = 90°$ during the ^{124}Sn(d,p) experiment. The top panel shows the raw data without any gating. The bottom panel shows the same data after gating on the TAC peak and anti-gating on the noise in the IC.

Gating on the TAC peak and good events in the IC dramatically improved the quality of the silicon detector data. Figure 4.7 shows a single BB15 detector from the ^{124}Sn(d,p) experiment without any gates applied, and then with these gates described above.

4.3 Beam Normalization

In order to normalize the differential cross sections, it is imperative to understand the integrated number of beam particles on target and the number of particles in that target. Ideally, a beam counter at 0° in the lab frame would count all incoming beam particles. The IC in this experiment provides a good tool for this approach. However, there are several issues that arise using this method. Any pileup that occurs in the ADC must be accounted for. Pileup is a situation where nearly simultaneous events are detected, causing an artificially high energy to be read into the ADC. It is possible to interpret the pileup events and reconstruct the total number of particles into the IC, but it may be difficult to quantify the uncertainty.

Another approach is to compare the differential cross section for elastically scattered deuterons from the target to the well-known Rutherford scattering cross section [Jon11, Ahn13, Sch12]. By normalizing the elastic cross section to the Rutherford cross section it is possible to obtain the product of the integrated number of beam particles and the total number of target particles. Jones et al. showed that calculated cross section is dominated by the Coulomb potential, thus the choice of optical model potential is not critical [Jon11]. For this study Lohr-Haeberli global potentials [Loh74] were used for the deuteron optical potential. The normalization factor N is given by,

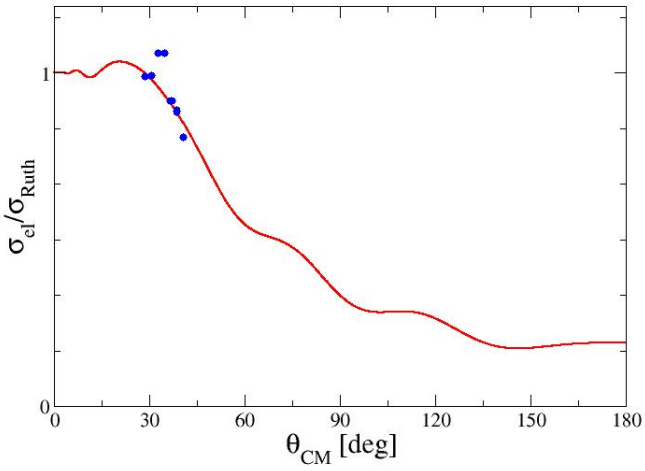

Figure 4.8: Ratio of measured elastically scattered deuterons to the Rutherford differential cross section. The deuteron data are scaled to the elastic scattering calculation (red curve). Blue dots shows the data from the BB15 style detectors. Statistical uncertainties are the size of the points for the data. Furthermore, a similar discrepancy has been noted in previous experiments [Jon11, Ahn13].

$$N \cdot \left(\frac{d\sigma}{d\Omega}\right)_{\text{el}} = \left(\frac{d\sigma}{d\Omega}\right)_{\text{Ruth}} \tag{4.7}$$

where $\left(\frac{d\sigma}{d\Omega}\right)_{\text{el}}$ is the unnormalized deuteron elastic cross section and $\left(\frac{d\sigma}{d\Omega}\right)_{\text{Ruth}}$ is the calculated Rutherford scattering cross section. To normalize the (d,p) reaction cross section one must multiply the unnormalized cross section by the normalization factor N.

There are two distinct advantages to this approach: it only requires one measurement and it takes into account the actual beam on target interaction. The rate of particles being measured in the silicon detectors is much lower than the rate of particles into the IC. Counting in the silicon detectors is more reliable due

to these decreased rates. As for the target, it is possible that it could degrade over time. It is also possible that the target density is not uniform. In either of these cases it would prove difficult to precisely determine the target thickness at the interaction point, especially if the beam spot drifted during the experiment. Measuring the elastically scattered deuterons automatically accounts for all of these complications.

The elastic yield is measured in a region where the scattering is dominated by Coulomb effects and is independent of the interior of the nuclear wavefunction, and thus the choice of optical model parameters. Previous studies have shown that for $\theta_{\mathrm{CM}} < 30^{\circ}$ both the energy and angular resolution quickly degrade because the lowest energy particles are scattered at the most forward center-of-mass angles [Jon11, Ahn13, Sch12]. The same effect is observed in the present study, as shown in Figure 4.8 for ^{124}Sn(d,d). The data were fit to a FRESCO [Tho88] calculation over the range $30^{\circ} < \theta_{CM} < 45^{\circ}$. For the calculation, the potential included both a Coulomb and nuclear component, where the optical model parameters for the deuteron wavefunction were taken from Lohr-Haberli global nuclear potentials [Loh74]. Previous studies [Jon11, Ahn13, Sch12] also indicate a bump in the data near $\theta_{CM} = 35^{\circ}$, so this feature is considered to be normal and the data points were ignored in the fit. The uncertainty in the fit was taken to be 10% from a chi-square minimization.

4.4 Single-Neutron States

The primary focus of these experiments is to study single-neutron states above the N=82 shell gap. The first step is to identify states from the Q-value spectrum for each reaction. Extracting the centroid of the Q-value for each state enables a calculation of the excitation energy of this state in the final nucleus. Once a state has been identified it may be possible to assign a value to the orbital angular momentum, ℓ, transferred in the reaction. The data for each state are divided into angular bins and the differential cross section is plotted as a function of center of mass angle. Comparing reaction theory calculations to the differential cross section may allow us to determine ℓ. Although the spin is not uniquely defined by ℓ, it can often be inferred. Finally, a spectroscopic factor is determined by normalizing the theoretical differential cross section to the measured results. The extracted spectroscopic factor will depend strongly on the inputs into the theoretical calculation.

4.4.1 Reaction Q-values

A separate Q-value spectrum was produced for each radioactive ion beam experiment. The reaction Q-value is the mass difference between the initial reaction channel and the final channel [Kra87]. For a binary reaction with initial masses m_{beam} and m_{target} and final masses $m_{ejectile}$ and m_{recoil}, the relativistic Q-value is given by

$$Q = m_{beam} + m_{target}m_{ejectile} - [m_{beam}^2 + m_{target}^2 + m_{ejectile}^2 + 2m_{target}E_{beam} - 2E_{ejectile}\left(E_{ejectile} + m_{target}\right) + 2P_{beam}P_{ejectile}\cos\psi]^{1/2} \quad (4.8)$$

where E_{beam} is the total beam energy, $E_{ejectile}$ is the total ejectile energy, P_{beam} is the relativistic momentum of the beam, $P_{ejectile}$ is the relativistic momentum of the ejectile, and ψ is the scattering angle of the ejectile relative to the beam axis [Mar68].

The beam energy is taken to be the residual energy of the incoming tin ions halfway through the target. The masses and relativistic momenta of the beam, target, and ejectile are known. By measuring the energy and angle of each ejectile it is possible to calculate the relativistic Q-value on an event-by-event basis.

^{124}Sn(d,p)

In the ^{124}Sn(d,p) Q-value spectrum shown in Figure 4.9, there are three prominent states observed near $Q = 0$ MeV. There appears to be a doublet of states near $Q = 3.25$ MeV, and potentially several states below $Q = -1$ MeV. A Gaussian was fit to the three prominent peaks to extract the centroid of the peak. The uncertainty in the centroid was determined from the full width at half maximum (FWHM), since FWHM$= 2.354 \times \sigma$. Once the Q-value of a state is known, the

excitation energy of the state can be determined from the kinematics calculator CATKIN [Cat04]. For the moment the peaks will be labeled A, B, and C in order of decreasing Q-value. The extracted values are $Q_A = 0.74 \pm 0.04$ MeV, $Q_B = 0.13 \pm 0.04$ MeV, and $Q_C = -0.49 \pm 0.05$ MeV. These values correspond to $E_A = 2.77 \pm 0.04$ MeV, $E_B = 3.39 \pm 0.04$ MeV, and $E_C = 4.00 \pm 0.05$ MeV. The quality of the lower Q-value peaks appears to deteriorate as the width increases for these states. The broadening of the peaks is due to the observed fragmentation of the single-neutron states [Tom11] The fragmentation is further illustrated in Figure 4.10, a plot of the relative strength (normalized to unity) of each state as a function of excitation energy. The black curves are Gaussians with centroids and widths derived from the present study. The amplitude is normalized to the spectroscopic factors accepted in Table 5.1. The red lines represent states observed by Tomandl et al. in the ^{124}Sn(d,p) reaction in normal kinematics [Tom11] with orbital angular momentum $\ell = 3$, and the blue lines represent states with $\ell = 1$. The amplitude of each line represents the spectroscopic factor of the state. The width of the lines represents the energy resolution from the study.

The doublet near $Q = 3.25$ MeV has been well studied in previous measurements [Jon04, Tom11, Str77]. It is the combination of a $3/2^+$ state at $E_x = 0.029$ MeV, and a $1/2^+$ state at $E_x = 0.219$ MeV. In the present measurement the broad peak was fit with two Gaussian peaks near the centroid. The extracted centroids of the peaks were found to be $Q_{3/2} = 3.17$ MeV and $Q_{1/2} = 3.37$ MeV, thus indicating the states are separated by approximately

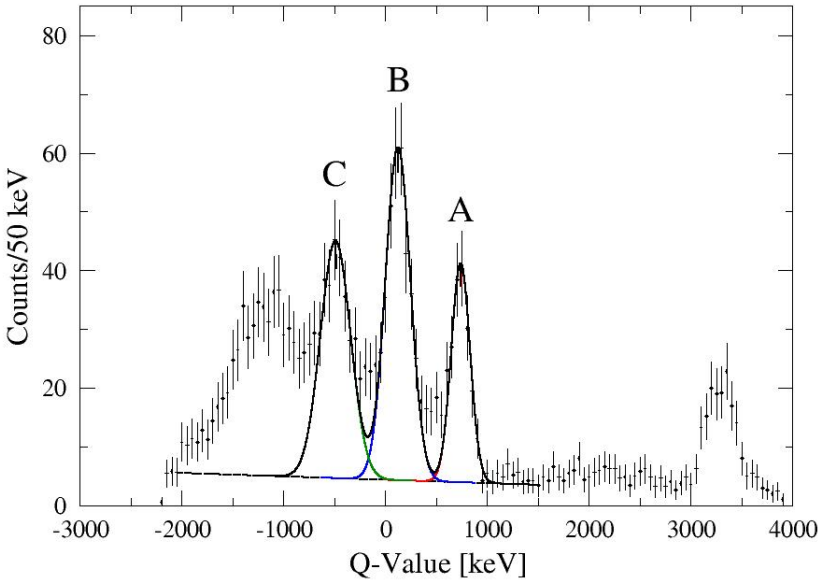

Figure 4.9: Q-value spectrum of ^{124}Sn(d,p) in inverse kinematics, summed over all angles. The uncertainties on the data are purely statistical. Dashed curves represent the fits to each state and the background. A solid black line represents the sum of all of the fits and the background. The centroids extracted from the individual fits are $Q_A = 0.74 \pm 0.04$ MeV, $Q_B = 0.13 \pm 0.04$ MeV, and $Q_C = -0.49 \pm 0.05$ MeV. The uncertainties on centroids are calculated from the error in the fit.

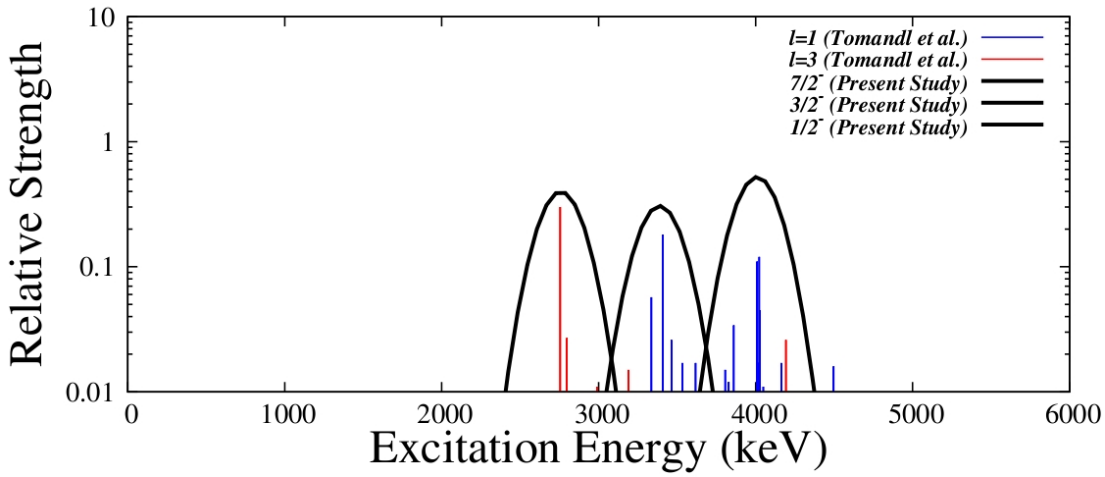

Figure 4.10: Relative strength of states observed in ^{124}Sn(d,p) as a function of excitation energy. The black curves are Gaussians with centroids and widths derived from the present study. The amplitude is normalized to the spectroscopic factors accepted in Table 5.1. The red lines represent states observed by Tomandl et al. in the ^{124}Sn(d,p) reaction in normal kinematics [Tom11] with orbital angular momentum $\ell = 3$, and the blue lines represent states with $\ell = 1$. The width of the lines represents the energy resolution of each state, and the amplitude is normalized to the spectroscopic factor deduced by Tomandl.

200 keV, consistent with the adopted excitation energies [Tom11]. The energy resolution was not sufficient to resolve the states individually, but present work indicates that the observed doublet is indeed the previously studied states. We adopt the values $E_x = 0.029$ MeV and $E_x = 0.219$ MeV for the excitation energies [ENS11].

The broad peak below $Q = -1.00$ MeV did not possess enough structure to clearly identify individual states. Previous studies [Tom11] suggest that this broad peak is composed of many small fragments of the $5/2^-$ single-particle strength. The energy resolution in the present study is not sufficient to resolve these individual states, and it is not possible to reliably extract spectroscopic information.

^{126}**Sn**(d,p)

In the ^{126}Sn(d,p) Q-value spectrum shown in Figure 4.11, there are three prominent states observed near $Q = 0$ MeV. There appears to be a doublet of states just above $Q = 3.00$ MeV, and potentially several weakly populated states below $Q = -1$ MeV. A Gaussian was fit to the three prominent peaks to extract the centroids, and the error in the fit provided a measure of the uncertainty in the centroid. Once the Q-value of a state is known, the excitation energy of the state can be determined from the kinematics calculator CATKIN. For the moment the peaks will be labeled A, B, and C in order of decreasing Q-value. The extracted values are $Q_A = 0.62 \pm 0.04$ MeV, $Q_B = 0.01 \pm 0.05$ MeV, and $Q_C = -0.56 \pm 0.05$ MeV. These values correspond to $E_A = 2.71 \pm 0.04$ MeV, $E_B = 3.33 \pm 0.05$ MeV, and $E_C = 3.88 \pm 0.05$ MeV.

Due to the poor statistics of the high Q-value region, it was not possible to extract a clear centroid for any proposed states. These states are likely to be the $3/2^+$ state at 0.005 MeV and the $1/2^+$ state at 0.258 MeV as observed in the decay of the $1/2^-$ isomer in ^{127}In [Gau04].

^{128}**Sn**(d,p)

In the ^{128}Sn(d,p) Q-value spectrum shown in Figure 4.12, there are three prominent states observed near $Q = 0$ MeV. There appears to be a doublet of states

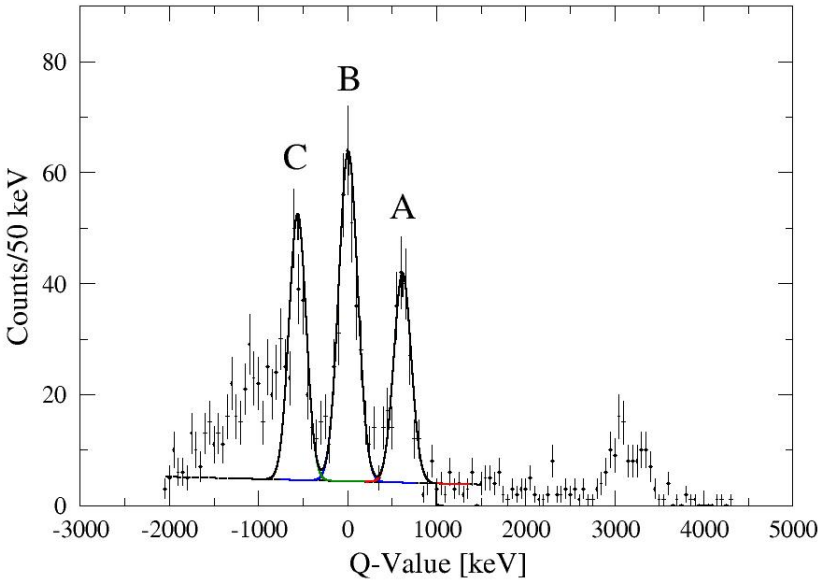

Figure 4.11: Q-value spectrum of $^{126}\mathrm{Sn}(d,p)$ in inverse kinematics, summed over all angles. The uncertainties on the data are purely statistical. Dashed curves represent the fits to each state and the background. A solid black line represents the sum of all of the fits and the background. The centroids extracted from the individual fits are $Q_A = 0.62 \pm 0.04$ MeV, $Q_B = 0.01 \pm 0.05$ MeV, and $Q_C = -0.56 \pm 0.05$ MeV. The uncertainties on centroids are calculated from the error in the fit.

near $Q = 3.25$ MeV, and potentially several states below $Q = -1$ MeV. A Gaussian was fit to the three prominent peaks to extract the centroids, and the error in the fit provided a measure of the uncertainty in the centroids. Once the Q-value of a state is known, the excitation energy of the state can be determined from the kinematics calculator CATKIN. For the moment the peaks will be labeled A, B, and C in order of decreasing Q-value. The extracted values are $Q_A = 0.40 \pm 0.05$ MeV, $Q_B = -0.21 \pm 0.05$ MeV, and $Q_C = -0.81 \pm 0.06$ MeV. These values correspond to $E_A = 2.77 \pm 0.05$ MeV, $E_B = 3.39 \pm 0.05$ MeV, and $E_C = 4.00 \pm 0.06$ MeV.

Although the statistics of the three prominent peaks were better in the ^{128}Sn(d,p) experiment than those in the ^{126}Sn(d,p) experiment, the population of the high Q-value states was actually worse. It was not possible to extract a clear centroid for any proposed states. These states are likely to be the $3/2^+$ ground state and the $1/2^+$ state at 0.315 MeV observed in the decay of the $9/2^+$ ground state of ^{129}In [Gau04].

It is often desirable to normalize the Q-value spectrum to previously measured states with energy centroids known to high precision [Ahn13, Tho07]. However, the states of interest in ^{127}Sn and ^{129}Sn have not been previously observed. The prominent states observed in ^{125}Sn agree very well with previous high precision measurements [Tom11, Str77]. Therefore, we feel that the extracted energies are

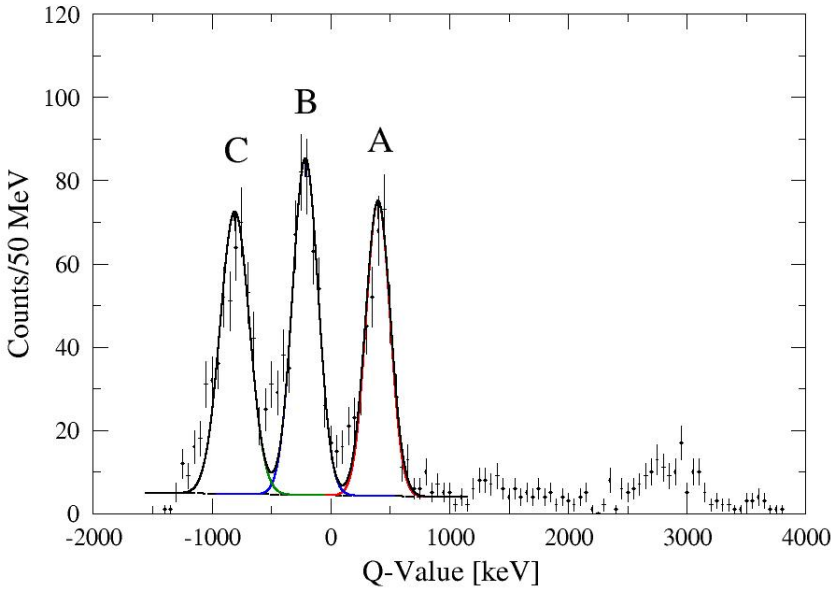

Figure 4.12: Q-value spectrum of $^{128}\mathrm{Sn}(d,p)$ in inverse kinematics, summed over all angles. The uncertainties on the data are purely statistical. Dashed curves represent the fits to each state and the background. A solid black line represents the sum of all of the fits and the background. The centroids extracted from the individual fits are $Q_A = 0.40 \pm 0.05$ MeV, $Q_B = -0.21 \pm 0.05$ MeV, and $Q_C = -0.81 \pm 0.06$ MeV. The uncertainties on centroids are calculated from the error in the fit.

reliable for all Q-value spectra in the study since the ^{124}Sn beam measurements were part of the same campaign as the ^{126}Sn and ^{128}Sn studies.

4.4.2 Reaction Angular Distributions

Absolute differential cross sections were determined for each of the three prominent peaks populated in all three reactions. The cross section was first calculated in the laboratory system as

$$\frac{d\sigma(\theta_i)}{d\Omega} = N \cdot \frac{N_i}{d\Omega_i}, \tag{4.9}$$

where θ_i is the average angle in the laboratory frame of the ith angular bin, N is the normalization factor determined from elastically scattered deuterons, N_i is the number of recoil-coincident protons observed in the ith angular bin, and $d\Omega_i$ is the solid angle subtended by the silicon detectors in the ith angular bin.

The differential cross section must then be converted to center-of-mass coordinates by way of a Jacobian transformation between the two reference frames for the ith angular bin. The cross section in the center-of-mass frame is given by

$$\left(\frac{d\sigma}{d\Omega}\right)_{CM} = \gamma \cdot \left(\frac{d\sigma}{d\Omega}\right)_{Lab} \tag{4.10}$$

where γ is the Jacobian transformation defined as

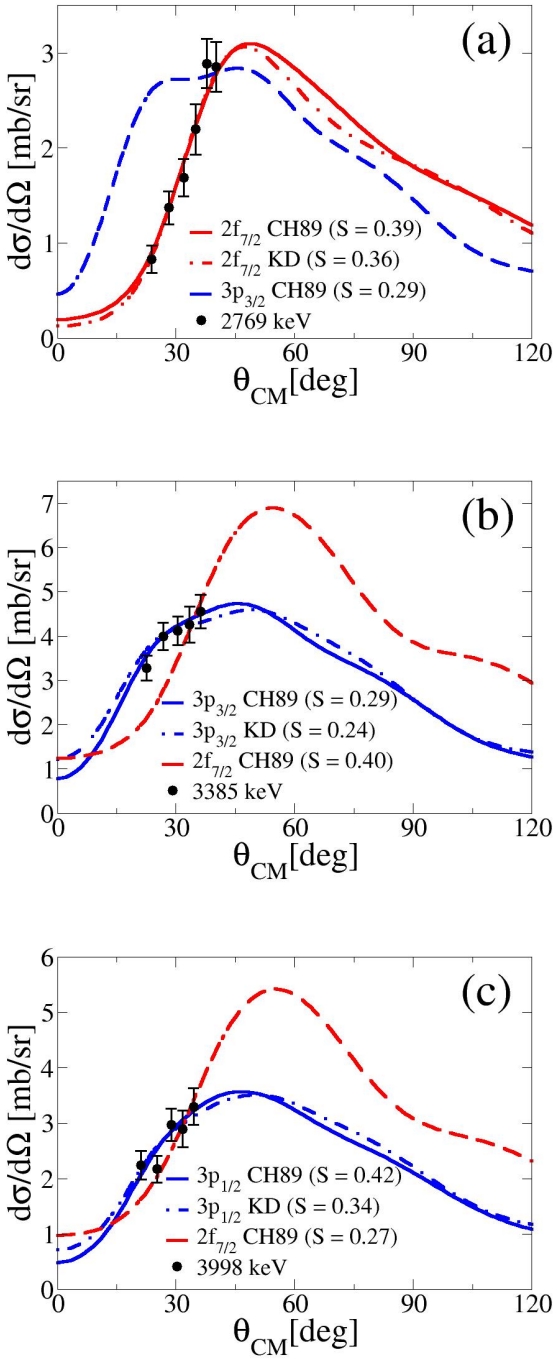

Figure 4.13: Absolute differential cross sections from the ^{124}Sn(d,p) reaction with purely statistical uncertainties. Panel (a) is for state A, panel (b) is for state B, and panel (c) is for state C. The data are compared to FR-ADWA calculations for a momentum transfer of $\ell = 3$ transfer (red curves) and $\ell = 1$ (blue curves). Adopted orbital angular momentum transfer calculations were made using the Chapel-Hill 89 parameterization (solid curve) and the Koning-Delaroche parameterization (dot-dashed curves). The other orbital angular momentum transfer was only calculated with the Chapel-Hill 89 parameterization (dashed line).

$$\gamma = \frac{\left|1 - \rho \cos\left(\theta_i^{CM}\right)\right|}{\left(1 + \rho^2 - 2\rho \cos\left(\theta_i^{CM}\right)\right)^{3/2}} \tag{4.11}$$

and

$$\rho = \frac{m_{beam} \cdot m_{ejectile}}{m_{recoil} \cdot m_{target}} \left(\frac{E_{ejectile}^{CM}}{E_{ejectile}^{CM} + Q} \right) \tag{4.12}$$

where $E_{ejectile}^{CM}$ is the center-of-mass kinetic energy of the ejectile, Q is the reaction Q-value, m_{beam}, m_{recoil}, $m_{ejectile}$, and m_{target} are the rest mass of the beam, heavy residue, ejectile, and target respectively and θ_i is the center-of-mass angle corresponding to the ith angular bin [Lee10].

The experimental differential cross sections for the three prominent states populated in ^{124}Sn$(d,p)^{125}$Sn, ^{126}Sn$(d,p)^{127}$Sn, and ^{128}Sn$(d,p)^{129}$Sn were analyzed with both DWBA and ADWA reaction formalisms [Joh70, Joh72, Joh74] as shown in Figures 4.13, 4.14, and 4.15. For the DWBA calculation the optical potential for the deuteron in the incident channel was the same as that used in the elastic scattering analysis [Loh74]. The proton optical potential for the outgoing channel was taken from the Chapel-Hill 89 parameterization [Var91]. Two ADWA calculations were performed using different optical model parameterizations. The Reid interaction [Rei68] was used to obtain the deuteron wavefunction and in the transfer operator for both calculations. The deuteron adiabatic potential was constructed using the Johnson and Tandy optical parametrization method [Joh74]

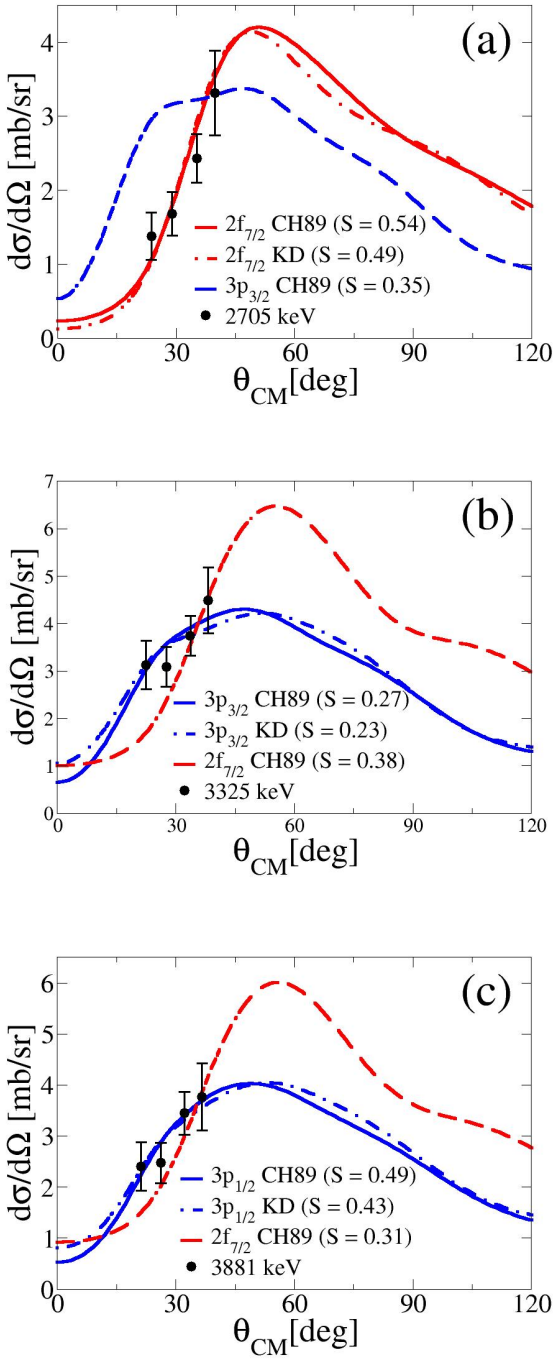

Figure 4.14: Absolute differential cross sections from the ^{126}Sn(d,p) reaction with purely statistical uncertainties. Panel (a) is for state A, panel (b) is for state B, and panel (c) is for state C. The data are compared to FR-ADWA calculations for a momentum transfer of $\ell = 3$ transfer (red curves) and $\ell = 1$ (blue curves). Adopted orbital angular momentum transfer calculations were made using the Chapel-Hill 89 parameterization (solid curve) and the Koning-Delaroche parameterization (dot-dashed curves). The other orbital angular momentum transfer was only calculated with the Chapel-Hill 89 parameterization (dashed line).

using Chapel-Hill 89 [Var91] nucleonic potentials for the neutron and the proton. The second ADWA calculation was performed in the exact same manner but with Koning-Delaroche [Kon03] nucleonic potentials for the neutron and proton. All of the reaction calculations included finite range effects using the code FRESCO [Tho88]. Standard radius and diffuseness parameters of $r = 1.25$ fm and $a = 0.65$ fm were used for the bound state of the neutron. Tables 4.2, 4.3, and 4.4 summarize the potentials used for both the DWBA and ADWA calculations.

The theoretical calculations strongly suggest that state A in ^{125}Sn, ^{127}Sn, and ^{129}Sn are transfers of $\ell = 3$. State B seems to be best described by a transfer of $\ell = 1$ in ^{125}Sn and ^{127}Sn, as well as in ^{129}Sn where the most forward angle data are best described by an $\ell = 1$ transfer. The transfer for state C in ^{125}Sn is not clear. The transfer for state C in ^{127}Sn and ^{129}Sn agrees well with $\ell = 1$, with the forward angle data for the C state in ^{125}Sn also suggesting an $\ell = 1$ transfer. This pattern of one $\ell = 3$ transfer and two $\ell = 1$ transfers is analogous to that observed in previous studies of ^{133}Sn [Jon11] and ^{131}Sn [Koz12], and is consistent with the high resolution studies of ^{125}Sn [Tom11].

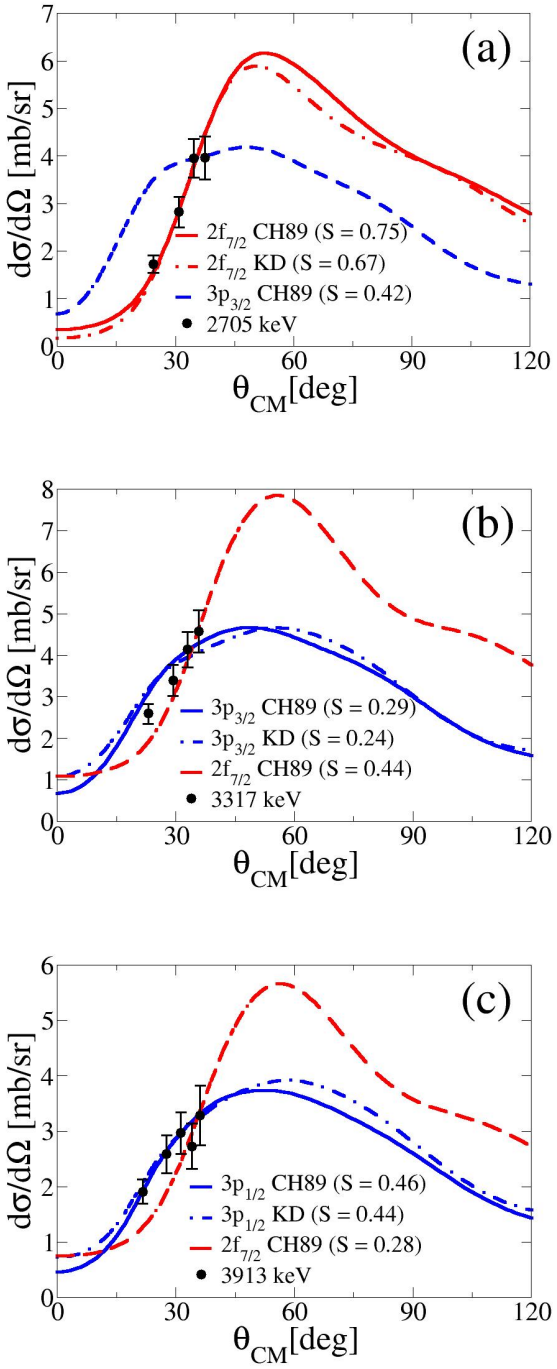

Figure 4.15: Absolute differential cross sections from the ^{128}Sn(d,p) reaction with purely statistical uncertainties. Panel (a) is for state A, panel (b) is for state B, and panel (c) is for state C. The data are compared to FR-ADWA calculations for a momentum transfer of $\ell = 3$ transfer (red curves) and $\ell = 1$ (blue curves). Adopted orbital angular momentum transfer calculations were made using the Chapel-Hill 89 parameterization (solid curve) and the Koning-Delaroche parameterization (dot-dashed curves). The other orbital angular momentum transfer was only calculated with the Chapel-Hill 89 parameterization (dashed line).

Table 4.2: Optical model potential parameters for DWBA and ADWA calculation in ^{124}Sn(d,p) reaction. The definition of the parameters are explained in Section 2.2.1. The value of $r_{W\ vol}$ and $a_{W\ vol}$ are the same as the one of $r_{V\ vol}$ and $a_{V\ vol}$. The V_{vol} value for the neutron $(*)$ is adjusted to reproduce the binding energy of the neutron in the ^{125}Sn nucleus.

Theory	Channel	V_{vol} (MeV)	$r_{V\ vol}$ (fm)	$a_{V\ vol}$ (fm)	W_{vol} (MeV)	W_{surf} (MeV)	r_{surf} (fm)	a_{surf} (fm)	V_{so} (MeV)	r_{so} (fm)	a_{so} (fm)	r_{coul} (fm)
DWBA	d	113.19	1.05	0.86	0.00	8.77	1.43	0.82	7.00	0.75	0.50	1.30
DWBA	p	56.40	1.21	0.69	0.67	10.08	1.25	0.69	5.90	1.10	0.63	1.26
DWBA	n	$*$	1.25	0.65	0.00	0.00	0.00	0.00	6.00	1.25	0.65	1.30
ADWA - CH	$d(p)$	58.03	1.21	0.69	0.48	10.38	1.25	0.69	5.90	1.10	0.63	1.26
ADWA - CH	$d(n)$	48.86	1.21	0.69	1.04	4.55	1.25	0.69	5.90	1.10	0.63	1.26
ADWA - CH	p	56.40	1.21	0.69	0.67	10.08	1.25	0.69	5.90	1.10	0.63	1.26
ADWA - CH	n	$*$	1.25	0.65	0.00	0.00	0.00	0.00	6.00	1.25	0.65	1.30
ADWA - KD	$d(p)$	61.23	1.22	0.66	0.31	7.55	1.26	0.58	6.01	1.06	0.59	1.23
ADWA - KD	$d(n)$	52.33	1.22	0.66	0.40	5.10	1.26	0.58	6.01	1.06	0.59	1.23
ADWA - KD	p	58.74	1.22	0.66	0.66	9.16	1.26	0.58	5.87	1.06	0.59	1.23
ADWA - KD	n	$*$	1.25	0.65	0.00	0.00	0.00	0.00	6.00	1.25	0.65	1.30

Table 4.3: Optical model potential parameters for DWBA and ADWA calculation in ^{126}Sn(d,p) reaction. The definition of the parameters are explained in Section 2.2.1. The value of $r_{W\ vol}$ and $a_{W\ vol}$ are the same as the one of $r_{V\ vol}$ and $a_{V\ vol}$. The V_{vol} value for the neutron $(*)$ is adjusted to reproduce the binding energy of the neutron in the ^{127}Sn nucleus.

Theory	Channel	V_{vol} (MeV)	$r_{V\ vol}$ (fm)	$a_{V\ vol}$ (fm)	W_{vol} (MeV)	W_{surf} (MeV)	r_{surf} (fm)	a_{surf} (fm)	V_{so} (MeV)	r_{so} (fm)	a_{so} (fm)	r_{coul} (fm)
DWBA	d	113.07	1.05	0.86	0.00	8.67	1.43	0.83	7.00	0.75	0.50	1.30
DWBA	p	56.63	1.21	0.69	0.66	10.26	1.25	0.69	5.90	1.10	0.63	1.26
DWBA	n	$*$	1.25	0.65	0.00	0.00	0.00	0.00	6.00	1.25	0.65	1.30
ADWA - CH	$d(p)$	58.21	1.21	0.69	0.48	10.56	1.25	0.69	5.90	1.10	0.63	1.26
ADWA - CH	$d(n)$	48.72	1.21	0.69	1.03	4.39	1.25	0.69	5.90	1.10	0.63	1.26
ADWA - CH	p	56.63	1.21	0.69	0.66	10.26	1.25	0.69	5.90	1.10	0.63	1.26
ADWA - CH	n	$*$	1.25	0.65	0.00	0.00	0.00	0.00	6.00	1.25	0.65	1.30
ADWA - KD	$d(p)$	58.03	1.21	0.69	0.48	10.38	1.25	0.69	5.87	1.06	0.59	1.23
ADWA - KD	$d(n)$	48.86	1.21	0.66	0.66	9.16	1.26	0.58	5.87	1.06	0.59	1.23
ADWA - KD	p	59.06	1.22	0.66	0.64	9.22	1.26	0.59	5.89	1.06	0.59	1.23
ADWA - KD	n	$*$	1.25	0.65	0.00	0.00	0.00	0.00	6.00	1.25	0.65	1.30

Table 4.4: Optical model potential parameters for DWBA and ADWA calculation in ^{128}Sn(d,p) reaction. The definition of the parameters are explained in Section 2.2.1. The value of $r_{W\ vol}$ and $a_{W\ vol}$ are the same as the one of $r_{V\ vol}$ and $a_{V\ vol}$. The V_{vol} value for the neutron $(*)$ is adjusted to reproduce the binding energy of the neutron in the ^{129}Sn nucleus.

Theory	Channel	V_{vol} (MeV)	$r_{V\ vol}$ (fm)	$a_{V\ vol}$ (fm)	W_{vol} (MeV)	W_{surf} (MeV)	r_{surf} (fm)	a_{surf} (fm)	V_{so} (MeV)	r_{so} (fm)	a_{so} (fm)	r_{coul} (fm)
DWBA	d	112.96	1.05	0.86	0.00	8.58	1.43	0.83	7.00	0.75	0.50	1.30
DWBA	p	56.88	1.21	0.69	0.65	10.45	1.25	0.69	5.90	1.10	0.63	1.26
DWBA	n	$*$	1.25	0.65	0.00	0.00	0.00	0.00	6.00	1.25	0.65	1.30
ADWA - CH	$d(p)$	58.37	1.21	0.69	0.48	10.73	1.25	0.69	5.90	1.10	0.63	1.26
ADWA - CH	$d(n)$	48.58	1.21	0.69	1.03	4.24	1.25	0.69	5.90	1.10	0.63	1.26
ADWA - CH	p	56.88	1.21	0.69	0.65	10.45	1.25	0.69	5.90	1.10	0.63	1.26
ADWA - CH	n	$*$	1.25	0.65	0.00	0.00	0.00	0.00	6.00	1.25	0.65	1.30
ADWA - KD	$d(p)$	58.03	1.21	0.69	0.48	10.38	1.25	0.69	5.87	1.06	0.59	1.23
ADWA - KD	$d(n)$	48.86	1.21	0.66	0.66	9.16	1.26	0.58	5.87	1.06	0.59	1.23
ADWA - KD	p	59.42	1.22	0.66	0.61	9.26	1.26	0.59	5.90	1.06	0.59	1.23
ADWA - KD	n	$*$	1.25	0.65	0.00	0.00	0.00	0.00	6.00	1.25	0.65	1.30

Chapter 5

Interpretations

The results presented in this chapter combine the theoretical framework discussed in Chapter 2 with the experimental quantities from Chapter 4. In addition to analyzing data from the present study of the ^{124}Sn(d,p), ^{126}Sn(d,p), and ^{128}Sn(d,p) reactions, this chapter provides a re-analysis of previous studies of the ^{130}Sn(d,p) and ^{132}Sn(d,p) reactions [Koz12, Jon11, Jon10]. The results show systematic trends that can have broad impacts on both nuclear structure and nuclear astrophysics.

5.1 Spectroscopic Factors

As discussed in Chapter 2, experimental spectroscopic factors rely heavily on the reaction theory formalism, choice of optical model parameterization, and bound state geometry of the neutron. Comparing spectroscopic factors from different measurements is most meaningful when these theoretical inputs are the same for all of the reactions. A major focus of this project was creating a systematic study of the same single-neutron states in odd-mass tin isotopes from ^{133}Sn

to ^{125}Sn. Thus, this dissertation includes a re-analysis of the spectroscopic factors from previous studies of both the ^{130}Sn(d,p) [Koz12] and ^{132}Sn(d,p) reactions [Jon10, Jon11] using the same reaction theory formalism, choice of optical model parameterization, and bound state geometry of the neutron as used for the analysis of the ^{124}Sn(d,p), ^{126}Sn(d,p), and ^{128}Sn(d,p) measurements described in Chapter 4.

Table 5.1: Spectroscopic factors of the three single-neutron states populated by the (d,p) reaction on neutron-rich tin isotopes. For completeness, the reanalysis of the candidates for the $2f_{7/2}$ states in ^{131}Sn and ^{133}Sn are included. The values were extracted using the DWBA and FR-ADWA formalisms. The listed uncertainties include only experimental uncertainties. Values extracted from the FR-ADWA-CH are considered the most reliable and are listed in boldface.

			Spectroscopic Factors		
^{A}X	E_x (keV)	$n\ell j$	DWBA	FR-ADWA-KD	FR-ADWA-CH
^{125}Sn	2769	$2f_{7/2}$	0.40 ± 0.03	0.36 ± 0.03	**0.39 ± 0.03**
	3385	$3p_{3/2}$	0.37 ± 0.04	0.24 ± 0.02	**0.29 ± 0.03**
	3998	$3p_{1/2}$	0.55 ± 0.07	0.34 ± 0.04	**0.42 ± 0.05**
^{127}Sn	2705	$2f_{7/2}$	0.51 ± 0.07	0.49 ± 0.07	**0.54 ± 0.08**
	3325	$3p_{3/2}$	0.35 ± 0.04	0.23 ± 0.03	**0.27 ± 0.03**
	3881	$3p_{1/2}$	0.70 ± 0.06	0.43 ± 0.04	**0.49 ± 0.04**
^{129}Sn	2705	$2f_{7/2}$	0.72 ± 0.09	0.67 ± 0.09	**0.75 ± 0.10**
	3317	$3p_{3/2}$	0.39 ± 0.05	0.24 ± 0.03	**0.29 ± 0.04**
	3913	$3p_{1/2}$	0.63 ± 0.09	0.44 ± 0.07	**0.46 ± 0.07**
^{131}Sn	2628	$2f_{7/2}$	0.75 ± 0.11	0.85 ± 0.11	**0.95 ± 0.13**
	3404	$3p_{3/2}$	0.75 ± 0.11	0.50 ± 0.11	**0.55 ± 0.08**
	3986	$3p_{1/2}$	1.00 ± 0.14	0.88 ± 0.14	**1.00 ± 0.14**
	4655	$2f_{5/2}$	0.89 ± 0.12	0.66 ± 0.12	**0.76 ± 0.11**
^{133}Sn	0	$2f_{7/2}$	0.86 ± 0.07	0.90 ± 0.07	**1.00 ± 0.08**
	854	$3p_{3/2}$	0.92 ± 0.07	0.87 ± 0.07	**0.92 ± 0.07**
	1363	$3p_{1/2}$	1.1 ± 0.2	1.3 ± 0.3	**1.3 ± 0.3**
	2005	$2f_{5/2}$	1.5 ± 0.3	1.1 ± 0.3	**1.3 ± 0.3**

The reaction calculations were performed using the code FRESCO [Tho88], employing both a Distorted Wave Born Approximation (DWBA) and Finite

Range ADiabatic Wave Approximation (FR-ADWA) formalism. For the DWBA calculations, the Lohr-Haberli optical model parameterization was used for the deuteron and the Chapel Hill 89 optical model parameterization was for the proton potential. Two optical model parameterizations were used for the FR-ADWA calculations in order to estimate the uncertainty in the spectroscopic factors due to the choice of parameterization. A Reid interaction [Rei68] was used for the deuteron with the neutron-proton potential. A Koning-Delaroche potential was used for the proton and neutron, and a Chapel Hill 89 potential was used for the proton and neutron in a separate calculation. The adiabatic potential of the deuteron was calculated using the code TWOFNR [Iga08]. A major source of uncertainty in modeling transfer reactions is the choice of the Woods-Saxon potential parameters for the bound state. Density Functional Theory (DFT) can be used to predict these parameters, but for the tin isotopes the uncertainties would still be large [Ter05]. Therefore, we employed a Woods-Saxon shaped potential with the same radius parameter $r = 1.25$ fm and diffuseness parameter $a = 0.65$ fm adopted in previous experiments [Koz12, Ahn13, Jon11, Jon04, Tho07]. The optical model parameters for these calculations are summarized in Table 4.2, Table 4.3, and Table 4.4. The results of the spectroscopic factor analysis are summarized in Table 5.1.

The same global optical model parameters from Strömich et al. [Str77] that were used in the analysis by Jones et al. [Jon11] were used in a second DWBA

calculation, but the spectroscopic factor was still large. Regardless, the ADWA calculation with Chapel Hill parameters is considered the most reliable value and is used in all future calculations in this study.

Table 5.2: Sources of experimental uncertainty in spectroscopic factors and asymptotic normalization coefficients. The total uncertainty is calculated by adding the contributing terms in quadrature.

		Percentage Uncertainty			
^{A}X	E_x (keV)	Q-value fitting	Normalization	Ang. dist. fitting	Total
^{125}Sn	2769	4.3	6	3	8
	3385	7.2	6	4	10
	3998	6.7	6	10	13
^{127}Sn	2705	3.9	6	12	14
	3325	4.9	6	8	11
	3881	5.4	6	5	9
^{129}Sn	2705	3.5	5	12	13
	3317	5.1	5	12	14
	3913	4.8	5	13	15
^{131}Sn	2628	N/A[1]	10	10	14
	3404	N/A[1]	10	10	14
	3986	N/A[1]	10	10	14
	4655	N/A[1]	10	10	14
^{133}Sn	0	4.0	5	5	8
	854	3.5	5	5	8
	1363	6.4	5	20	22
	2005	7	5	20	22

[1]See text for details.

The uncertainty analysis is summarized in Table 5.2. There are three components to the total experimental uncertainty: the uncertainty in fitting states in the Q-value spectra, the beam normalization, and normalizing the theoretical differential cross section to the experimental differential cross section. For the

^{132}Sn(d,p) study, the authors divided each state in the Q-value spectrum into angular bins, and for each bin the population of a given state was determined by fitting a Gaussian to the data. The uncertainty presented in Table 5.2 reflects the average uncertainty from these fits. For both the ^{130}Sn(d,p) analysis and the present studies of ^{124,126,128}Sn(d,p), the population of each state was determined by estimating the full range of each peak and taking the total number of counts within this region. For the present study, the uncertainty listed was estimated by varying the range of the peak over reasonable values. As this uncertainty is small in comparison to the normalization uncertainties, the authors of the ^{130}Sn(d,p) study chose not to report these values since they do not represent a significant contribution to the total uncertainty. The uncertainties due to the normalizations were determined on a state-by-state basis using a chi-square fitting routine to find the optimum value of interest; the beam normalization in the plot of elastically scattered deuterons and the normalization factor for the theoretical differential cross section. The listed uncertainties reflect the percentage variation in the chi-square minimization. The size of these uncertainties for the two normalization values is determined largely from the number of counts in each angular bin and how well the shape of the theoretical curves describes the data. The uncertainty in the Q-value fitting is determined largely by statistics and the resolution that is dominated by energy straggling of the beam in the target.

In addition to the experimental uncertainties just described, theoretical uncertainties must also be considered. Spectroscopic factors were extracted for two different reaction formalisms, DWBA and FR-ADWA, and two different optical model parameterizations were used for the FR-ADWA calculations. Table 5.1 shows that the choice of optical model parameterization presents an uncertainty of up to 20% for the cases studied, whereas the choice of reaction formalism created a much larger source of uncertainty, varying as much as almost 40%. Furthermore, spectroscopic factors are highly sensitive to the choice of the bound state geometry of the neutron as reported by previous studies [Jon11]. The same sensitivity was found to be true in this study, as varying the radius and diffuseness parameters to $r = 1.2$ fm and $a = 0.6$ fm yielded uncertainties of nearly 40% in some cases.

One of the primary criticisms of spectroscopic factors is that extracted values depend on the choice of experimental reaction. Kramer et al. reported reduced spectroscopic factors extracted from the (e,e'p) reaction as compared to those from transfer reactions [Kra01]. In fact, knockout of deeply bound particles will in general yield lower spectroscopic factors [Gad08]. Initially it was assumed that these discrepancies were due to short-range correlations missing from the shell model. However, large-scale shell model [Bar09] and coupled-cluster calculations [Jen11] also indicate reduced spectroscopic factors, and hence that short-range correlations are not the only culprit. Lee et al. showed that spectroscopic

factors extracted from transfer reactions agree with those from the (e,e'p) reaction within the uncertainties when constraining the bound-state potential geometry using radii from Hartree-Fock calculations [Lee06]. It has also been shown that considering the nonlocal nature of the bound-state interaction can reduce spectroscopic factors [Kra01]. In the present study, a Woods-Saxon potential with standard radius and diffuseness was chosen for the bound state, and non-locality was not included. Since each set of spectroscopic factors in Table 5.1 were extracted using consistent theoretical parameters and formalism, it is possible to make relative comparisons for these values across the tin isotopes in the study.

The single-neutron strength for the $2f_{7/2}$ state in ^{125}Sn is consistent with previous measurements [Jon04, Str77, Tom11] and serves as a benchmark for the study. The $2f_{7/2}$ strength is monotonically decreasing from near the double-shell closure at ^{133}Sn towards stability at ^{125}Sn. Interestingly, the single-neutron strength of the $3p_{3/2}$ and $3p_{1/2}$ states remains high for both ^{133}Sn and ^{131}Sn, but then fragments quickly for the lighter mass tin isotopes in the study. One explanation for the observed fragmentation is mixing between the single-particle states and core-coupled states. For spherical nuclei, the single-particle strength is expected to be concentrated in one state. However, if the level density is sufficiently high, there will be other states with the same and parity quantum numbers with which the pure state can mix. The amount of mixing depends upon the energy separation between the two states and the mixing matrix element [Cas00].

In ^{133}Sn, the $2f_{7/2}$, $3p_{3/2}$, $3p_{1/2}$, and $2f_{5/2}$ strength has been observed to be concentrated in one state which is consistent with the doubly-magic nature of ^{132}Sn and the associated low level density [Jon11]. In contrast, there is a high fragmentation of these single-particle strengths in ^{125}Sn [Tom11]. The ^{124}Sn nucleus has eight neutron holes below the $N = 82$ shell closure and a significantly higher level density. At 2.6 MeV to 4 MeV in excitation energy, it is relatively easy to make $3/2^-$, $5/2^-$, and $7/2^-$ states in ^{125}Sn by coupling the $1h_{11/2}$ neutrons to the positive-parity states in the ^{124}Sn or the $2d_{3/2}$ neutrons to the negative parity 3^- and 5^- states in the core. However, as $N = 82$ is approached, the level density in the even mass tin cores is reduced, giving rise to fewer core-coupled states that could mix with the single-neutron states above the $N = 82$ shell gap, and hence fragmenting their strength.

5.2 Asymptotic Normalization Coefficients

Spectroscopic factors are known to be model dependent, as supported by the results in Table 5.1. For peripheral reactions, asymptotic normalization coefficients (ANCs) are relatively model independent and thus are more robust. An ANC, $C^2_{\ell j}$, is the product of the spectroscopic factor and the square of the single-particle ANC, $b_{\ell j}$, as described in section 2.4. The results of the asymptotic normalization coefficient calculations are summarized in Table 5.3.

Table 5.3: Asymptotic normalization coefficients of the three single-neutron states populated by (d, p) reactions on neutron-rich tin isotopes. For completeness, the reanalysis of the candidates for the $2f_{7/2}$ states in ^{131}Sn and ^{133}Sn are included. Listed error margins include only experimental uncertainties.

			C^2 (fm^{-1})		
^{A}X	E_x (keV)	$n\ell j$	DWBA	FR-ADWA-KD	FR-ADWA-CH
^{125}Sn	2769	$2f_{7/2}$	0.60 ± 0.05	0.54 ± 0.04	0.59 ± 0.05
	3385	$3p_{3/2}$	6.5 ± 0.7	4.2 ± 0.4	5.1 ± 0.5
	3998	$3p_{1/2}$	2.8 ± 0.6	2.6 ± 0.3	3.2 ± 0.4
^{127}Sn	2705	$2f_{7/2}$	0.72 ± 0.10	0.69 ± 0.10	0.76 ± 0.11
	3325	$3p_{3/2}$	5.9 ± 0.7	3.9 ± 0.4	4.6 ± 0.5
	3881	$3p_{1/2}$	5.8 ± 0.5	3.6 ± 0.3	4.2 ± 0.4
^{129}Sn	2705	$2f_{7/2}$	0.74 ± 0.10	0.69 ± 0.09	0.77 ± 0.10
	3317	$3p_{3/2}$	4.9 ± 0.7	3.0 ± 0.4	3.7 ± 0.5
	3913	$3p_{1/2}$	3.5 ± 0.5	2.4 ± 0.4	2.6 ± 0.4
^{131}Sn	2628	$2f_{7/2}$	0.74 ± 0.10	0.84 ± 0.12	0.94 ± 0.13
	3404	$3p_{3/2}$	7.4 ± 1.0	4.9 ± 0.7	5.4 ± 0.8
	3986	$3p_{1/2}$	3.9 ± 0.5	3.4 ± 0.5	3.9 ± 0.5
	4655	$2f_{5/2}$	$(4.0 \pm 0.5) \times 10^{-3}$	$(3.0 \pm 0.4) \times 10^{-3}$	$(3.4 \pm 0.6) \times 10^{-3}$
^{133}Sn	0	$2f_{7/2}$	0.70 ± 0.06	0.73 ± 0.06	0.81 ± 0.06
	854	$3p_{3/2}$	6.6 ± 0.5	6.3 ± 0.5	6.6 ± 0.5
	1363	$3p_{1/2}$	3.2 ± 0.7	3.8 ± 0.8	3.96 ± 0.9
	2005	$2f_{5/2}$	$(3.1 \pm 0.7) \times 10^{-3}$	$(2.3 \pm 0.5) \times 10^{-3}$	$(2.8 \pm 0.6) \times 10^{-3}$

The single particle ANCs were calculated directly in FRESCO and the spectroscopic factors were taken from Table 5.1. Single-particle ANCs are sensitive to the nuclear masses and hence the Q-value of the reaction, the radius and diffuseness of the mean field, and the spin-orbit potential depth. All of these input values are summarized in Tables 4.2, 4.3, and 4.4. It has been shown that for peripheral reactions, spectroscopic factors vary as a function of $b_{\ell j}$, but C^2 is independent of this parameter. Reference [Tho07] provides a summary of the analysis that demonstrates the peripheral nature of the (d, p) reaction at 4 MeV/u and the dependence of S and C^2 on $b_{\ell j}$. It bears repeating that the mean field radius and diffuseness were chosen to be $r = 1.25$ fm and $a = 0.65$ fm.

5.3 Neutron Capture Cross Sections

The structure information presented in this chapter can be used to calculate the Direct-Semi Direct (DSD) component of neutron capture on the tin isotopes in the present study. In direct capture the captured neutron directly populates a discrete bound state in the final nucleus. Semi direct capture proceeds by exciting the Giant Dipole Resonance (GDR), followed by electromagnetic transitions to the low-lying states in the final nucleus. As the nuclei in the present study are near a shell closure for both protons and neutrons, it is expected that the level density is low and the DSD neutron capture will dominate over capture through resonances above the neutron separation energy [Moh12].

The calculations were performed with the code CUPIDO under the guidance of Goran Arbanas [Par95, Arb05]. The excitation energies, spins, parities, and spectroscopic factors used in the calculations are found in Table 5.1 and the GDR information was taken from recent data evaluations [Rip14]. At low neutron energies, low-spin states will dominate direct neutron capture as seen in Figures 5.1, 5.2, 5.3, 5.4, and 5.5. The calculation for neutron capture on ^{132}Sn at 30 keV agrees with previous calculations [Rau98]. The calculation for neutron capture on ^{130}Sn at 30 keV is slightly reduced from that of Kozub et al., but agrees within the listed uncertainties.

Figure 5.6 shows the DSD neutron capture cross sections calculated in this study compared with recent theoretical calculations [Chi08]. The set of DSD neutron capture cross section calculations from Reference [Chi08] was made using theoretical spectroscopic factors, but these calculations overestimate the cross sections at 30 keV. Additionally, Kozub et al. suggested that this discrepancy for neutron capture on ^{130}Sn is likely due to using different single particle level energies or a different single particle bound-state potential by Koura et al. [Kou00]. The Hauser-Feshbach calculations in Figure 5.6 assume a high level density near the neutron separation energy as mentioned in Section 2.5. An open question is the role that Hauser-Feshbach statistical neutron capture plays in the tin isotopes as the level density changes across the neutron-rich tin isotopes.

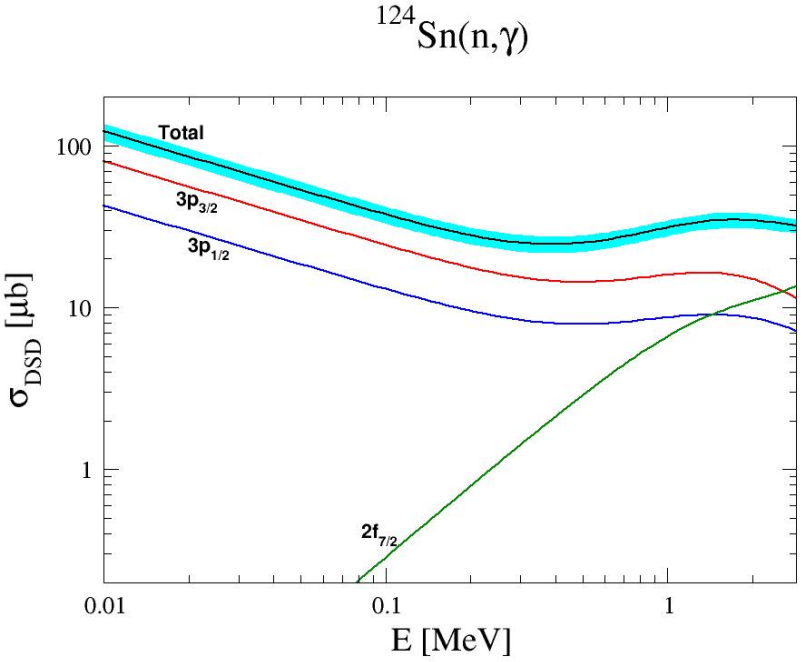

Figure 5.1: Calculation of direct-semidirect neutron capture on ^{124}Sn. The teal band represents the uncertainty in the cross section due to the uncertainties in the spectroscopic factors. Low spin states dominate the capture at low neutron energies.

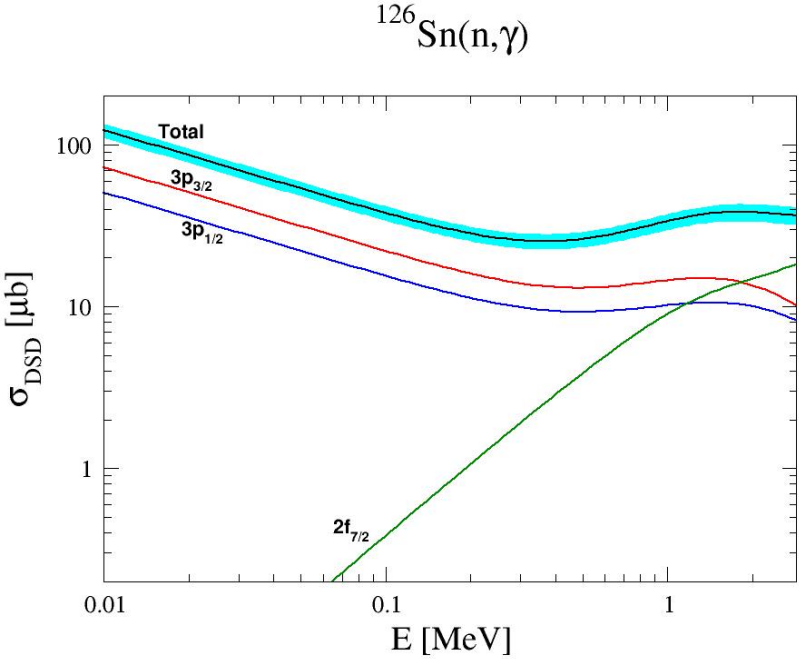

Figure 5.2: Calculation of direct-semidirect neutron capture on ^{126}Sn. The teal band represents the uncertainty in the cross section due to the uncertainties in the spectroscopic factors. Low spin states dominate the capture at low neutron energies.

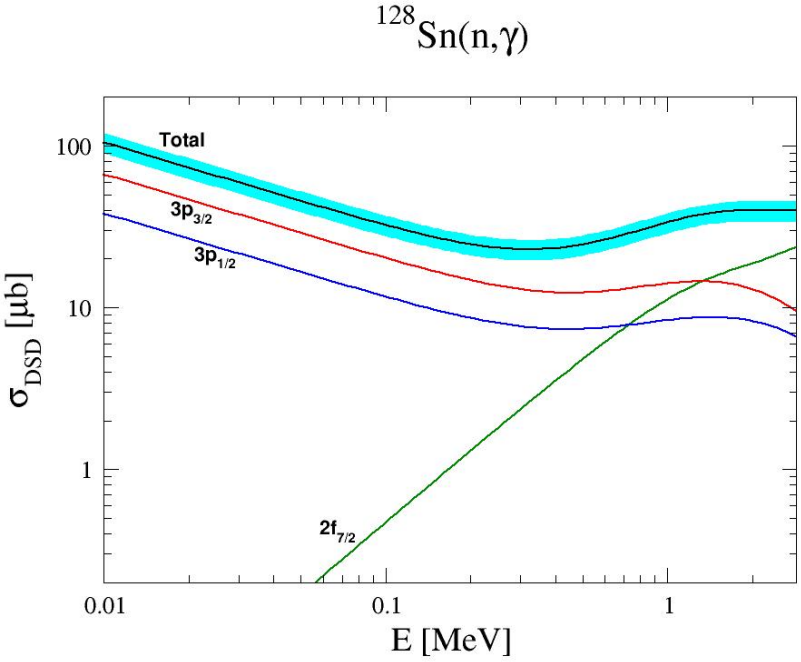

Figure 5.3: Calculation of direct-semidirect neutron capture on ^{128}Sn. The teal band represents the uncertainty in the cross section due to the uncertainties in the spectroscopic factors. Low spin states dominate the capture at low neutron energies.

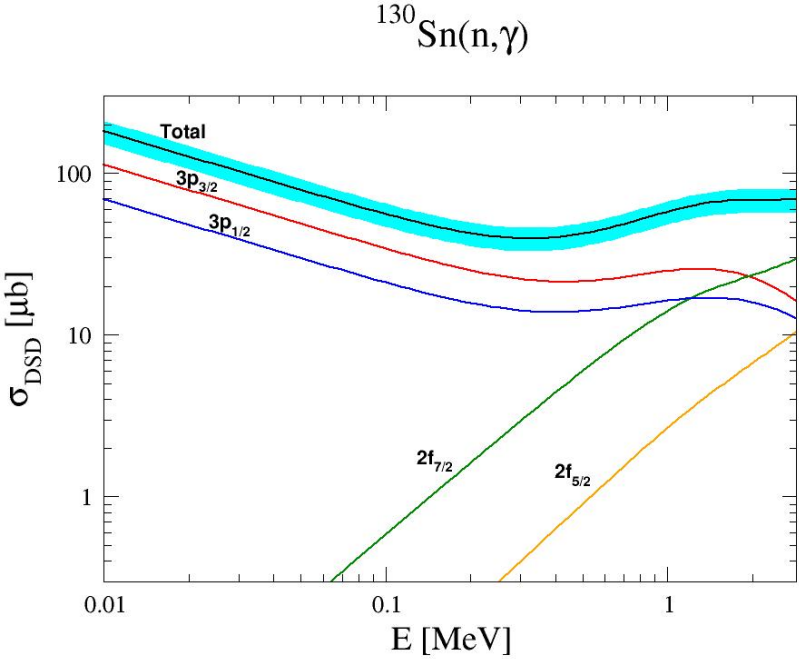

Figure 5.4: Calculation of direct-semidirect neutron capture on ^{130}Sn. The teal band represents the uncertainty in the cross section due to the uncertainties in the spectroscopic factors. Low spin states dominate the capture at low neutron energies.

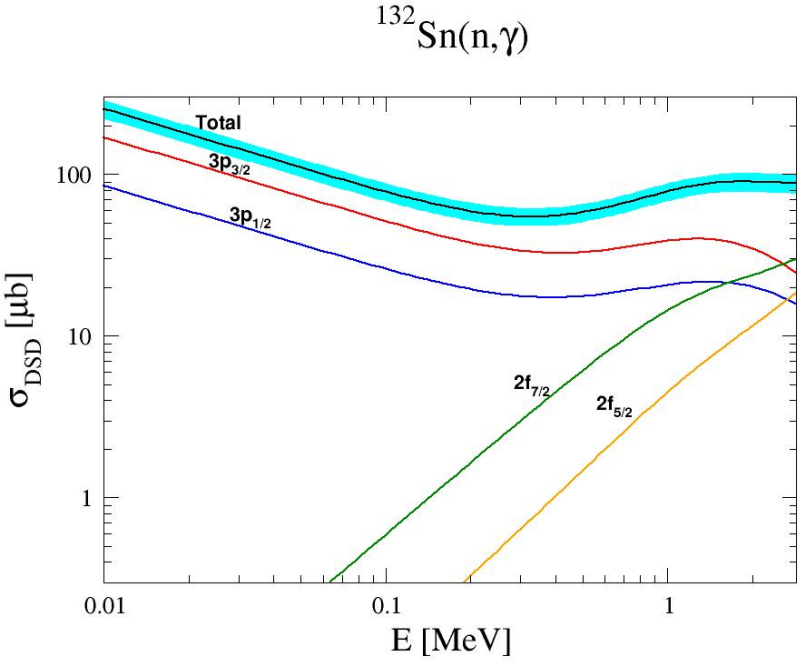

Figure 5.5: Calculation of direct-semidirect neutron capture on ^{132}Sn. The teal band represents the uncertainty in the cross section due to the uncertainties in the spectroscopic factors. Low spin states dominate the capture at low neutron energies.

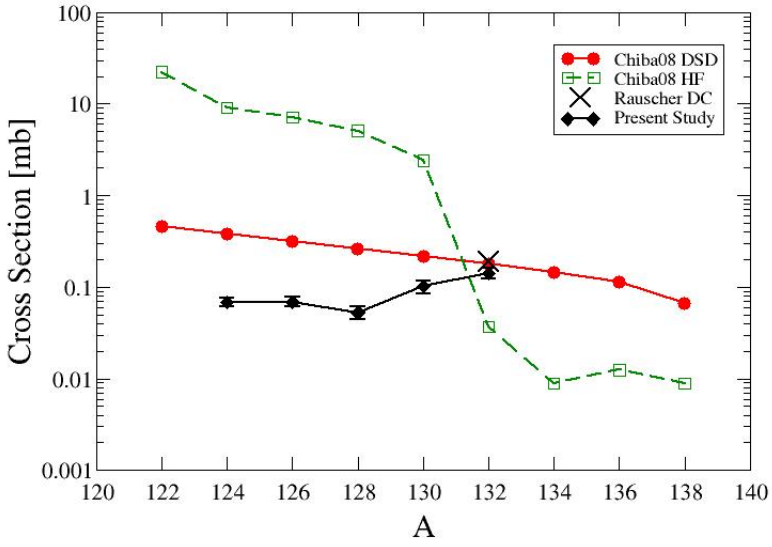

Figure 5.6: Comparison of calculated neutron capture cross sections for tin isotopes at 30 keV. Present DSD calculations with experimental spectroscopic factors (black diamonds), Hauser-Feshbach model calculations [Chi08] (green squares), direct capture using theoretical spectroscopic factor [Rau98] (black "X"), and DSD calculations with theoretical spectroscopic factors [Chi08].

Chapter 6

Summary and Outlook

Radioactive ion beams of ^{126}Sn and ^{128}Sn were used to measure the ^{126}Sn(d,p) and ^{128}Sn(d,p) reactions for the first time, along with a stable beam of ^{124}Sn to measure the ^{124}Sn(d,p) reaction. The neutron-rich tin isotopes were produced through proton-induced fission on a thick uranium carbide target at the Holifield Radioactive Ion Beam Facility at Oak Ridge National Laboratory, and the desired isotope was chemically and magnetically separated from contaminants yielding about 99% beam purity [HRI14, Sha11]. Reaction protons were detected in the SuperORRUBA silicon detectors and the heavy beam-like particles were detected in a newly commissioned ionization counter [Bar13b, Cha14]. Due to the large number of electronics channels used in this experiment, a new Application Specific Integrated Circuits (ASICs) electronics setup was implemented as a part of these efforts [Ahn13]. For the present study, excitation energies and proton differential cross sections were measured for single-neutron states in ^{125}Sn, ^{127}Sn, and ^{129}Sn. Orbital angular momentum transfers, spectroscopic factors, asymptotic normalization coefficients, and direct-semidirect neutron capture cross sections were calculated using the same reaction models for the states in the ^{125}Sn, ^{127}Sn, and ^{129}Sn in addition to the analogous single-neutron states in ^{131}Sn and ^{133}Sn

from previous studies [Koz12, Jon11, Jon10].

The adopted spins and parities in ^{127}Sn and ^{129}Sn agree with previous studies of single-neutron states in neighboring tin isotopes. This was the first observation of single-neutron excitations above the $N = 82$ shell gap for these isotopes. The extracted spectroscopic factors indicate a steady increase in the fragmentation of the $2f_{7/2}$ state from ^{133}Sn to ^{125}Sn. For the $3p_{3/2}$ and $3p_{1/2}$ states, the fragmentation sets in very suddenly for odd-mass tin isotopes lighter than ^{131}Sn. Asymptotic normalization coefficients have been extracted for these three states in ^{133}Sn, ^{131}Sn, ^{129}Sn, ^{127}Sn, and ^{125}Sn. The spectroscopic factors have been used to calculate the DSD neutron capture on ^{132}Sn, ^{130}Sn, ^{128}Sn, ^{126}Sn, and ^{124}Sn, and these results have been compared with other recent calculations of these cross sections. Given that the deduced DSD neutron capture cross sections are relatively small for the $N < 82$ tin isotopes, it is important to understand the role of HF statistical neutron capture in this region.

Nuclear states populated in transfer reactions in inverse kinematics with heavy ion beams near double shell closures can be resolved with silicon detectors alone due to the low level density of states. For systems just a few nucleons away from double shell closures, however, the single-particle strength can become fragmented very quickly. For example, two protons beyond ^{133}Sn, the single-neutron strength for states in ^{135}Te is much more fragmented and better energy resolution

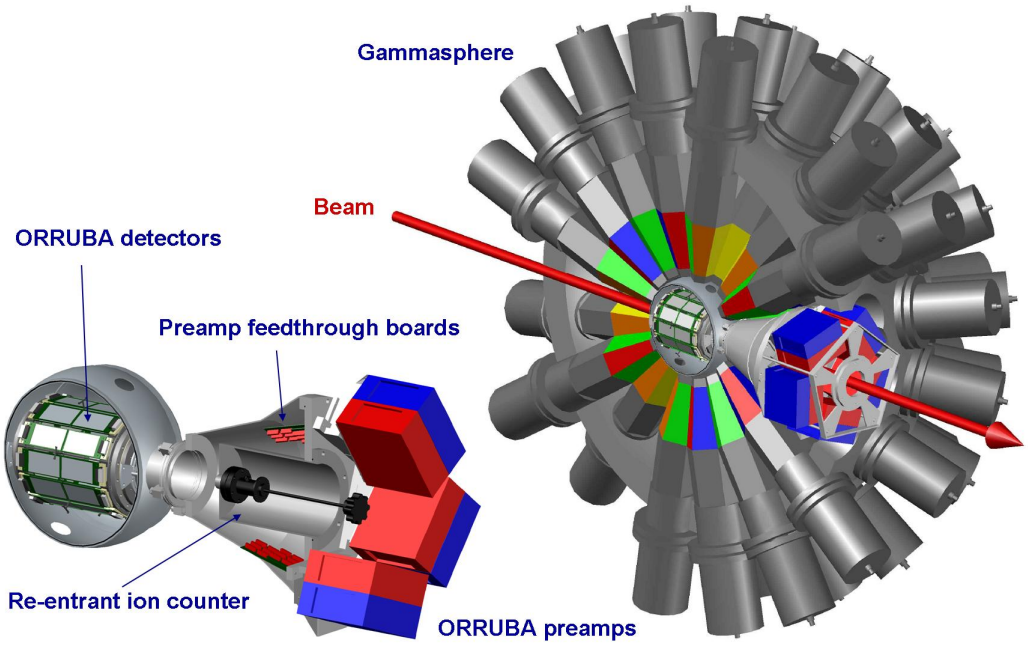

Figure 6.1: CAD drawings of the GODDESS coupling, showing the silicon detector setup alone on the left and the full setup installed inside of Gammasphere on the right. It is important to minimize the length of the signal cables between the detectors and the preamps in order to reduce noise. Special care was taken to place the preamp boxes near the detectors while limiting the number of gamma-ray detectors that would need to be removed from Gammasphere. Figure taken from Reference [Pai14].

is required to resolve these states [Jon08, Ciz09, Pai13].

High-purity germanium (HPGe) detectors have long been used to detect gamma rays with an energy resolution of 2 keV at 1.33 MeV [Kno10]. The downside is that the detection efficiency is very low, so large detector arrays are needed. This is especially true for radioactive ion beam experiments with low beam rates [Kno10]. Fortunately, large arrays of HPGe detectors have been constructed, such as Gammasphere [Lee90], and more recently, GRETINA [Lee99, Pas13]. Coupling arrays of gamma ray detectors and charged particle detectors has long been a powerful

technique for studying nuclear states (see references found within [All13]). Recent efforts have been made to couple the Oak Ridge Rutgers University Barrel Array (ORRUBA) [Pai07] with Gammasphere and potentially GRETINA to form the Gammasphere ORRUBA Dual Detectors for Experimental Structure Studies (GODDESS) [Pai14, Rat13] (see Figure 6.1). GODDESS will have the energy resolution to study closely spaced nuclear states that will be common in many of the anticipated beams from the CAlifornium Rare Isotope Breeder Upgrade (CARIBU) [Sav05] at Argonne National Laboratory (ANL). Figure 6.2 shows the expected yields for each isotope at CARIBU. The most intense beams will be centered around the fission fragment peaks of ^{252}Cf. The majority of the isotopes for which transfer reactions will be possible are mid-shell nuclei with high level densities. Thus, GODDESS will be a critical spectroscopic tool for the beams at CARIBU.

The future of radioactive ion beam experiments in the United States will be the Facility for Rare Isotope Beams (FRIB) at Michigan State University [Wei13]. FRIB will provide greater beam intensities for many isotopes previously studied in addition to producing many isotopes far from stability that have never been studied. GODDESS could be used with GRETINA at FRIB to study these new isotopes as well as improving on previous experiments. Even for nuclei with lower level densities, GODDESS will provide significant improvements. Specifically, the present study could be improved using the excellent gamma-ray energy resolution

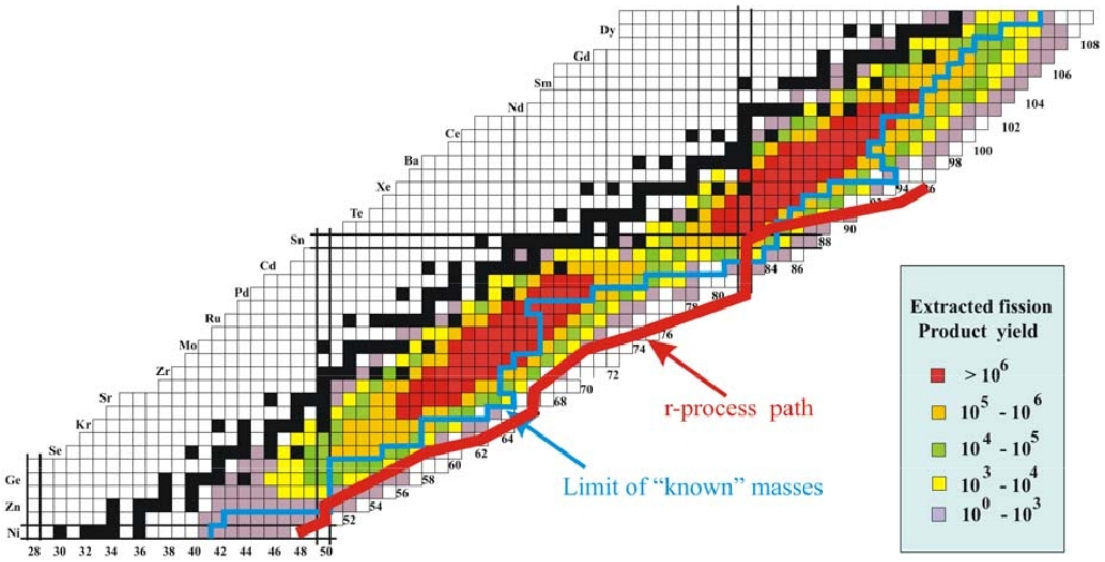

Figure 6.2: Chart of the nuclides; an r-process path is depicted by the red line and a blue line indicates the present limits of studied isotopes. The yield expected from an ion source system based on a 1 Ci californium fission source is indicated by the color of each square, as explained in the legend on the right. Figure taken from Reference [Sav05].

of GODDESS. The increased resolution would not only allow for better determination of excitation energies, but would also reduce uncertainties in the extracted spectroscopic factors. The latter is made possible by determining the population of each state in the Q-value spectrum in coincidence with gamma-rays of interest. Future systematic studies of spectroscopic factors will be greatly enhanced by the improved energy resolution capable with GODDESS as well as the additional information that charged particle-gamma spectroscopy provides [All13].

For stable isotopes, or those with long half-lives, it is possible to make a target and measure neutron capture directly. Neutron capture on exotic nuclei far from stability can be an important input to r-process calculations [Sur09], but for these nuclei it is not possible to directly measure the cross section. There are

ongoing efforts to validate the $(d, p\gamma)$ reaction in inverse kinematics as a surrogate reaction for the (n, γ) reaction [Hat10, Ciz13]. Measuring this surrogate reaction could provide the Hauser-Feshbach contribution to neutron capture. FRIB will provide beams of these critical isotopes, and GODDESS will have the resolution and efficiency to make $(d, p\gamma)$ reaction studies possible in the near future.

Bibliography

[Ahn13] S. Ahn. *The study of nuclear structure of neutron-rich* ^{81}G*e and its contribution in the r-process via the neutron transfer reaction* ^{80}G*e(d,p).* Ph.d. thesis, University of Tennessee, 2013.

[All12] J. M. Allmond, D. C. Radford, J. Pavan, K. Lagergren, C. Baktash, J. R. Beene, C. R. Bingham, L. Chaturvedi, M. Danchev, D. Fong, A. Galindo-Uribarri, P. A. Hausladen, J. K. Hwang, W. Krolas, J. F. Liang, E. Padilla-Rodal, W. Reviol, D. G. Sarantites, D. Seweryniak, D. Shapira, A. E. Stuchbery, J. P. Urrego-Blanco, R. L. Varner, X. Wang, C. H. Yu, S. Zhu, Phys. Rev. C **86**, 031307, 2012.

[All13] J. M. Allmond, AIP Conf. Proc., **1525**, 610, 2013.

[All14] J. M. Allmond, A. ,E. Stuchbery, J. R. Beene, A. Galindo-Uribarri, J. F. Liang, E. Padilla-Rodal, D. C. Radford, R. L. Varner, A. Ayres, J. C. Batchelder, A. Bey, C. R. Bingham, M. E. Howard, K. L. Jones, B. Manning, P. E. Mueller, C. D. Nesaraja, S. D. Pain, W. A. Peters, A. Ratkiewicz, K. T. Schmitt, D. Shapira, M. S. Smith, N. J. Stone, D. W. Stracener, and C. H. Yu, Phys. Rev. Lett. **112**, 172701, 2014.

[Arb05] G. Arbanas, F. S. Dietrich, A. K. Kerman *Direct-Semidirect Thermal*

Neutron Capture Calculations, Perspectives on Nuclear Data for the Next Decade, 2005.

[Bar01] D. W. Bardayan, J. C. Blackmon, W. Bradfield-Smith, C. R. Brune, A. E. Champagne, T. Davinson, B. A. Johnson, R. L. Kozub, C. S. Lee, R. Lewis, P. D. Parker, A. C. Shotter, M. S. Smith, D. W. Visser, and P. J. Woods, Phys. Rev. C **63**, 065802, 2001.

[Bar09] C. Barbieri, Phys. Rev. Lett. **103**, 202502, 2009.

[Bar13a] S. Baroni, Petr Navrátil, and S. Quaglioni, Phys. Rev. C **87**, 034326, 2013.

[Bar13b] D. W. Bardayan, S. Ahn, J. C. Blackmon, A. J. Burkhart, K. Y. Chae, J. A. Cizewski, J. Elson, S. Hardy, R. L. Kozub, L. Linhardt, B. Manning, M. Matos, S. D. Pain, L.G. Sobotka, and M. S. Smith, Nucl. Instrum. Meth. **A711**, 160, 2013.

[Bar39] W. H. Barkas, Phys. Rev. **55**, 691, 1939.

[Ber00] M. J. Berger, J. S. Coursey, and M. A. Zucker, *ESTAR, PSTAR, and ASTAR: Computer Programs for Calculating Stopping-Power and Range Tables for Electrons, Protons, and Helium Ions* (version 1.2.2), (2000) Available: http://physics.nist.gov/Star [2005, January 11], National Institute of Standards and Technology, Gaithersburg, MD.

[Ber04] C. A. Bertulani and P. Danielewicz, *Introduction to Nuclear Reactions*. (Institute of Physics, London, 2004).

[Bro10] S. M. Brown. *Neutron Shell Breaking in Neutron-Rich Neon Isotopes* Ph.D. thesis, University of Surrey, 2010.

[Bru77] P. J. Brussaard and P. W. M. Glaudemans *Shell-Model Applications in Nuclear Spectroscopy.* (North Holland Publishing Co., Amsterdam, 1977).

[Bur57] E. M. Burbidge, G. R. Burbidge, W. A. Fowler, and F. Hoyle, Rev. Mod. Phys., **29**, 547, 1957.

[Car97] H. K. Carter, J. Kormicki, D. W. Stracener, J. B. Breitenbach, J. C. Blackmon, M. S. Smith, and D. W. Bardayan, Nucl. Instrum. Meth. **B126**, 166, 1997.

[Cas00] *Nuclear Physics from a Simple Perspective.* (University of Oxford Press, New York, 2000).

[Cat04] W. C. Catford, http://personal.ph.surrey.ac.uk/ phs1wc/kinematics/.

[Cha14] K. Y. Chae, S. H. Ahn, D. W. Bardayan, K. A. Chipps, B. Manning, S. D. Pain, W. A. Peters, K. T. Schmitt, M. S. Smith, and S. Strauss, Nucl. Instrum. Meth. In Press, 2014.

[Chi08] S. Chiba, H. Koura, T. Hayakawa, T. Maruyama, T. Kawano, and T. Kajino, Phys. Rev. C, **77**, 015809, 2008.

[Chr79] L. G. Christophorou, D. L. McCorkle, D. V. Maxey, and J. G. Carter, Nucl. Instrum. Meth. **163**, 141, 1979.

[Ciz09] J. A. Cizewski, Nuclear Fission and Fission-Product Spectroscopy, AIP Conf. Proc. **1175**, 147, 2009.

[Ciz13] J. A. Cizewski, Journal of Physics: Conference Series **420**, 012058, 2013.

[Cla68] D. D. Clayton, *Principles of Stellar Evolution and Nucleosynthesis*. (University of Chicago Press, Chicago, 1968).

[Eng07] G. L. Engel, M. Sadasivam, M. Nethi, J. M. Elson, L. G. Sobotka, and R. J. Charity, Nucl. Instrum. Meth. **A**, 573, 2007.

[ENS11] http://www.nndc.bnl.gov/ensdf.

[Gad08] A. Gade et al., Phys. Rev. C **77**, 044306, 2008.

[Gau04] H. Gausemel, B. Fogelberg, T. Engeland, M. Hjorth-Jensen, P. Hoff, H. Mach, K. A. Mezilev, and J. P. Omtvedt, Phys. Rev. C, **69**, 054307, 2004.

[Hab11] D. Habs, P G. Thirolf, M. Gross, K. Allinger, J. Bin, A. Henig, D. Kiefer, W. Ma, and J. Schreiber, Applied Phys. B, **103**, 471, 2011.

[Hat10] R. Hatarik, L. A. Bernstein, J. A. Cizewski, D. L. Bleuel, J. T. Burke, J. E. Escher, J. Gibelin, B. L. Goldblum, A. M. Hatarik, S. R. Lesher, P. D. O'Malley, L. Phair, E. Rodriguez-Vieitez, T. Swan, and M. Wiedeking, Phys. Rev. C **81**, 011602, 2010.

[Hau52] W. Hauser and H. Feshbach, Phys. Rev., **87** 366, 1952.

[Hax49] O. Haxel, T. H. D. Jensen, and H. E. Suess, Phys. Rev. **75**, 1766, 1949.

[Hil78] W. Hillebrandt, Space Sci. Rev. **21**, 639, 1978.

[HRI14] http://www.phy.ornl.gov/hribf/misc/whatishribf.shtml

[Hun88] S. R. Hunter, J. G. Carter, and L. G. Christophorou, Phys. Rev. A **38**, 58, 1988..

[Iga08] M. Igarashi and M. Toyama, Computer program TWOFNR, University of Surrey, modified version (2008).

[Jac99] J. D. Jackson. *Classical Electrodynamics*. (Wiley, New York, 1999).

[Jen11] Ø. Jensen, G. Hagen, M. Hjorth-Jensen, B. Alex Brown, and A. Gade, Phys. Rev. Lett. **107**, 032501, 2011.

[Joh70] R. C. Johnson and P. J. R. Soper, Phys. Rev. C, **1**, 976, 1970.

[Joh72] R. C. Johnson and P. J. R. Soper, Nucl. Phys. A, **182**, 619, 1972.

[Joh74] R. C. Johnson and P. C. Tandy, Nucl. Phys. A, **235**, 56, 1974.

[Jon04] K. L. Jones, R. L. Kozub, C. Baktash, D. W. Bardayan, J. C. Blackmon, W. N. Catford, J. A. Cizewski, R. P. Fitzgerald, M. S. Johnson, R. J. Livesay, Z. Ma, C. D. Nesaraja, D. Shapira, M. S. Smith, J. S. Thomas, and D. W. Visser, Phys. Rev. C, **70**, 067602, 2004.

[Jon08] K. L. Jones, R. L. Kozub, S. D. Pain, and J. A. Cizewski, Nucl. Phys. A, **805**, 215, 2008.

[Jon10] K. L. Jones, A. S. Adekola, D. W. Bardayan, J. C. Blackmon, K. Y. Chae, K. A. Chipps, J. A. Cizewski, L. Erikson, C. Harlin, R. Hatarik, R. Kapler, R. L. Kozub, J. F. Liang, R. Livesay, Z. Ma, B. H. Moazen, C. D. Nesaraja, F. M. Nunes, S. D. Pain, N. P. Patterson, D. Shapira, J. F. Shriner Jr, M. S. Smith, T. P. Swan and J. S. Thomas, Nature, **465** 454, 2010.

[Jon11] K. L. Jones, F. M. Nunes, A. S. Adekola, D. W. Bardayan, J. C. Blackmon, K. Y. Chae, K. A. Chipps, J. A. Cizewski, L. Erikson, C. Harlin, R. Hatarik, R. Kapler, R. L. Kozub, J. F. Liang, R. Livesay, Z. Ma, B. Moazen, C. D Nesaraja, S. D. Pain, N. P. Patterson, D. Shapira, J. F. Shriner Jr., M. S. Smith, T. P. Swan, and J. S. Thomas, Physical Review C, **84**, 034601, 2011.

[Kim05] K. Kimura, T. Izumikawa, R. Koyama, T. Ohnishi, T. Ohtsubo, A. Ozawa, W. Shinozaki, T. Suzuki, M. Takahashi, I. Tanihata, T. Yamaguchi, and Y. Yamaguchi, Nucl. Instrum. Meth. **A538**, 608, 2005.

[Kno10] G. F. Knoll. *Radiation Detection and Measurement.* (Wiley, New York, 2010).

[Kon03] A. J. Koning and J. P. Delaroche, Nucl. Phys. A **713**, 231, 2003.

[Kou00] H. Koura and M. Yamada, Nucl. Phys. A **671**, 96, 2000.

[Koz12] R. L. Kozub, G. Arbanas, A. S. Adekola, D. W. Bardayan, J. C. Blackmon, K. Y. Chae, K. A. Chipps, J. A. Cizewski, L. Erikson, R. Hatarik,

W. R. Hix, K. L. Jones, W. Krolas, J. F. Liang, Z. Ma, C. Matei, B. H. Moazen, C. D. Nesaraja, S. D. Pain, D. Shapira, J. F. Shriner, Jr., M. S. Smith, and T. P. Swan, Phys. Rev. Lett. **109**, 172501, 2012.

[Kra01] G. J. Kramer, H. P. Blok, and A. Lapikás, Nucl. Phys. **679**, 267, 2001.

[Kra87] K. S. Krane. *Introductory Nuclear Physics.* (Wiley, New York, 1987).

[Kra96] E. Krausmann, W. Balogh, H. Oberhummer, T. Rauscher, K. L. Kratz, and W. Ziegert, Phys. Rev. C **53**, 469, 1996.

[Lee06] J. Lee, J. A. Tostevin, B. A. Brown, F. Delaunay, W. G. Lynch, M. J. Saelim, and M. B. Tsang, Phys. Rev. C **73**, 044608, 2006.

[Lee10] H. C. Lee. *Survey of Neutron Spectroscopic Factors and Asymmetry Dependence of Neutron Corrleations in Transfer Reactions.* Ph.d. thesis, 2010.

[Lee90] I. Y. Lee, Nucl. Phys. A, **520**, 641, 1990.

[Lee99] I. Y. Lee, Nucl. Instrum. Methods Phys. Res. A, **422**, 195, 1999.

[Loh74] J. M. Lohr and W. Haeberli, Nucl. Phys. A, **232**, 381, 1974.

[Mar68] J. B. Marion and F. C. Young, *Nuclear Reaction Analysis.* (Wiley, New York, 1968).

[Mat90] G. J.Mathews, J. J. Cowan, Nature **345**, 491, 1990.

[May49] M. G. Mayer, Phys. Rev. **75**, 1969, 1949.

[Mil02] W. Milner, STOPIT, 2002.

[Moh12] P. Mohr, Phys. Rev. C, **86**, 068803, 2012.

[Muk01] A. M. Mukhamedzhanov, C. A. Gagliardi, and R. E. Tribble, Phys. Rev. C **63**, 024612, 2001.

[Mum12] M. R. Mumpower, G. C. McLaughlin, and R. Surman, Phys. Rev. C, **86**, 035803, 2012.

[Nav00] P. Navrátil, J. P. Vary, and B. R. Barrett, Phys. Rev. C **62**, 054311, 2000.

[Nil95] S. G. Nilsson and I. Ragnarsson, *Shapes and Shells in Nuclear Structure*. (Cambridge University Press, New York, 1995).

[Nun11] F. M. Nunes and A. Deltuva, Phys. Rev. C, **84**, 034607, 2011.

[Pai07] S. D. Pain, J. A. Cizewski, R. Hatarik, K. Jones, J. Thomas, D. Bardayan, J. Blackmon, C. Nesaraja, M. Smith, R. Kozub, and M. Johnson, Nucl. Instr. and Meth. in Phys. Res. B, **261**, 1122, 2007.

[Pai13] S. D. Pain, Private Communication, 2013.

[Pai14] S. D. Pain, AIP Advances, **4**, 041015, 2014.

[Par95] W. E. Parker, M. B. Chadwick, R. M. Chasteler, F. S. Dietrich, M. A. Godwin, A. R. Kerman, L. H. Kramer, K. E. Sale, G. J. Schmid, and H. R. Weller, Phys. Rev. C, **52**, 252, 1995.

[Pas13] S. Paschalis, I. Y. Lee, A. O. Macchiavelli, C. M. Campbell, M. Cromaz, S. Gros, J. Pavan, J. Qian, R. M. Clark, H. L. Crawford, D. Doering, P. Fallon, C. Lionberger, T. Loew, M. Petri, T. Stezelberger, S. Zimmermann, D. C. Radford, K. Lagergren, D. Weisshaar, R. Winkler, T. Glasmacher, J. T. Anderson, and C. W. Beausang, Nucl. Instrum. Methods Phys. Res. A **597**, 233, 2013.

[Per76] C. M. Perey and F. G. Perey, At. Data Nucl. Data Tables, **17**, 1, 1976.

[Qia03] Y. Z. Qian, Prog. Part. Nucl. Phys., **50**, 153, 2003.

[Rat13] A. Ratkiewicz, S. D. Pain, J. A. Cizewski, D. W. Bardayan, J. C. Blackmon, K. A. Chipps, S. Hardy, K. L. Jones, R. L. Kozub, C. J. Lister, B. Manning, M. Matos, W. A. Peters, D. Seweryniak, and C. Shand, AIP Conf. Proc., **1525**, 487, 2013.

[Rau97] T. Rauscher, F. K. Thielemann, and K. L. Kratz, Phys. Rev. C, **56**, 1613, 1997.

[Rau98] T. Rauscher, R. Bieber, H. Oberhummer, K. L. Kratz, J. Dobaczewski, P. Moller, and M. M. Sharma, Phys. Rev. C, **57**, 2031, 1998.

[Rei68] R. V. Reid Jr, Ann. Phys., **50**, 411, 1968.

[Ria00] RIA White Paper, 17, 2000.

[Rin80] P. Ring and P. Schuck, *The Nuclear Many Body Problem*. (Springer-Verlag, New York, 1980).

[Rip14] https://www-nds.iaea.org/RIPL-3/.

[Sat70] G. R. Satchler, *Introduction to Nuclear Reactions.* (Wiley, New York, 1970).

[Sat83] G. R. Satchler, *Direct Nuclear Reactions.* (Oxford University Press, New York, 1983).

[Sav05] G. Savard and R. Pardo, http://www.phy.anl.gov/atlas/caribu/Cf252-upgrade-proposal-final-Rev4.pdf.

[Sch12] K. T. Schmitt, K. L. Jones, S. H. Ahn, A. Bey, D. W. Bardayan, J. C. Blackmon, S. M. Brown, K. Y. Chae, K. A. Chipps, J. A. Cizewski, K. I. Hahn, J. J. Kolata, R. L. Kozub, J. F. Liang, C. Matei, M. Matos, D. Matyas, B. Moazen, C. Nesaraja, F. M. Nunes, P. D. O'Malley, S. D. Pain, W. A. Peters, S. T. Pittman, A. Roberts, D. Shapira, J. F. Shriner, Jr., M. S. Smith, I. Spassova, D. W. Stracener, A. N. Villano, and G. L. Wilson, Phys. Rev. Lett., **108**, 192701, 2012.

[Sha11] D. Shapira, Private communication, 2011.

[Str03] D. W. Stracener, Nucl. Instrum. Meth. **B204**, 42, 2003.

[Str04] D. W. Stracener, G. D. Alton, R. L. Auble, J. R. Beene, P. E. Mueller, and J. C. Bilheux, Nucl. Instrum. Meth. **A521**, 126, 2004.

[Str77] A. Stromich, B. Steinmetz, R. Bangert, B. Gonsior, M. Roth, and P. von Brentano, Phys. Rev. C, **16**, 2193, 1977.

[Sur01] R. Surman and J. Engel, Phys. Rev. C, **64**, 035801, 2001.

[Sur09] R. Surman, J. Beun, G. C. Mclaughlin, and W. R. Hix, Phys. Rev. C, **79**, 045809, 2009.

[Ter05] J. Terasaki, J. Engel, M. Bender, J. Dobaczewski, W. Nazarewicz, and M. Stoitsov, Phys. Rev. C, **71**, 034310, 2005.

[Tho05] J. S. Thomas. *Single-Neutron Excitations of the N = 51 Isotones* ^{83}*Ge and* ^{85}*Se.* Ph.d. thesis, Rutgers University, 2005.

[Tho07] J. S. Thomas, G. Arbanas, D. W. Bardayan, J. C. Blackmon, J. A. Cizewski, D. J. Dean, R. P. Fitzgerald, U. Greife, C. J. Gross, M. S. Johnson, K. L. Jones, R. L. Kozub, J. F. Liang, R. J. Livesay, Z. Ma, B. H. Moazen, C. D. Nesaraja, D. Shapira, M. S. Smith, and D. W. Visser, Phys. Rev. C, **76**, 044302, 2007.

[Tho09] I. J. Thompson and F.M. Nunes, *Nuclear Reactions for Astrophysics: Principles, Calculation and Applications.* (University Press, Cambridge, 2009).

[Tho88] I. J. Thompson, Comp. Phys. Rep., **7**, 167, 1988.

[Tom11] I. Tomandl, J. Honz, T. von Egidy, H.-F. Wirth, T. Faestermann, V. Yu. Ponomarev, S. Pasic, R. Hertenberger, Y. Eisermann, and G. Graw Phys. Rev. C, **83**, 044326, 2011.

[Var91] R. L. Varner, W. J. Thompson, T. L. McAbee, E. J. Ludwig, and T. B. Clegg, Phys. Rep., **201**, 57, 1991.

[Wei13] J. Wei, *P*roceedings of the Particle Accelerator Conference 2013, 1453, 2013.

[Won04] S. M. Wong *Introductory Nuclear Physics*. (Wiley-VCH, Weinheim, 2004).